Superconducting Nanowires in Coherent Quantum Circuits

Zur Erlangung des akademischen Grades eines

Doktors der Naturwissenschaften (Dr. rer. nat.)

von der KIT-Fakultät für Physik des

Karlsruher Instituts für Technologie (KIT)

genehmigte

Dissertation

von

M.Sc. Yannick Schön

Acknowledgments

Nature surely would have been much less welcoming of my little scientific endeavor, had I dared to undertake any of it alone — an ant dreaming of the mountains. It is therefore my pleasure to acknowledge all those who paved the way in front of my feet by sharing tools, know-how, ideas, and insights — and by keeping the waves from crashing over my head.

To Prof. Dr. Alexey V. Ustinov I owe my gratitude not only for taking me into his group but also for numerous opportunities to study wave dynamics and low temperature physics outside of the lab in a great atmosphere and for facilitating my participation in numerous international conferences. Hadn't I joined the International Conference on Quantum Technologies in Moscow 2017, my life today would look much different.

I am honored that Prof. Dr. Alexander Shnirman who made invaluable contributions to our research field agreed to co-supervise this thesis.

Dr. Hannes Rotzinger greatly contributed to my work by sharing his interest and involvement in the intricacies of superconducting nanowires. Always with eyes toward the scientific questions more than any application, he encouraged all my efforts. As helpful as his scientific and technical know-how were his optimism and faith in my eventual success.

I thank Prof. Dr. Jared H. Cole for the great opportunity to spend time in his group at the RMIT in Melbourne, allowing me to experience physics from a new perspective in an awesome environment: not just upside down but from the theoretical side. Especially, I am thankful for his way of always finding the time to discuss my questions with sincere interest.

At KIT, our 4th floor community has in my eyes always stood out due to a sense of community. Thanks to everyone for being more than just colleagues: Jan Brehm who started his thesis at the same day, who will finish together with me, and who was a companion along the whole path of exams and exercise sheets up to this day; my office (and cabin) comrades Dr. Alexander Bilmes, Alexander Stehli, and Tim Wolz who never tired of sprawling discussions about life and resonators — noise-canceling headphones might be of help sometimes but the soothing of

shared experiences is invaluable; Jan Nicolas Voss with whom I undertook my first steps on thin wires and who shares many of my experiences with the joys and frustrations of nano fabrication; Dr. Andre Schneider who proved his patience and readiness to help with my countless questions ranging from python, time-domain measurements to the every-day issues of a PhD student; Maximilian Kristen who toward the end helped with fabrication and measurements and will be a worthy successor; and Micha Wildermuth who always helps everywhere and everyone. Some of the people who first introduced me to our group and the required methods already continued on their ways. Dr. Jochen Braumüller, Dr. Marco Pfirrmann, Dr. Steffen Schlör, and Dr. Sebastian Skacel all helped make the group what it is and what attracted not only me.

Without Lucas Radtke, Dr. Silvia Diewald, and the rest of the cleanroom team my wafers would have neither been written nor diced, nor had I been able to use maintained equipment. I am grateful for their support.

Also, I want to thank everyone I met at the RMIT and especially Tommy Bartolo, Akib Karim, Hugh Sullivan, and Dr. Samuel Wilkinson who all gave me such a warm welcome and great time in Melbourne. May no moat ever be too wide and no dupling too far.

Of course, I would not be at this point today were it not for my family, who not only gave me the opportunity to follow my path, which they never questioned, but also motivated me to become the curious and open-minded person I strive to be. And without my friends and flatmates life outside of the lab would have lacked all those bright sides that supply us with energy. I am very grateful to Dr. Ronald E. Ham for his encouragement while sharing his love of science and technology and especially for always taking me seriously.

To conclude, I am delighted to express my endless gratitude to my wife and best friend Anastasiia, without whom this conclusion might never have been reached. Whenever frustrations or doubt threatened to take over, you showed me with endless patience that there is so much more to life. Not only science but love too truly can be world-spanning.

Karlsruhe, December 21, 2020   Yannick Schön

Contents

1 Introduction

Quantum mechanics is often described as the theory treating the physics of every-thing small. While, in principle, dynamics at everyday scales follow the same laws, the intricacies of the quantum world are averaged out and classical formalisms become better suited for their description. Simple pendulums or guitar strings have well defined, quantized modes at frequencies ω_i. Their excitations, however, far exceed the energy quantum $\hbar\omega_i$, being of the order of 10^{-31} J at audible fre-quencies. So, continuous variables like displacement and amplitude well describe these systems. But even if one likes very quiet guitars, a single excitation would be impossible to control. This is due to the vast amount of participating atoms constituting and interacting with the system both mechanically and thermally. It is thus no wonder that when 2012 the Nobel prize was awarded to Serge Haroche and David Wineland for their groundbreaking experiments demonstrating the control of individual quantum transitions [Har13; Win13], these made use of systems inherently quantum and well isolated: Atoms passing through an optical cavity and laser cooled ions in an electromagnetic trap.

Since the proposal [SSH97] and eventual realization [NPT99] of the first super-conducting quantum circuits at the end of the 1990s, the cavity quantum electro-dynamics (cQED) approach pioneered by Serge Haroche has been successfully transferred to the superconducting circuit platform. These circuits employ elements resembling inductors and capacitors, well known from classical electrical circuitry, in the single excitation regime. Still, in contrast to the preceding experiments, these circuits extend over mesoscopic scales of many micrometers, incorporating a vast number of atoms[1]. The fact that these systems are still governed by a single quan-tum mechanical wave function is an impressive consequence of superconductivity. The order parameter, defining the phase transition such a circuit undergoes below its critical temperature, is precisely the macroscopic wave function governing the charge carriers in the superconducting condensate [GL50].

While the experiments have to be conducted in a setting well shielded from envi-ronmental and thermal influences at millikelvin temperatures, the fabrication and

---

[1] An aluminum circuit element of dimensions $(200 \times 200 \times 0.05)\,\mu m^3$ contains about 10^{14} atoms.

characterization of these circuits are possible at room temperature and greatly profit from technological advances pushed by the semiconductor industry. Additionally, while not superconducting, the circuit conductance at room temperature is in many cases a measure of the dynamics that emerge when cooled down [AB63a]. Their versatility has lead to a wide range of circuit designs with very different goals; and since Feynman's famous speech [Fey82] about simulating quantum mechanics with quantum mechanical systems, a lot has been achieved in the strive toward quantum information applications. However, while already proven a versatile tool, there is still a very active field of fundamental research concerning superconductivity and superconducting devices. So far, Josephson tunnel junctions are the dominant circuit element providing the nonlinearity, which is required to introduce anharmonicity into the energy spectrum, and allowing quantum interference to manifest in these circuits. They have therefore also been a steady object of study with regard to their performance and parameter spread limiting the lifetime of quantum states and the scalability of circuits [Kja+20].

In this thesis, we want to explore a different path: both by using superconducting nanowires as nonlinear element for quantum circuits as well as by using these highly sensitive circuits as a familiar environment for studies of the nanowires' physics. In contrast to custom engineered tunnel barriers, their nonlinearity arises purely from their material and small dimensions. Disordered superconductors can facilitate large kinetic inductances. Their structure gives rise to a reduced mean free path for the charge carriers and reduced superfluid density, thus increasing the kinetic energy contribution of the Cooper pairs. Granular aluminum, consisting of small superconducting grains embedded in an insulating oxide matrix, combines this property with low loss, making it suited for applications in high-impedance quantum circuits [Rot+16; Grü+19]. When scaled down to widths in the nanometer range, close to the dimensions of the internal granular structure of this material, the nonlinearity becomes large enough to be exploited for novel quantum circuits [Sch+20].

We address the question whether it is possible to realize a quantum circuit of a single granular aluminum layer in the design of an anharmonic oscillator and employing a nanowire as nonlinear element. To this end, we start by introducing the underlying physics and effects which can be observed in granular systems at reduced dimensions. In the following chapter, we present the circuit designs and fabrication processes derived for their realization. Also, the measurement framework, making experiments with these circuits possible, is introduced. Subsequently, two chapters are dedicated to our experimental results.

The demonstration of Rabi oscillations in such a circuit is an attractive goal as it proves the possibility to gain sufficient anharmonicity without a tunnel junction

or inter-layer contacts in a very compact design, and facilitates the controlled excitation of individual transitions. The system can then be studied to determine whether coherence prevails in the tunneling through the granular network of the wire. This is an especially intriguing question since their geometry invites comparison to weak links. In the latter, lengths far exceeding the superconducting coherence length ξ are predicted to suppress quantum interference of the two leads and eventually lead to the breakdown of superconductive charge transport. In contrast to these systems, however, our nanowires feature a much smaller $\xi \sim 8\,$nm [Vos+20] that allows for a well defined superconducting phase even in wires with a width of about 20 nm. This width, on the other hand, is in the order of the intrinsic grain sizes ($\sim 4\,$nm) and therefore allows for a manifestation of local dynamics. Still, in contrast to a Josephson junction, which is typically considered as a zero-dimensional tunnel contact without considerations of geometry, the latter must be expected to influence a nanowire's response. Increasing their length also increases the number of grain boundaries. The question then arises how much single boundaries influence the dynamics, or whether the anharmonicity of such a circuit is defined by its macroscopic properties. Circuits that allow the determination of this anharmonicity for different wire geometries can therefore be a valuable instrument. On top of an increased inductance in longer wires and the changed current-phase relation, the total inductance of a circuit fully made from a disordered superconductor plays a role. This can be studied by comparison to circuits in which parts of the circuit are shunted by a low inductance superconductor like pure aluminum. How far the intrinsic disorder affects the circuit's performance can be investigated by measuring their life- and coherence times. Compared to a single tunnel junction, the distribution of the phase drop over many grain boundaries could be advantageous since smaller electric fields couple less to local two-level fluctuators [MCL19].

Additionally, properties arise at such dimensions that are unique to these nanowires and are not observed in circuits, even of the same material, at larger scales. Depending on the nanowire geometry and resistance, very different transport regimes can be observed [Vos+20]. When the length or resistance is increased, the superconducting phase becomes susceptible to fluctuations until the ability to carry supercurrents is eventually fully suppressed [Fis86; Zai+97; SFK20]. Circuit elements operated in this insulating regime have been described as dual to Josephson tunnel contacts. One especially intriguing consequence is the possibility to realize circuits dual to Josephson arrays used in the modern voltage standard, which in turn could serve as a current standard [MN06]. With the nanowires studied in this project it is possible to observe the supercurrent, insulating, and a metallic-like intermediate regime all in the same circuit. This is possible because of an effect allowing us to reduce the wire resistance by applying short current pulses. Increas-

ing the current up to well above their critical current, the nanowire resistance can be permanently reduced. This then also allows a change of its transport regime, even from insulating to carrying a supercurrent [Vos+20].

One more goal of this thesis is the introduction of a method for DC characterization and adjustments of our nanowire circuits' transport properties. Combined with an anharmonic microwave oscillator design, the benefit here is threefold. First, better knowledge and control over the circuit parameters allow for a more quantitative understanding of their dynamic response. Already the measurement of their transition frequencies can yield insights into the dominant energy scales when parameters like resistance and critical current are known. Second, parameter spread occurring during fabrication can be reduced and yield increased. Third, circuits can be placed in atypical operating regimes, for instance close to the superconductor to insulator transition, to study how an increase of phase fluctuations affects the coherence of a circuit's oscillations.

2 Building blocks

2.1 Superconductivity in reduced dimensions

It took nearly fifty years until John Bardeen, Leon Cooper and John Schrieffer formulated a microscopic description of superconductivity [BCS57], known as the BCS theory. This is due to the counterintuitive nature of the underlying concept. Important impulses were the discovery of the isotope effect (transition temperature $\propto$ mass$^{-0.5}$) hinting at phonons as participants in superconductivity and the possibility of phonons mediating an attractive electron electron interaction [Max50; Frö50]. BCS expanded on these findings recognizing that any attractive interaction between electrons gives rise to a new state of energy lower than the Fermi sea, even at zero temperature [Tin04].

Scattering of electrons ($\mathbf{k}_1, \mathbf{k}_2 \rightarrow \mathbf{k}'_1, \mathbf{k}'_2$) depends on several conditions. First, the states must be accessible, meaning the Fermi surface is no longer sharp at $T = 0$. Considering the antisymmetric nature of fermionic wave functions and maximizing the combinations allowed to participate under conservation of momentum, it follows that the interaction will be most effective for pairs of equal momentum in opposite directions and with opposite spins ($\mathbf{k}^{\uparrow}, -\mathbf{k}^{\downarrow}$) — the so called Cooper pairs [Sch97].

The total energy can then be written as

$$E = \sum_{\mathbf{k}} 2\epsilon_{\mathbf{k}} v_{\mathbf{k}}^2 + \sum_{\mathbf{k},\mathbf{k}'} V_{\mathbf{k}\mathbf{k}'} v_{\mathbf{k}'} u_{\mathbf{k}} v_{\mathbf{k}} u_{\mathbf{k}'}, \tag{2.1}$$

where $\epsilon_{\mathbf{k}}$ is the kinetic energy relative to the Fermi surface, $v_{\mathbf{k}}^2$ the occupation probability of the states $\mathbf{k} \& -\mathbf{k}$ with $u_{\mathbf{k}}^2$ its opposite $1 - v_{\mathbf{k}}^2$. $V_{\mathbf{k}\mathbf{k}'}$ is the interaction potential for a transition between these states and is assumed constant $-V$ in an interval around the Fermi energy corresponding to the Debye frequency ω_{D}[1]. A

---

[1] $\hbar\omega_{\mathrm{D}}$ corresponds to the maximum phonon energy available to mediate the scattering.

variational ansatz then yields the functions $v_{\mathbf{k}}$ minimizing E, corresponding to the distribution function of the new superconducting ground state [Sch97]

$$v_{\mathbf{k}}^2 = \frac{1}{2} - \frac{\epsilon_{\mathbf{k}}}{2\sqrt{\epsilon_{\mathbf{k}}^2 + \Delta^2}}, \qquad \Delta = \frac{\hbar\omega_{\mathrm{D}}}{\sinh\left(\frac{1}{N_0 V}\right)} \simeq 2\hbar\omega_{\mathrm{D}}\exp\left(\frac{-1}{N_0 V}\right) \qquad (2.2)$$

where N_0 denotes the density of states at the Fermi surface. Δ thus is a measure for the widening of the distribution and the amount of participating states in k-space [Tin04].

The question then arises under which circumstances the interaction energy outweighs the excess kinetic energy. Comparison to the normal state energy yields a difference of $-N_0\Delta^2/2$, negative independently of V. Considering the situation of one pair missing, evaluating equation (2.1) for a single $\mathbf{k}$, and it being replaced by a single electron of energy $\epsilon_{\mathbf{q}}$ results in an energy increase of [Sch97]

$$E_{\mathbf{q}} = \sqrt{\epsilon_{\mathbf{q}}^2 + \Delta^2} \xrightarrow{q \to k_{\mathrm{F}}} \Delta. \qquad (2.3)$$

Δ thus corresponds to the *gap* between the lowest normal electron excitation at the Fermi level and the superconducting ground state.

For finite temperatures any state has an occupation probability given by the Fermi-Dirac statistics reducing the number of states available to pair binding. Taking this into account for the ground state energy and finding the minimum of the free energy density in terms of $v_{\mathbf{k}}^2$ allows for calculation of an implicit temperature dependence $\Delta(T)$ that can be evaluated numerically. For the critical temperature T_{c} at which the gap finally vanishes, comparison of $\Delta(T)$ with equation (2.2) yields [Sch97]

$$\Delta(0) = 1.764\, k_{\mathrm{B}} T_{\mathrm{c}}. \qquad (2.4)$$

The decrease of the gap with rising temperature is slow as long $\Delta \gg k_{\mathrm{B}}T$ since it is driven by thermal particle excitations above the gap, so called quasiparticles. Division of the implicit form of $\Delta(T)$ by equation (2.4) yields an approximation for the convergence of the gap toward T_{c} as [Tin04]

$$\Delta(T \to T_{\mathrm{c}}) \approx 1.74\sqrt{1 - \frac{T}{T_{\mathrm{c}}}}\Delta(0). \qquad (2.5)$$

Changes in the configuration of the superconducting state correspond to changes of the distribution function $v_{\mathbf{k}}^2$, which following equation (2.2) is confined to a range $\Delta k \sim 2\Delta k_{\mathrm{F}}/\epsilon_{\mathrm{F}}$. Together with equation (2.4) and the uncertainty principle,

the length scale for variations in the superconducting wave function Δx is given by the coherence length [Sch97]

$$\xi = 0.18 \frac{\hbar v_{\mathrm{F}}}{k_{\mathrm{B}} T_{\mathrm{c}}}. \tag{2.6}$$

It is worth noting that $u_{\mathbf{k}}$ and $v_{\mathbf{k}}$ can actually differ by a phase factor $\mathrm{e}^{\mathrm{i}\varphi}$ forming a relation between states with certain numbers of pairs and giving rise to the uncertainty relation between the number of pairs and the phase [Tin04]

$$|\Psi_N\rangle = \int_0^{2\pi} \mathrm{e}^{-iN\varphi/2} |\Psi_\varphi\rangle \quad \Rightarrow \quad \Delta N \Delta \varphi \gtrsim 1. \tag{2.7}$$

This corresponds to the phase of the superconducting wave function which is coherent on macroscopic scales allowing for non zeroing-out expectation values for the pair creation $\mathbf{k}^{\uparrow}, -\mathbf{k}^{\downarrow}$.

2.1.1 Ginzburg-Landau theory

Before BCS derived their microscopic theory, Vitaly Ginzburg and Lev Landau were able to construct a theory on the basis of second order phase transitions and symmetry breaking [GL50; GL65], which had been previously studied by Landau [Lan37]. While their theory was of phenomenological nature, it was later shown to be derivable from the BCS theory by Lev Gor'kov [Gor59].

The appearance of the superconducting phase is interpreted as additional order of a state with lower symmetry. As order parameter they assumed the appearance of an "'effective' wave function of the 'superconducting electrons'" [GL65]

$$\Psi = \sqrt{n_{\mathrm{s}}} \exp(\mathrm{i}\varphi), \tag{2.8}$$

where n_{s} is the superconducting electron density. Expanding the free-energy density F in terms of this order parameter near the phase transition ($T \sim T_{\mathrm{c}}$) gives

$$F_{\mathrm{s}0} = F_{\mathrm{n}} + \alpha |\Psi|^2 + \frac{\beta}{2} |\Psi|^4 \tag{2.9}$$

with F_{n} representing the energy in the normal state. To allow for an equilibrium situation with a finite value of Ψ below T_{c}, equation (2.9) must exhibit minima. From this follows that $\alpha < 0$ and $\beta > 0$ and

$$\frac{\mathrm{d}F_{\mathrm{s}0}}{\mathrm{d}|\Psi|^2}(\Psi_0) = 0 \quad \Rightarrow \quad |\Psi_0|^2 = -\frac{\alpha}{\beta} \quad \Rightarrow \quad F_{\mathrm{n}} - F_{\mathrm{s}0} = \frac{\alpha^2}{2\beta}. \tag{2.10}$$
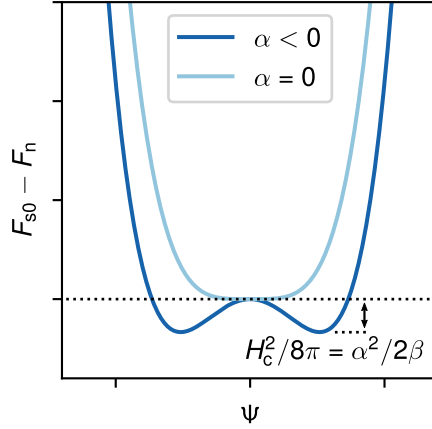
Figure 2.1: Symmetry breaking in the GL theory. Above T_c, the phase in the equilibrium at minimum free energy is arbitrary with Ψ being 0. This symmetry is broken in the superconducting state's ($\alpha < 0$) double well potential. The difference between both states will be overcome by a critical magnetic field of $H_c^2 = 4\pi\alpha^2/\beta$

Additionally considering the presence of electromagnetic fields, allowing for variations in Ψ due to said fields and requiring gauge invariance, equation (2.9) is extended to

$$F_{s0} \rightarrow F_s = F_{s0} + \frac{H^2}{8\pi} + \frac{1}{2m^*}\left|-i\hbar\nabla\Psi - \frac{e^*}{c}\mathbf{A}\Psi\right|^2, \tag{2.11}$$

where Gor'kov found that $e^* = 2e$ due to the pairing of the charge carriers in the BCS theory and $m^* = 2m_e$ with the electron mass m_e [Gor59; Sch97]. A critical magnetic field will suppress superconductivity when

$$\frac{H_c^2}{8\pi} = \frac{\alpha^2}{2\beta} \quad \Rightarrow \quad H_c^2 = \frac{4\pi\alpha^2}{\beta}. \tag{2.12}$$

Being defined as order parameter, $|\Psi_0|^2$ and thus also α must be 0 for $T > T_c$. Expansion to first order yields the empirically observed temperature dependence [Sch97]

$$H_c(T) = H_c(0)\left(1 - \frac{T^2}{T_c^2}\right). \tag{2.13}$$

2.1.2 Josephson coupling

By studying the voltage required for electronic tunneling through an insulating barrier, Ivar Giaever demonstrated the appearance of the superconducting gap when the lead becomes superconducting [Gia60]. Until Brian Josephson's prediction

of a tunneling current with vanishing resistance [Jos62], tunneling was however still thought to be driven by a voltage. Considerations of symmetry breaking and the uncertainty relation between the number and phase operators lead Josephson to the insight that a phase difference $\Delta\varphi$, not its time evolution, between two superconductors should coincide with an exchange of charges [Jos74].

Following Feynman's derivation [FLS11] we find a relation between the wave functions of the superconducting condensate in the leads, identified in the Ginzburg-Landau theory [GL50; GL65] as $\psi_i = \sqrt{n_i}\exp(i\varphi_i)$, where n denotes the charge density and φ the position dependent phase. If the tunnel barrier is thin enough to allow for a finite contribution of each wave function on the other side, we expect their overlap to induce a coupling. In the absence of magnetic fields, we can write the Schrödinger equations

$$i\hbar \begin{pmatrix} \dot{\psi}_1 \\ \dot{\psi}_2 \end{pmatrix} = \begin{pmatrix} \mathcal{H}_1 & K \\ K & \mathcal{H}_2 \end{pmatrix} \begin{pmatrix} \psi_1 \\ \psi_2 \end{pmatrix}. \tag{2.14}$$

Considering both leads in their respective ground state and allowing for an additional voltage drop V over the junction, the $\mathcal{H}_i$ amount to an energy of $\pm qV/2$ where $q = 2e$ for each Cooper pair. The off-diagonal corresponds to a coupling amplitude with the dimension of an energy. With the Ginzburg-Landau wave function (Eq. (2.8)), this results in the equations of motion for the charge densities and phases

$$\dot{n}_1 = \frac{2K}{\hbar}\sqrt{n_1 n_2}\sin(\Delta\varphi) = -\dot{n}_2 \tag{2.15}$$

$$\dot{\varphi}_1 = -\frac{K}{\hbar}\sqrt{\frac{\varphi_2}{\varphi_1}}\cos(\Delta\varphi) - \frac{eV}{\hbar} \qquad \dot{\varphi}_2 = -\frac{K}{\hbar}\sqrt{\frac{\varphi_1}{\varphi_2}}\cos(\Delta\varphi) + \frac{eV}{\hbar} \tag{2.16}$$

with $\Delta\varphi = \varphi_2 - \varphi_1 \equiv \varphi$.[2]

Under the assumption that both leads are of the same material and their charge carrier densities $n_1 = n_2 = n$ are not changed by a current in the vicinity of the junction, equation (2.15) becomes the first Josephson equation

$$j = \frac{2Kn}{\hbar}\sin\varphi = j_c\sin\varphi. \tag{2.17}$$

---

[2] More accurately and including the effects of external fields one can define a gauge-invariant phase as $\varphi = \Delta\varphi - (2\pi/\Phi_0)\int \mathbf{A}\,d\mathbf{s}$. [Tin04]

The critical current density j_c is a measure for the maximum superconducting current of the junction and is a characteristic of the material and junction design. Subtracting equations (2.16) gives the second Josephson equation

$$\dot{\varphi} = \frac{2eV}{\hbar} = \frac{2\pi}{\Phi_0} V \tag{2.18}$$

with the superconducting flux quantum $\Phi_0 = h/2e$.

Additional to the main consequence that a tunnel current can flow without resistance, this leads to the interpretation of the Josephson junction as nonlinear inductor with kinetic Josephson inductance $L_J = \hbar/2eI_c$ since

$$\frac{\partial I}{\partial \varphi}\frac{\partial \varphi}{\partial t} = \frac{2\pi I_c \cos\varphi}{\Phi_0} V \iff V = \frac{\Phi_0}{2\pi I_c \cos\varphi}\dot{I} = L_J \dot{I}. \tag{2.19}$$

Applying a constant voltage V_0 to a tunnel contact results in fast current oscillations. High frequency modulation of the applied voltage gives rise to steps of the tunnel current for frequencies of $\omega = 2eV_0/\hbar$ and multiples as confirmed by Sidney Shapiro [Sha63]. This effect today serves as the bases of the voltage standard.

While the absolute phase of the superconducting wave function is still not measurable, the phase difference over a junction and its time dynamics become observable through the Josephson effect [And70]. This gave a boost to applications of superconductivity beyond perfect conductance by allowing for direct observation of quantum interference effects and the eventual realization of macroscopic quantum devices.

The first proposed device considered two superconducting grains connected by a single Josephson junction [SSH97]. Analogous to the ansatz leading to equation (2.14), the Josephson coupling then mixes states with different numbers of Cooper pairs $|N\rangle$, $|N+1\rangle$ on the islands and a difference in the number of Cooper pairs on the two grains contributes an additional energy $E_C = e^2/2C_J$. Together, the Hamiltonian of a Josephson junction can be written [Bou+98]

$$\mathcal{H}_{JJ} = 4E_C \sum_N (N - N_g)^2 |N\rangle\langle N| - \frac{E_J}{2}\sum_N (|N\rangle\langle N+1| + |N+1\rangle\langle N|). \tag{2.20}$$

The factor 4 arises due to the fact that the charge carriers in this systems are Cooper pairs with charge $2e$. An offset charge N_g can be added by a voltage between the superconducting grains and the environment to which there always is a capacitance. The charging term then gives rise to a periodic parabolic dispersion and the second term splits the parabolas at the crossing points into bands. An illustration (Fig. 3.1) together with a discussion of different regimes is given in section 3.1.1.

Since charge and phase are conjugate variables (Eq. (2.7)), the second term in the Hamiltonian can be expressed in the basis of phase states via the Fourier transform

$$|\varphi\rangle = \sum_N e^{iN\varphi} |N\rangle \quad \Rightarrow \tag{2.21}$$

$$\mathcal{H}_J = -\frac{E_J}{4\pi} \int_0^{2\pi} d\varphi \left(e^{i\varphi} + e^{-i\varphi} \right) |\varphi\rangle \langle \varphi| . \tag{2.22}$$

Introducing the number and phase operators [Dev97]

$$\hat{N} = \sum_N N |N\rangle \langle N| \tag{2.23}$$

$$e^{i\hat{\varphi}} = \frac{1}{2\pi} \int_0^{2\pi} d\varphi e^{i\varphi} |\varphi\rangle \langle \varphi| , \tag{2.24}$$

the Josephson junction Hamiltonian in the operator notation becomes

$$\mathcal{H}_{JJ} = 4E_C \left(\hat{N} - N_g \right)^2 - E_J \cos(\hat{\varphi}). \tag{2.25}$$

Applying the Heisenberg equation to calculate the current flowing in such a system and the commutation relation $[\hat{\varphi}, \hat{N}] = i$, one finds

$$\hat{I} = -2e \frac{d\hat{N}}{dt} = -2e \frac{i}{\hbar} \left[\mathcal{H}_{JJ}, \hat{N} \right] = -2e \frac{i}{\hbar} \left[\hat{\varphi}, \hat{N} \right] \frac{\partial \mathcal{H}_{JJ}}{\partial \hat{\varphi}} = \frac{2e}{\hbar} E_J \sin \hat{\varphi}. \tag{2.26}$$

Comparison to the first Josephson equation (Eq. (2.17)) yields the relation for the Josephson energy

$$E_J = \frac{\hbar}{2e} I_c = \frac{\Phi_0}{2\pi} I_c. \tag{2.27}$$

An important step towards applications of this effect and the design of devices was done by Vinay Ambegaokar and Alexis Baratoff by calculating junction characteristics and their temperature dependence from measurable material properties by applying a Green's function approach to the microscopic BCS theory. In the situation of the junction connecting two identical superconductors with gap Δ (Eq. (2.4)), the Ambegaokar-Baratoff relation (AB) takes the form [AB63a; AB63b; Tin04]

$$I_c = \frac{\pi \Delta}{2eR_n} \tanh \left(\frac{\Delta}{2k_B T} \right) \xrightarrow{T \to 0} 2.77 \frac{k_B T_c}{eR_n}. \tag{2.28}$$

2.1.3 RCSJ model and phase slips

The environment of a tunnel contact strongly influences its dynamics. Wilbert C. Stewart and Dean E. McCumber derived a model incorporating these effects

by adding an additional shunt capacitance C_J and a shunt resistance R to the effective circuit of a tunnel contact [Ste68; McC68]. A capacitance exists even in an isolated junction between the metallization on both sides of the tunnel barrier and quasiparticles tunneling through it are subjected to its normal state resistance. The current through this so-called RCSJ circuit then becomes [Tin04]

$$I = I_c \sin \varphi + \frac{\hbar}{2eR} \dot{\varphi} + \frac{\hbar C_J}{2e} \ddot{\varphi}. \tag{2.29}$$

The stationary solution reproduces the first Josephson equation (2.17) for a zero-voltage tunnel current. Currents exceeding I_c correspond to a changing phase and are thus resistive. Equation (2.29) can be rewritten in the form

$$M\ddot{\varphi} + \eta\dot{\varphi} + E_J \frac{\mathrm{d}}{\mathrm{d}\varphi} U(\varphi) = 0 \tag{2.30}$$

$$U(\varphi) = -E_J \left(\cos \varphi + \frac{I}{I_c} \varphi \right) \tag{2.31}$$

corresponding to the equation of motion of a "phase particle" of mass $M = (\hbar/2e)^2 C_J$ in a potential $U(\varphi)$ and with damping $\eta = (\hbar/2e)^2/R$ [Tin04]. U has the form of a "tilted washboard" with the tilt given by the current (Fig. 2.2). The various limits of this model illustrate different regimes of tunnel junction dynamics. For small excitation and damping, the phase can oscillate around a minimum in the potential well with the plasma frequency $\omega_p = 1/(L_J C_J)^{1/2} = (2eI_c/\hbar C_J)^{1/2}$. When $I \geq I_c$, the potential minima disappear resulting in a resistive running state. The damping then determines how far the potential has to be tilted back until the phase particle is "retrapped" in a minimum giving rise to hysteretic I-V curves.

Already below I_c however, the barriers separating the potential wells can be overcome by different processes, increasing the phase by multiples of 2π. For instance, thermal fluctuations larger than the current dependent barrier height might lift the phase particle into an adjacent well (thermally activated phase slips or TAPS). For zero current, there is no preferred direction of this process so that the net effect averages out. With a given tilt however, this can result in diffusion of the phase, yielding a net $\dot{\varphi} > 0$ visible as non-zero resistance. Since the rate increases with increased tilt, an I-V curve in the presence of phase-diffusion will show pronounced rounding near I_c. At low temperatures ($kT \ll E_J$), direct tunneling, so called quantum phase slips (QPS), between the wells will dominate. [DMC85; Gio88; Bez12]

Generally, these dynamics are influenced both by environmental fluctuations and periodic excitations applied on purpose. The mentioned thermal fluctuations also directly impact the I_c. Additionally, a circuit might be subjected to charge or current
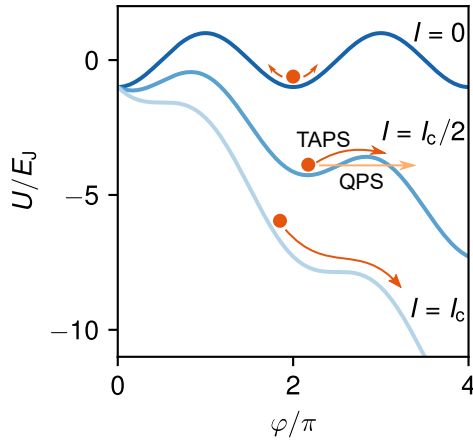
Figure 2.2: Illustration of the RCSJ model. The lines correspond to the potential energy $U(\varphi)$ of a "phase particle" for different currents I. For currents $\ll I_c$, its phase remains localized in one well in which it can oscillate with $\omega_p = 1/(L_J C_J)^{1/2}$. There is no favored direction for tunneling to an adjacent well. The current thus flows dissipationless. When the current is increased, the effective barriers in one direction decrease until it can be overcome either by thermal excitation or quantum tunneling resulting in increased diffusion of the phase particle and the onset of observed resistance. Once the critical current is exceeded, the phase can no longer be confined to one well. The phase roll-off gets faster with increasing current, corresponding to a resistively flowing current.

noise, leading to fluctuations of the tilt and thus the barrier height, or to phase noise.

When the insulating barrier of a tunnel contact becomes thicker, the superconducting coupling E_J is reduced, resulting in a diminishing I_c. In other words, the charge becomes more localized. From the argument that charge and phase are non commuting ($[\hat{\varphi}, \hat{N}] = i$), it can be understood that localization of either leads to fluctuations of the other. Especially in granular materials with a high normal state resistance, the phase can locally become susceptible to tunneling, resulting in an increased rate of QPS. [Fis86]

Finally, E_J can be suppressed so far that any externally applied phase required to drive an arbitrarily small current (Eq. (2.29)) results in a phase slip, equivalent to a flux quantum tunneling across the wire. This means that below a certain voltage V_c the circuit behaves insulating, while above it conducts resistively. In this regime, I_c is no longer suitable to describe the circuit's behavior. However, with the critical voltage V_c, a new measure can take its place.

It is important to mention that this insulating regime is still an effect of superconductivity. Above T_c, neither the supercurrent regime with dissipationless conductance up to I_c nor the insulating regime can be observed.

2.1.4 Duality of Cooper pair tunneling and phase slips

Hans Mooij and Yuli Nazarov proposed a model [MN06] that describes super-conducting nanowires in the insulating regime as an element dual to a Josephson tunnel contact. In analogy to the Hamiltonian describing the Josephson coupling (Eq. (2.20)), their ansatz considers one inductive energy contribution E_L from flux through a loop replacing the charging energy, and the phase slip energy E_S playing the role of a coupling term between states of different flux numbers. Already before, phase slips have been described as a process defining superconducting transport in thin wires [Zai+97]. This then yields a Hamiltonian equivalent to the one for a Josephson junction under the exchange of

$$E_J \leftrightarrow E_S \quad E_C \leftrightarrow E_L \quad N_g \leftrightarrow \Phi / \Phi_0, \tag{2.32}$$

where Φ is the externally applied magnetic flux. Consequently, the relation for the current through a junction in equation (2.29) is replaced by a relation for the voltage drop across an insulating phase slip element [MN06]:

$$V = V_c \sin\left(2\pi q\right) + 2eR\dot{q} + 2eL\ddot{q}. \tag{2.33}$$

The washboard potential of the RCSJ model (Fig. 2.2) then translates to one with respect to the charge, exhibiting maxima of E_S resulting in an expression for the critical voltage introduced in the previous section:

$$V_c = \frac{\pi}{e} E_S. \tag{2.34}$$

In a QPS element the charge is well defined in the regime $E_S \gg E_L$, meaning that any applied phase gradient results in phase slips without a current flowing.

One important consequence of this model is the expected dynamic response. Equivalent to the kinetic inductance introduced for a Josephson contact (Eq. (2.19)), a kinetic capacitance can be introduced for the phase slip element. This kinetic capacitance

$$C_{kin} = \frac{e}{\pi V_c \cos\left(2\pi q\right)} \tag{2.35}$$

exhibits a periodicity in dependence of the charge q in contrast to the phase periodicity of the Josephson inductance. The resulting dual to Shapiro steps then would manifest in regions of constant current when the QPS element is driven at microwave frequencies, which could then be applicable as a measure for a new current standard [MN06]. Implementation of such a device remains challenging [WLA19].

This model assumes QPS elements as homogeneous nanostructures with well defined properties. Experimentally, inhomogeneities can arise in geometry and material parameters during fabrication and naturally due to intrinsic disorder.

Designing a device operating in the desired regime requires a relation between the ratio of E_S/E_L and controllable parameters. This is more difficult in the low temperature regime of QPS where the Ginzburg-Landau formalism, which is often used to study effects affecting the superconducting order parameter, is applicable only in terms of extrapolation [Moo+15]. Treating QPS events as occurring on a length scale defined by the coherence length ξ and at wavelengths much longer than the wire length l_w, their rate is expected to scale with the latter while being suppressed with increasing width, which in turn for the same material reduces the normal state resistance R_n. Together with assumptions concerning the barrier shape and damping, an expression is found by

$$\frac{E_S}{E_L} = \alpha \left(\frac{l_w}{\xi}\right)^2 \frac{0.18}{\pi} \exp\left(-\beta \frac{R_q l_w}{\xi R_n}\right), \qquad (2.36)$$

where α and β remain phenomenological parameters and $R_q = h/4e^2$ the resistance quantum [Moo+15]. The numerical factor $0.18 = 1/1.764\pi$ stems from the prefactor of the gap (Eq. (2.4)) entering into the kinetic inductance and thus E_L (see also equation (2.38)).

2.1.5 Current and phase

The confinement of a superconducting current that gives rise to macroscopic quantum interference effects can also be realized in different circuit designs like point-contacts, bridges and weak links [Lik79]. This will, however, result in differing relations between critical current and resistance (Eq. (2.28)) as well as between supercurrent and phase (Eq. (2.17)). In view of our experiments employing nanowires, we focus on constrictions between large superconducting leads.

While for short, "dirty" weak links with a mean free path ℓ smaller than the wire l and coherence lengths ξ ($\ell \ll l \leq \xi$) the "ideal" Josephson behavior is recovered near T_c, this is not true for arbitrary temperatures [Lik79]. Igor' Kulik and Alexander Omel'yanchuk expanded the existing analysis by calculations for arbitrary temperatures (KO-1) [KO75]. Figure 2.3 a) shows how for $T \to 0$ the current-phase relation (CPR) gets distorted and reaches a maximum at 1.32 times the I_{c0} given by the AB relation (Eq. (2.28)).

When the length is increased, the maximum supercurrent decreases and shifts to phases $> \pi/2$ (Fig. 2.3 b)). At a critical length $l_c \approx 5\xi$, the CPR becomes
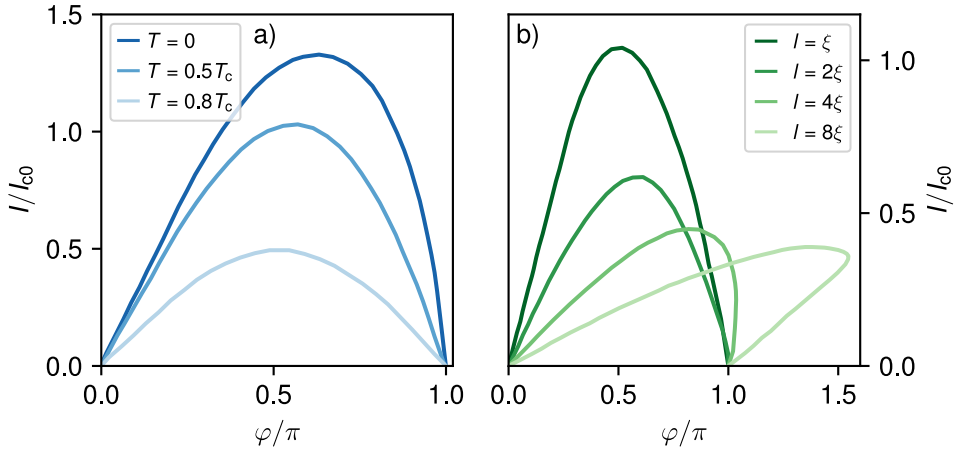
Figure 2.3: Kulik-Omel'yanchuk model for the current-phase relation of a "dirty" weak link. (a) The CPR in a short weak link takes a skewed form with a maximum of $1.32I_{c0}$ in comparison to the Ambegaokar Baratoff relation for a tunnel contact. At higher temperatures I_c decreases and the sinusoidal form is recovered. **(b)** While increasing length relative to the coherence length ξ, the skewness increases until the CPR becomes multi-valued. *With data from [Lik79].*

multi-valued and the conduction thus hysteretic, marking the onset of depairing by giving rise to a phase slip center [Lik79]. While the CPR tilts, the sine shape transitions into a more linear and finally sawtooth-like shape [Vij+09]. The weak link is regarded merely as facilitating the interference of the leads' superconducting wave functions over longer distances. When the length is increased further, these effects thus must vanish and the link becomes either a simple superconducting or normal conducting wire [Lik79].

While this model is instructive in connecting the different regimes and limits of the Josephson effect, it is important to note the differences with regard to the disordered nanowires studied in this thesis which will be outlined in the following section.

A different model (with different limitations) treating a homogeneous chain of effective tunnel junctions is discussed in section 2.2.2.

2.2 Disordered superconducting nanowires

Having introduced the physical models describing superconducting systems in reduced dimensions, we now want to shift toward effects arising in materials with

intrinsic disorder as well as introduce the material and nanowires used throughout this project.

2.2.1 Granular aluminum

In early experiments around the discovery of superconductivity in the lab of Heike Kamerlingh Onnes [Kam11] that were made possible by the realization of a liquid helium cryostat, a lot of effort was put into procuring pure material samples for the study of their resistances at low temperatures. Underlying was the discussion whether the resistance in a pure metal would continue to decrease until $T = 0\,\mathrm{K}$ or level off and increase [Kel02]. Not long after, however, Kamerlingh Onnes noted that this purity might not have been required since even amalgam became superconducting [DK10]. Today it is known that impurities can even increase the transition temperature of a material [CLS59].

Already before the microscopic BCS theory depending on phonons as mediators of the Cooper pair coupling, the impact of different ways of material preparation on T_c were studied. In aluminum evaporated on a cold surface, a disordered structure arose that gave rise to an increased T_c, which however vanished after heating to room temperature [BH54]. Later, this increase was studied in films produced in an atmosphere containing small amounts of oxygen [ACC66]. The resulting *granular* aluminum retained its T_c after thermal cycling [CA68].

In the models discussed in the previous section, the superconducting material itself was considered as homogeneous. For a disordered material like granular aluminum, it became clear that the intrinsic disorder strongly affects its properties. To explain the high normal state resistance and eventual suppression of superconductivity when the resistance per material square $R_\square$ became larger than the resistance quantum $R_\mathrm{Q} = h/4e^2 = 6.45\,\mathrm{k\Omega}$, the grains were considered as a network separated by tunnel barriers [Deu+73]. The transition to metallic or even insulating behavior is then explained by an increase of phase slips and the resulting charge localization on the superconducting islands as described for a single junction in section 2.1.3 [Fis86; Jae+89].

With the appearance of superconducting quantum circuits at the end of the last century, superconducting materials found refreshed attention from a new viewpoint. Now with an eye toward applications and with advanced fabrication techniques, microwave equipment and cryogenic environments, the research focus shifted to the behavior and performance of these materials when embedded in complex experimental circuits. On the other hand, new measurement techniques also gave
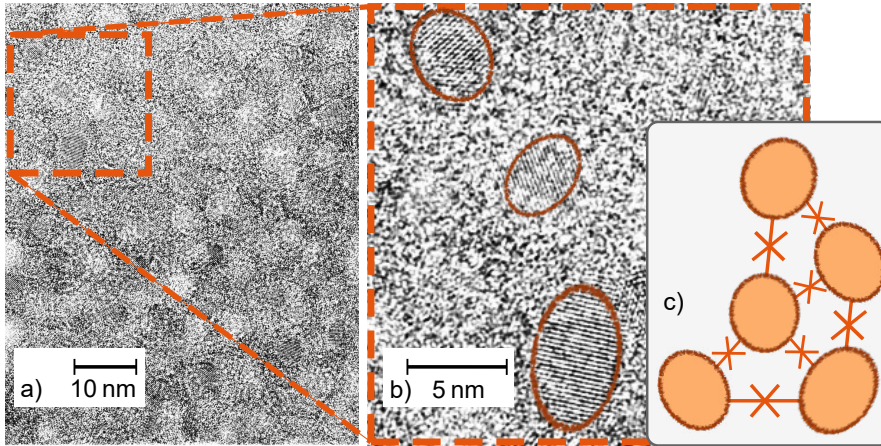
Figure 2.4: Transmission electron microscopy (TEM) of a granular aluminum film and sketch.
The TEM measurements were performed at the Laboratorium für Elektronenmikroskopie at KIT.
(a) Granular aluminum films consist of pure aluminum grains (visible as diffraction pattern) of
around 4 nm size embedded in an insulating aluminum oxide matrix. **(b)** Zoom in on an image
region with several distinct pattern of aluminum grains. **(c)** The material then can be thought of as
a disordered network of superconducting grains connected via tunnel barriers.

new drive to the research of fundamental effects of superconductivity. Individual
quantum transitions became observable in custom engineered circuits. [SFK20]

The granular aluminum used in the presented work features pure aluminum
nano-crystallites embedded in insulating amorphous aluminum-oxide. The grain
sizes range between 3–4 nm as determined by transmission electron microscopy
(Fig. 2.4) [Rot+16]. It can be fabricated with a wide range of normal state resistances
(Sec. 3.2.1) which, when structured into nanowires, translate into very different
transport regimes (Sec. 2.2.3). In films of around 20 nm thickness and kilo-ohm
resistances, the critical temperature is around 1.8 K. Due to its large kinetic induc-
tance, circuit elements can feature a large impedance and microwave frequencies
in resonators of very compact designs. It also found applications in microwave
kinetic inductance detectors [Maz20]. In combination with low loss observed in res-
onators [Rot+16], these properties make granular aluminum an attractive material
for applications in high impedance quantum circuits [Grü+18; Grü+19; Sch+20].

Aluminum and its insulating oxide are still the most widely used materials in
Josephson junctions for quantum circuits due to performance and the straight-
forward fabrication by in situ oxidization. Here, they make up the structure of a
material that can be structured into nanoscopic dimensions where dynamics arising
from the internal disorder manifest. Already in larger circuit elements, however,
the kinetic inductance features an intrinsic nonlinearity.

By calculating the transition probabilities between excitations of different states, Mattis and Bardeen found an expression for the ratios of complex superconducting σ_s and normal state conductivities σ_n. For frequencies and temperatures far below the superconducting gap at $0\,\mathrm{K}$, $\Delta_0 = 1.764\,k_\mathrm{B}T_\mathrm{c}$ [Tin04], the quasiparticle contribution to the conductivity $\Re(\sigma)$ vanishes and the relevant ratio becomes [MB58; Tin04]

$$\frac{\Im\sigma_s}{\sigma_n} = \frac{\pi\Delta(T)}{\hbar\omega} \tanh\left(\frac{\Delta(T)}{2k_\mathrm{B}T}\right). \tag{2.37}$$

The imaginary conductance relates to a kinetic inductance $L_k = Z/i\omega$. This kinetic inductance is a property inherent to the motion of the charge carriers in contrast to geometric inductances arising from the interplay with induced magnetic fields. With $Z = \mathrm{i}l/wt\Im\sigma_s$, the normal state sheet resistance $R_\square = 1/t\sigma_n$ and the number of squares $n = l/w$, this yields [Ann+10]

$$L_k = nR_\square \frac{\hbar}{\pi\Delta(T)\tanh\left(\frac{\Delta(T)}{2k_\mathrm{B}T}\right)} \xrightarrow{T\to0} 0.18\frac{\hbar}{k_\mathrm{B}T_\mathrm{c}}nR_\square. \tag{2.38}$$

While $T \ll T_\mathrm{c}$ and $\Delta = \Delta_0$ is usually justified by our experimental conditions, the current dependence of the gap can not be neglected and

$$\frac{L_k(I)}{L_k(0)} = \frac{\Delta_0(0)}{\Delta_0(I)}. \tag{2.39}$$

For small currents, an approximation is found with the Ginzburg-Landau theory by [ASB89]

$$\frac{L_k(I)}{L_k(0)} \approx 1 + \frac{4}{27}\frac{I_\mathrm{c}^2}{I_\mathrm{c}^2} \propto \frac{I^2}{I_\mathrm{c}^2}. \tag{2.40}$$

2.2.2 A model for the nonlinearity

For sufficiently large granular structures in which local inhomogeneities are averaged out, the picture of a disordered network of tunneling junctions can be reduced to a linear chain of effective junctions with length l. Through this simplification, the equations of motion for the phase drop across the n-th junction φ_n can be derived by applying Kirchhoff's circuit laws, considering an external excitation at the m-th junction in the middle of the chain [Mal+18]. Thus

$$\frac{\hbar C_0}{2e}\frac{\mathrm{d}^2\varphi_n}{\mathrm{d}t^2} = 2I_{n+1} - I_{n+2} - I_n + \delta_{m,n}I_\mathrm{ext}\cos(\omega t) \tag{2.41}$$

where (following Eqs. (2.17) and (2.29))

$$I_n = I_\mathrm{c}\sin(\varphi_n) + \frac{\hbar C_\mathrm{J}}{2e}\frac{\mathrm{d}^2\varphi_n}{\mathrm{d}t^2}. \tag{2.42}$$
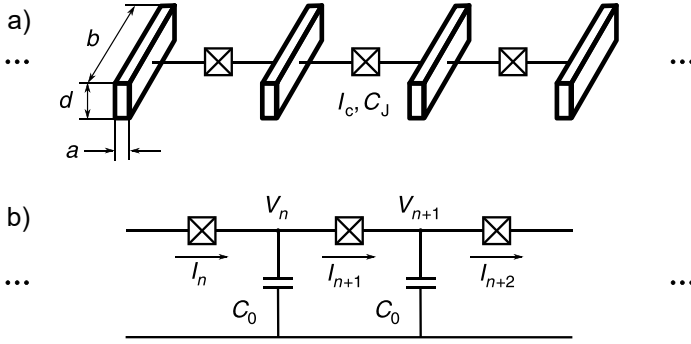
Figure 2.5: Schematic of a granular aluminum line modeled as a series array of effective junctions. (a) The line is made from a material film of thickness d, has a width b and length l. The latter is divided in parts of length a which represent the superconductive material separate by barriers forming the effective junctions with equal critical currents I_c and capacitance C_J. **(b)** Circuit diagram representation of the model. I_n denotes the current flowing through the n-th junction. The resulting island's self-capacitance is C_0. *Cutout from Fig. 1 in [Mal+18] under [CC-BY]*

As for the critical current, also the junction capacitance C_J and the capacitance to ground C_0 are assumed equal for the effective junctions. The derived equation of motion can be written in terms of derivatives in the continuous limit. The dispersion relation is then obtained by using the different current distributions of the resonance modes as ansatz [Mal+18], giving

$$\omega_n = \frac{na\pi}{l}\sqrt{\frac{2eI_c}{\hbar\left(C_0 + \frac{n^2\pi^2a^2}{l^2}C_J\right)}} \tag{2.43}$$

where a is the length of one effective junction. The modes converge to the plasma frequency of the chain when $n \to l/a$.

In a nonlinear system, the spectrum depends on the strength of the excitation. In the presented model, the Kerr coefficients are derived by solving the equation of motion under consideration of damping and amount of photons exciting the resonance. This leads to the expression for self- and cross-Kerr coefficients between the first and n-th mode [Mal+18]:

$$K_{11} = \frac{3}{16}\pi ea\frac{\omega_1^2}{j_c V_{\text{chain}}} \quad \text{and} \quad K_{1n} = \frac{1}{4}\pi ea\frac{\omega_1\omega_n}{j_c V_{\text{chain}}} \quad \text{with} \quad n > 1. \tag{2.44}$$

V_{chain} is the volume of the chain and j_c its critical current density. For different circuit designs employing granular aluminum as nonlinear inductor, the mode spectrum will differ. Due to the self-Kerr of the fundamental mode, its excitation by a photon induces a shift of its frequency to $\omega = \omega_1 - K_{11}$. A second photon of

the same frequency ω_1 can only stimulate emission, allowing for a control over the mode excitation.

By relating equation (2.44) with the current induced by a single photon excitation $I^2 \propto 1/L_J$, the derived nonlinearity exhibits the dependency found in equation (2.40) as $K_{11} \propto (I/I_c)^2$.

Limitations of this model are found when averaging breaks down and the assumption of effective junctions with equal effective parameters is no longer justified. This is to be expected for structures with dimensions comparable to the scale of grain sizes and local variations.

2.2.3 Three phases in a single nanowire

We have introduced how restricting the superconducting order parameter, for instance by geometric constraints, gives rise to effects that can be exploited for the creation of novel devices. Granular aluminum was introduced as a material with intriguing properties arising due to its intrinsic disorder. Now, we want to introduce properties specific to nanowires fabricated from granular aluminum films. As stated in the previous section, the disorder plays an increasing role when the dimensions are reduced leading to deviations from macroscopic effective models. This disorder is also an important difference compared to the weak links discussed in section 2.1.5. In that case, the material itself was taken as homogeneous and the constraints purely geometric. In granular aluminum, the coherence length of $(8.0 \pm 0.4)\,\text{nm}$ [Vos+20] is much shorter than in pure aluminum. Therefore, even in very narrow structures of about 20 nm width, the superconducting order parameter can still be well defined. The phase fluctuations are then induced by the very local barriers. While these models are valuable to understand the qualitative dependencies, their precise form and limits, for instance in regard to the length dependence, should be expected to differ. Additional to quantitative differences, there are, however, also properties unique to our granular aluminum nanowires.

When the width of a granular nanowire is constrained enough to limit the number of current paths, it becomes susceptible to alterations. In room temperature resistance measurements we observe a quasi continuous, permanent decrease of the wire's normal state resistance R_n when the amplitude of current pulses I_p, applied to the wire, is increased. At cryogenic temperatures, reduced noise allows for more precise transport measurements, allowing for the observation of discrete steps in the resistance change (Fig. 2.6a). The strength of this effect depends strongly on the wire geometry. In longer wires, we observe finer steps and a wider accessible resistance range. For wide structures the effect is diminished by the existence of
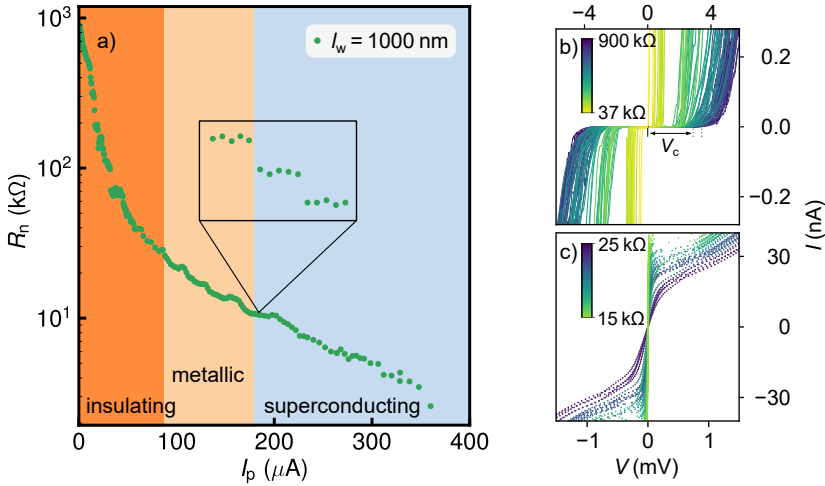
Figure 2.6: Current transport regimes in a single nanowire. (a) Decrease of the normal state resistance R_n of a 1000 nm long nanowire due to the application of current pulses. The change is permanent. For further decrease, the current pulse amplitude I_p has to be increased. Small increments of the pulse amplitude reveal steps in R_n. This agrees with discrete modifications in a disordered barrier network. **(b)** The same nanowire first shows insulating behavior at mK temperatures. I–V curves show a pronounced critical voltage V_c above which the wire conducts resistively. Current pulses decreasing the wire's R_n also reduce its V_c. **(c)** Once R_n is reduced far enough, the wire exhibits a metallic-like intermediate regime with an increasing slope around zero current. Further pulses and reduction of R_n finally lead to a transition to the supercurrent regime, where the wire exhibits zero resistance up to its critical current I_c above which it conducts resistively. I_c can then be further increased. Repeated application of current pulses and characterization offers a method to precisely control a nanowire's transport properties (patent pending). [Vos+20]

too many parallel conduction paths. Additionally, the superconducting behavior is strongly affected [Vos+20].

From the behavior of two-dimensional granular films it can be expected that above a certain resistance threshold the wire will not carry supercurrents anymore. As this depends on the resistance per square, resistances far exceeding R_Q can be realized in narrow structures while still permitting supercurrents. At the same time, this facilitates circuit elements with very limited critical currents. When the resistance, or wire length, is increased even further, the nanowires not only stop becoming superconducting but exhibit insulating behavior (Fig. 2.6). That this is in fact an effect based on superconductivity is clear, since it disappears above T_c where these wires exhibit highly resistive normal conductivity. Between these two regimes, we observe a nonlinear metallic-like behavior. There, I-V curves exhibit a clear resistive tilt and a distinct zero-bias anomaly: a higher resistance in vicinity of the zero-bias point. The nature of this regime and the origin of this anomaly are a matter of active research also for two-dimensional films [SFK20]. The described

ability to reduce the nanowire resistance in situ allows for studying the different regimes in a single nanowire [Vos+20].

A possible explanation for this resistance reducing process again makes use of the picture we have of the wire's internal structure. "Classical" Josephson junctions can be pinched by application of a voltage large enough to break through the insulating layer [AR63]. At this point, one can observe an altered Josephson effect and a strongly increased critical current. For a wire, the modification of a single barrier in the matrix can result in a decrease of the barrier amount or a shift of the effective current path. This is corroborated by the observation of discrete steps in the resistance trend.

The three different current transport regimes can be distinguished by the ratio of phase slip energy E_S and inductive energy E_L introduced in section 2.1.4. For the phenomenological parameters in equation (2.36) values can be derived from measurements of V_c in dependence of R_n (Eq. (2.34)). Fitting data obtained from the nanowires used in this experiment are $\alpha = 0.07$ and $\beta = 0.49$ [Vos+20]. The observed change of transport regime (Fig. 2.6) is then attributed to alterations in the granular structure influencing R_n and therewith E_S. For values of $E_S/E_L \gtrsim 10^{-2}$ any applied phase gradient leads to a high rate of 2π phase slips resulting in insulating behavior. A smaller phase slip energy corresponds to a stiffer phase. Superconducting behavior is observed for $E_S/E_L \lesssim 10^{-4}$. [Vos+20]

Together with the material properties, we now have three ways of controlling superconductivity in granular aluminum nanowires. First, parameters during the sputter deposition define the granularity and resistance of the two dimensional film. Secondly, design parameters like length and width set the accessible energy scales for a given film.

Finally, by applying high current pulses to our nanowires we are able to reduce R_n in situ, even allowing for a change of the superconductive regime.

2.3 Circuit quantum electrodynamics

A big challenge regarding experiments with quantum systems is found in maintaining the necessary protection from environmental fluctuations while making it accessible to measurement. In 2012 Serge Haroche won the Nobel price for pioneering work on cavity quantum electrodynamics. Embedding single atoms in a high quality optical cavity enabled his group to study numerous fundamental quantum effects [Bru+96; Har13]. Circuit quantum electrodynamics (cQED) applies this approach to superconducting quantum circuits [Bla+04].

To observe individual quantum transitions, the energy of the thermal bath surrounding it must be lower than the level distance ($k_\mathrm{B}T \ll E_{ij}$) and their separation larger than their linewidth ($\hbar\delta\omega_{i,j} \ll E_{ij}$) [Dev97]. The microwave band (4 to 12 GHz) mostly used in superconducting cQED satisfies the first condition for temperatures below 50 mK and a variety of circuit designs and materials have fulfilled the second [BGO20].

2.3.1 Readout and control

At this point, without addressing the realization, we imagine a circuit featuring one single-mode oscillator and one two-level system or artificial atom that will be called qubit. The first is described by the Hamiltonian of the harmonic oscillator $\mathcal{H}_\mathrm{r} = \hbar\omega_\mathrm{r}\hat{a}^\dagger\hat{a}$, where $\hat{a}^\dagger\hat{a} = \hat{n}$ are the common bosonic creation and annihilation operators. The second, due to its similarity to a spin-half system with states $|\uparrow\downarrow\rangle$, is expressed through the Pauli matrices σ_i as $\mathcal{H}_\mathrm{q} = \hbar\omega_{01}\sigma_z/2$. A coupling between these two can be mediated capacitively by an electric field acting on the qubit's dipole moment. Under consideration of low field amplitudes and spatial variations with respect to the qubit size, the interaction can be expressed in terms of an effective coupling g_r

$$\mathcal{H}_\mathrm{int} = \hbar g_\mathrm{r}\sigma_x\left(\hat{a}^\dagger + \hat{a}\right) \propto \mathbf{p}\cdot\mathbf{E}. \tag{2.45}$$

As long as g_r is much smaller than the qubit and resonator frequencies, the counter-rotating terms resulting from equation (2.45) as $\sigma_+\hat{a}^\dagger + \sigma_-\hat{a}$ can be neglected and all terms combined give the Jaynes-Cummings Hamiltonian in the so-called rotating wave approximation [WM08; HR06; JC63]

$$\mathcal{H}_\mathrm{JC} = \hbar\omega_\mathrm{r}\hat{a}^\dagger\hat{a} + \frac{\hbar}{2}\omega_{01}\sigma_z + \hbar g_\mathrm{r}\left(\hat{a}\sigma_+ + \hat{a}^\dagger\sigma_-\right), \tag{2.46}$$

where $\sigma_\pm = (\sigma_x \pm i\sigma_y)/2$. The coupling g lifts the degeneracy of the states $|n,\uparrow\rangle$ & $|n+1,\downarrow\rangle$ and gives rise to the new eigenstates $|n,\pm\rangle$ [Bla+04]

$$|n,+\rangle = \cos\gamma\,|\downarrow,n\rangle + \sin\gamma\,|\uparrow,n+1\rangle \tag{2.47}$$

$$|n,-\rangle = -\sin\gamma\,|\downarrow,n\rangle + \cos\gamma\,|\uparrow,n+1\rangle \tag{2.48}$$

with mixing angle $\gamma = \arctan(2g_\mathrm{r}\sqrt{n+1}/\Delta_\mathrm{r})/2$ and detuning $\Delta_\mathrm{r} = \omega_{01} - \omega_\mathrm{r}$. Their eigenenergies are given by

$$E_{n,\pm} = (n+1)\hbar\omega_\mathrm{r} \pm \frac{\hbar}{2}\sqrt{4g_\mathrm{r}^2(n+1) + \Delta_\mathrm{r}^2} \tag{2.49}$$

$$\overset{\Delta^2 \gg g^2}{\approx} (n+1)\hbar\omega_\mathrm{r} \pm \left(\frac{\hbar}{2}\Delta_\mathrm{r} + \hbar(n+1)\frac{g_\mathrm{r}^2}{\Delta_\mathrm{r}}\right). \tag{2.50}$$

In the so-called dispersive limit ($\Delta_\mathrm{r} \gg g_\mathrm{r}$), the mixing contribution is small and the energies differ from the uncoupled situation only by a small dispersive shift. As seen from equation (2.50) the mode excitation energies

$$E_{n+1,+} - E_{n,+} \approx \hbar\omega_\mathrm{r} + \hbar\frac{g_\mathrm{r}^2}{\Delta_\mathrm{r}} \qquad E_{n+1,-} - E_{n,-} \approx \hbar\omega_\mathrm{r} - \hbar\frac{g_\mathrm{r}^2}{\Delta_\mathrm{r}} \tag{2.51}$$

differ by a factor $\hbar\chi = \hbar g^2/\Delta_\mathrm{r}$ depending on the qubit's state, thus allowing its measurement by observation of the readout mode's frequency. This is called *dispersive readout* and a form of quantum nondemolition measurement. [Bla+04; Sch07].

For control or *manipulation* of the qubit, one can make use of the introduced interaction by applying an additional drive tone, also corresponding to a single mode field, near the qubit transition frequency ω_{01}. The Hamiltonian of the qubit-drive system is equivalent to the one above. This is expressed by changing all indices $\mathrm{r} \to \mathrm{m}$. On resonance ($\Delta_\mathrm{m} = 0$), the energies of the interacting system are split by $2g_\mathrm{m}\sqrt{n+1}$ and mixing is maximal. Since $|\uparrow\downarrow\rangle$ are no longer eigenstates of the coupled system, it will oscillate between them with the vacuum Rabi frequency $\Omega_0 = g_\mathrm{m}$.

Under consideration of detuning between drive and qubit transition, the Rabi frequency becomes

$$\Omega = \sqrt{g_\mathrm{m}^2 + \Delta_\mathrm{m}^2} \tag{2.52}$$

where the coupling g_m, combining prefactors of $\mathcal{H}_\mathrm{int} = -\mathbf{p} \cdot \mathbf{E}$, is proportional to the driving field amplitude [HR06]. At the same time, a detuned drive will excite the qubit only partially as the mixing angle γ becomes smaller. Arbitrary states can be prepared by applying drive pulses of varied length and with relative phases. Since the manipulation tone is far detuned from the readout resonator's frequency, the reflected signal does not carry information about the latter and therefore does not constitute a measurement of the qubit state [Bla+04].

2.3.2 The quantum state

An arbitrary state of a quantum system with two-dimensional Hilbert space (qubit) can be written as

$$|\Psi\rangle = \alpha\,|g\rangle + \beta\,|e\rangle = \cos\left(\frac{\theta}{2}\right)|g\rangle + \sin\left(\frac{\theta}{2}\right)\mathrm{e}^{\mathrm{i}\phi}\,|e\rangle\,. \tag{2.53}$$

This represents a vector to a point on the surface of a sphere, commonly called Bloch sphere. In contrast to a classical system which might exhibit time dependent

state probabilities, the quantum state is defined by probability amplitudes that can be complex numbers and allow for interference and quantum superpositions of the basis states. This is the foundation for applications in quantum information processing. [HR06]

An oscillation between the system's states as introduced in the previous section equates to a rotation of the polar angle θ. Readout of the qubit corresponds to a projection onto the z-axis. Each of the eigenstates is then measured (for instance by observing a readout resonator's shifted frequencies) with the probabilities

$$|\langle g \mid \Psi \rangle|^2 = \cos^2 \left(\frac{\theta}{2} \right) \quad \text{and} \quad |\langle e \mid \Psi \rangle|^2 = \sin^2 \left(\frac{\theta}{2} \right). \tag{2.54}$$

Determination of the qubit state thus requires repeated state preparation and readout.

For a qubit with an excitation energy $\hbar\omega_{01}$, the Hamiltonian yields the unperturbed system's time evolution

$$e^{-i\mathcal{H}t/\hbar} |\Psi(0)\rangle = e^{-i\omega_{01}t/2} \cos\left(\frac{\theta}{2} \right) |g\rangle + e^{i\omega_{01}t/2} \sin\left(\frac{\theta}{2} \right) e^{i\phi} |e\rangle. \tag{2.55}$$

Since only the relative phase can manifest itself in measurements, the above is equivalent to

$$|\Psi(t)\rangle = \cos\left(\frac{\theta}{2} \right) |g\rangle + \sin\left(\frac{\theta}{2} \right) e^{i(\phi - \omega_{01}t)} |e\rangle \tag{2.56}$$

representing a precession of the state vector around the z-axis with angular frequency ω_{01}.

2.3.3 Decay and dephasing

Quantum systems are fragile. In the same way any measurement of a quantum state can only yield one of the system's eigenstates, which in turn can be interpreted as collapsing its wave function, any interaction with the environment can destroy quantum superposition. Big effort is thus put into isolating the experiment from its environment while still allowing for control and measurement.

Perturbations of the qubit state can act either on θ or ϕ. One can thus distinguish processes involving frequencies close to the qubit transition, which are allowing for energy dissipation, from such detuned from ω_{01}, leading to variations of ω_{01} [Ith+05]. Following equation (2.55), random variations in $\mathcal{H}$ result in deviations from the unperturbed phase evolution, called dephasing. For a description of

decoherence inducing processes it is helpful to introduce the density operator for a qubit state (Eq. (2.53))

$$\hat{\rho} = |\Psi\rangle\langle\Psi| = \begin{pmatrix} |\alpha|^2 & \alpha\beta^* \\ \alpha^*\beta & |\beta|^2 \end{pmatrix}. \tag{2.57}$$

The diagonal elements contain the probabilities of finding the qubit in either of its eigenstates. The time scale associated with energy relaxation causing their decay is called T_1. Decoherence is expressed by the decay of the phase information carrying off-diagonal elements[3] on the time scale T_2 [Ith+05]. Since we are dealing with projective measurements, recording these processes depends on repeated preparation and measurement. This is true even if the signal to noise ratio was high enough to determine the state in a single measurement. These repetitions are independent of each other and therefore constitute an ensemble for which the density operator introduced in equation (2.57) translates into the density matrix

$$\rho = \sum_i p_i |\Psi_i\rangle\langle\Psi_i| \tag{2.58}$$

in which p_i is the probability to find a certain part of the ensemble in the state $|\Psi_i\rangle$. The expectation value for an observable $\hat{O}$ for this system then is given by

$$\sum_i p_i \langle\Psi_i|\hat{O}|\Psi_i\rangle = \text{Tr}(\hat{O}\rho) \quad \text{while} \quad \text{Tr}(\rho) = 1 \tag{2.59}$$

since the system has to be found in one state. The resulting *mixed* state is no longer represented by a unit vector on the Bloch sphere, even while the individual $|\Psi_i\rangle$ remain normalized. [HR06]

Measurement of the qubit life- and coherence times can be achieved by applying different schemes of drive pulses. For a T_1 measurement, the qubit is irradiated with a microwave pulse of frequency ω_{01} and with a length equivalent to one half Rabi period. This brings the qubit from its ground to its excited state and is thus called a π-pulse. After a varied waiting period Δt, a second microwave pulse is applied with the readout resonator's frequency ω_r. The measured amplitude and phase of the scattered signal yield information about the dispersive shift and thus reveals the qubit's state after Δt (Sec. 2.3.1). While, aside from noise on the measurement signal, each measurement pulse can only reveal either $|e\rangle$ or $|g\rangle$, the relative population is attained by repetition and averaging. This population then decays $\propto \exp(-t/T_1)$. It is assumed that the qubit is thermalized at temperatures $k_B T \ll \hbar\omega_{01}$ so that channels into which the qubit excitation can dissipate do not in turn excite the qubit. [Vio+02]

---

[3] It is worth noting that multiplication by a global phase factor does not change $\hat{\rho}$.

To measure decoherence, the system first needs to be prepared in a state with non vanishing off-diagonal components in $\hat{\rho}$. Typically, a $\pi/2$-pulse is applied to bring the state vector to the Bloch sphere's equator $|\Psi\rangle = (|1\rangle + |0\rangle)/\sqrt{2}$. After the phase has been allowed to freely evolve for a time Δt, the qubit state is projected back on the z-axis with a second $\pi/2$-pulse. With perturbations introducing random phase fluctuations over a given time span $\Delta\phi(t)$, the phase information decays $\propto \exp(-\langle\Delta\phi^2\rangle/2)$. The result of the second $\pi/2$-pulse then depends on the phase difference between the state vector and the drive. When driven on resonance, both phases are synchronized and the projection will decay to the equator as soon as this synchronization is lost due to dephasing. Additionally, a decay to the equator results when the second pulse comes after the system has decayed to its ground state by energy relaxation. The observed T_2 time is thus a combination of pure dephasing T_ϕ and T_1 expressed by their respective rates Γ [Ith+05]:

$$\Gamma_2 = \frac{\Gamma_1}{2} + \Gamma_\phi. \tag{2.60}$$

When the drive is detuned from ω_{01} by $\Delta\omega$, the phase difference between drive and state vector evolves, resulting in the characteristic Ramsey fringes [Ram50] of frequency $\Delta\omega$. Performing a T_2 measurement off-resonance thus precisely yields ω_{01} and prevents mistaking a small detuning for T_2 decay.

The physical processes leading to decoherence in superconducting quantum circuits are a matter of ongoing research. Prominent categories of noise are charge and magnetic flux noise, noise due to the radiation fields, and quasiparticles [Kra+19]. Defects and impurities in the circuit dielectric or in fabrication residues might couple to the circuit's fields via their dipole moment. This contributes to bulk dielectric (or ohmic) loss [Mar+05] providing channels for loss of the radiation energy and thus adds to Γ_1. Additionally, decreased lifetimes are observed at certain frequencies. This can be interpreted as individual two-level systems (TLS) oscillating at these frequencies, which are surely also present in non-tunable circuits. If such a TLS in turn couples to a bath of fluctuators (TLF) at lower, thermally populated energies, the resulting dispersive shifts affect ω_{01} and thus lead to dephasing [Sch+19; Bil19]. Observation of the qubit's performance in dependence of different external parameters like strain and electric fields enabled direct TLS spectroscopy [Gra+12] even distinguishing their locations in the circuit [Bil+20] (for a review of TLS loss see [MCL19]). In circuits with a small capacitance (e.g. a single junction, Sec. 2.1.2), charge fluctuations also directly influence ω_{01} via N_g (Eq. (2.25)).

Except for the detuned readout resonator required for readout and control as described in section 2.3.1), the microwave environment is engineered not to feature any radiation modes in the relevant frequency band to prevent the qubit from immediately decaying by emitting a photon of frequency ω_{01}. Enhancement of

spontaneous emission by coupling the emitter to a single mode was first described by Edward M. Purcell [Pur46]. It yields a rate

$$\Gamma_P = \left(\frac{g}{\Delta}\right)^2 \kappa,$$ (2.61)

where g denotes the coupling between the qubit and the mode, Δ their frequency detuning and κ the mode's linewidth [Hou+08]. This can be used in designing the readout mode to allow a clear enough signal without itself limiting the circuit lifetime. Photons of different frequencies can however still be present. For instance, high frequency thermal photons from warmer stages in the cryostat might directly drive the qubit transition or dispersively shift it. To limit this effect, attenuation and thermalization of the microwave setup is of great importance (Sec. 3.3) [Kri+19]. In addition, optimized circuit designs featuring high impedances and small dipole moments can help reduce coupling to parasitic modes [Kja+20].

In general, the variety of noise contributions has lead to refined circuit designs made to be less sensitive to these perturbations. The dimensions of a circuit define the strength of electromagnetic fields and thus the possible coupling to TLS. Bulk dielectric loss is addressed by the choice of low-loss materials for the metallization as well as the substrate and cleaning procedures during fabrication [Pla+20]. Excess quasiparticles excited even at low temperatures pose another limitation, which is tackled by introducing traps consisting of a lower-gap superconductor down-converting the energy of scattering phonons. [Kar+19; Hen+19]

2.3.4 Microwave circuits

Conducting experiments that make use of the introduced methods require their physical realization. Before the circuit designs will be introduced in section 3.1, we want to lay out their technical groundwork. Between the lower bound given by the thermal energy of the cryogenic environment and the upper one given by the superconducting gap, the microwave frequency band offers the necessary interface to our quantum circuits. The research field greatly benefits from readily available equipment for microwave signal generation, manipulation, transmission, and analysis. In many cases, the used tools have their origins in applications like telecommunication or radar working in the same frequency band. The terminology used in microwave based quantum experiments therefore shares the same origin.

A widespread method of describing a signal's interaction with a given circuit featuring n ports is the scattering matrix S_{ij}. It represents the transformation of the input voltages at port i to the one observed at the output port j as the signal is scattered by the circuit elements [Poz12]. In case of reflection i equals j. As

in this project we deal with two-port circuits, we can limit this treatment to the two-dimensional case:

$$\begin{pmatrix} U_{1,\text{out}} \\ U_{2,\text{out}} \end{pmatrix} = \begin{pmatrix} S_{11} & S_{12} \\ S_{21} & S_{22} \end{pmatrix} \begin{pmatrix} U_{1,\text{in}} \\ U_{2,\text{in}} \end{pmatrix}. \tag{2.62}$$

Importantly, all involved quantities are complex, carrying information not only about the wave's amplitude but also its phase. Assumed we have a setup to record these matrix elements (Sec. 3.3), understanding how a circuit element gives rise to its S matrix allows us to measure its properties directly.

To apply the method of dispersive readout and control introduced in section 2.3.1, we rely on microwave resonators. By coupling the resonator capacitively to a continuous transmission line, several of these notch-type resonators can be measured through the same ports. To observe even small shifts of their frequency ω_r, a small linewidth κ is required. This in turn depends on the rate at which energy stored in the oscillation is lost. A measure for this is the quality factor [Poz12]

$$Q = \omega_r \frac{E_{\text{stored}}}{P_{\text{loss}}} = \frac{\omega_r}{\kappa}. \tag{2.63}$$

Losses can be divided in those that are due to intrinsic losses by dissipation of the energy to a bath, which is not observable, for instance in the presence of a finite resistance or radiative losses, and those due to the coupling to the "bath" of the feedline. The first category is included in the internal quality factor Q_i and the second in Q_c. Combined they give the total, so-called loaded, quality factor

$$Q_l = \frac{1}{Q_i^{-1} + Q_c^{-1}}. \tag{2.64}$$

Ideally, Q_i would be infinite so as not to lose photons carrying information about the state of a coupled quantum circuit. Factors $> 10^5$ are facilitated by the use of superconducting materials and a mode environment, given by the sample box (Sec. 3.3.3), designed to reduce radiative losses. An infinite Q_c, on the other hand, would result in no measurement signal at all. Therefore, circuits are designed to be "overcoupled" with $Q_i \gg Q_c$.

The circuit impedances govern their response to a signal wave. By deriving the interplay with the quality factors, we can find the S matrix of an LCR circuit [PA98; Gao08]. Starting from the input impedance of a series LCR resonator with frequency $\omega_0 = 1/\sqrt{LC}$ [Poz12]

$$Z_{\text{in}} = R + i\omega L - \frac{i}{\omega C}, \tag{2.65}$$

where the dissipation is considered by the resistance R, the internal quality factor is found through the condition for resonance. Requiring the energy to be equal in the capacitor and inductor, it follows that

$$Q_i = \frac{1}{\omega_0 R C} = \frac{\omega_0 L}{R}. \tag{2.66}$$

For small detunings $\Delta\omega = \omega - \omega_0$, equation (2.65) can then be rewritten as

$$Z_{in} = R + 2i\frac{R Q_i \Delta\omega}{\omega_0}. \tag{2.67}$$

A typical realization of microwave resonators in the GHz band are transmission lines with geometrically imposed boundary conditions. In the case of an open termination after length l, the fundamental mode existing is defined by the condition for its wavelength $l = \lambda/2$. The impedance of such a line is [Poz12]

$$Z_{line} = \frac{Z_0}{\tanh \gamma l}. \tag{2.68}$$

Here, Z_0 is the characteristic line impedance in the absence of boundary conditions and γ represents a complex, geometry and frequency dependent wave propagation parameter, which becomes purely imaginary in the case of lossless transmission. For a resonator that is capacitively coupled to the rest of the circuit (Fig. 2.7 a)), the impedance of the coupling capacitance C is added

$$Z_{res} = Z_{line} + \frac{1}{i\omega C}. \tag{2.69}$$

Due to the tanh in equation (2.68), the resonance condition leads to a transcendental equation, which can however be evaluated by Taylor expansion around ω_r. For a small coupling capacitance this yields [Poz12]

$$Z_{res} \approx \frac{\pi}{2 Q_i Z_0 C^2 \omega_r^2} + i\frac{\pi\Delta\omega}{Z_0 C^2 \omega_r^3}. \tag{2.70}$$

Identifying $R = \pi/(2 Q_i Z_0 C^2 \omega_r^2)$ and comparison to equation (2.67) confirms the equivalence to a series LCR circuit.

Since we are interested in the effect of such a resonator on the signal traveling through the feedline it is coupled to, we consider the impedance at the coupling capacitor in the opposite direction, replacing Z_{line} in equation (2.69) by the external load from the feedline $Z_L = 2Z_0'$. The factor 2 arises due to the notch-type configuration seeing loads of the characteristic impedance of the feedline Z_0' in both
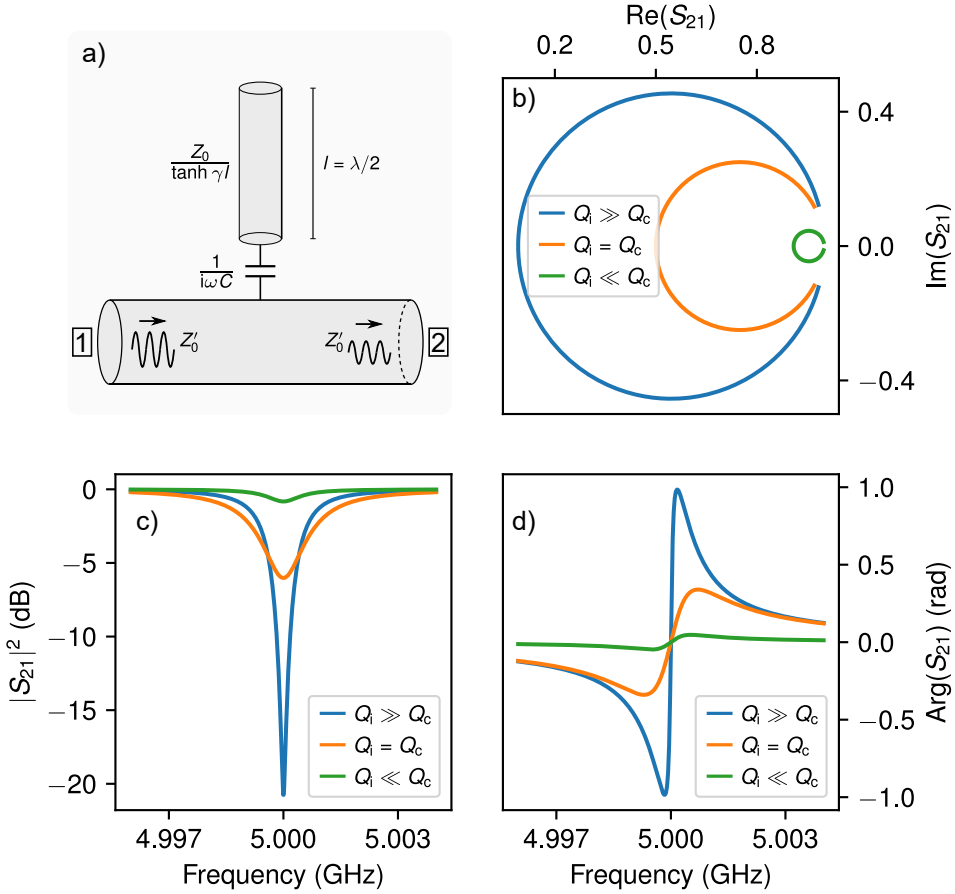
Figure 2.7: Notch type resonator and its effect on a wave transmitted through the feedline. (a) A terminated transmission line of length $\lambda/2$ capacitively coupled to a feedline acts like a series LCR resonator. **(b)** The resulting S_{21} scattering parameter for a signal entering the feedline at port 1 and traveling through to port 2 yields a circle in the complex plane from which the resonators Q factors can be extracted. **(c)** The amplitude signal squared corresponds to the typical resonance dip around ω_r with Lorentzian shape. Depending on the ratios of Q_i and Q_c the shape changes with the maximum depth in the case of an overcoupled resonator $Q_i \gg Q_c$. **(d)** The argument of S_{21} gives the phase roll-off, which maximally ranges from $-\pi/2$ to $\pi/2$ if $Q_i = \infty$.

directions. As before, we can introduce the corresponding Q factor representing the power dissipated into this load in the case of a small capacitance [Bra18]

$$Q_c \approx \frac{\pi}{Z_0 Z_0' \omega^2 C}. \tag{2.71}$$

With this, equation (2.70) can be rewritten as

$$Z_{res} = Z_0' \left(\frac{Q_c}{2Q_i} + i\frac{Q_c \Delta\omega}{\omega_r} \right). \tag{2.72}$$

Finally, this leads to the complex scattering parameter for a signal traveling from port 1 to port 2 through a transmission line with a capacitively coupled notch-type resonator [Bra18]

$$S_{21} = \frac{U_{2,out}}{U_{1,in}} = \frac{2Z_{res}}{2Z_{res} + Z_0'} = 1 - \frac{Q_l}{Q_c(1 + 2iQ_l\Delta\omega/\omega_r)}. \tag{2.73}$$

This equation represents a circle in the complex plane. A fit to this circle provides a convenient method to obtain the resonator's Q factors [PA98; Pro+15]. In figure 2.7 b) the circles resulting for different coupling regimes are plotted. Looking at the amplitude or phase of the signal (Fig. 2.7 c) and d)) illustrates how overcoupled resonators ($Q_i \gg Q_c$) are best suited for the observations of small frequency shifts: the signal resulting from the observation of a single point in a dip or along a phase roll-off that shifts is larger the deeper the dip and the larger the roll-off.

2.4 Modeling driven systems

In physical systems exhibiting multiple levels and small anharmonicity, these can be excited by multi-photon transitions of frequency close to the fundamental transition ω_{01}. Such a system is not well described by the assumption of a two-level system coupled to a single mode. Including multi-photon excitations, stimulated emission, decay and dephasing, this makes for a highly dynamic system that can not be solved analytically. There are, however, ways to numerically simulate these dynamics.

The Gorini–Kossakowski–Sudarshan–Lindblad master equation [Lin76; GKS76] describes the time evolution of the density matrix that was introduced in equation (2.58)

$$\dot{\rho} = -i/\hbar[\mathcal{H}, \rho] + \sum_{j=1}^{N} \Gamma_j \left(L_j \rho L_j^\dagger - 1/2\{L_j^\dagger L_j, \rho\} \right) \tag{2.74}$$

by considering the effects of operators L_j acting on the system described by the Hamiltonian $\mathcal{H}$ with rates Γ_j. The effects described by the operators L_j are typically due to interaction of the closed system with its environment. If the sum is zero and the net effect of all L_j on the system combined vanishes, the equation reduces to the von Neumann equation, which describes the time evolution of the closed system. The curly brackets denote the anticommutator $\{a, b\} = ab + ba$. [GZ04]

The dynamics of a two-level system coupled to a drive mode are typically studied in the rotating frame corresponding to the excitation frequency of the system ω_{01} resulting in a time-independent Hamiltonian [Bra18]. This method does, however, not work for systems with higher levels that can be excited by multi-photon transitions at frequencies close to yet different from ω_{01}. Since the system exhibits a strong periodicity, it is suited for the application of Floquet theory [Shi65]. To apply this approach to the Lindblad equation of a driven multi-level system for different drive frequencies and lengths, it is expanded into a superoperator form, which is evaluated for the frequencies of interest by summing over the Floquet components until the time of interest, following a method introduced for calculations of dynamics in magic-angle spinning NMR [BD01]. The result for different frequencies and times of interest yield a two dimensional representation of the driven system's dynamics. A challenge arising are the dimensions of the matrices encountered in the calculation. Considering only 3 states and 5 photons already results in a superoperator of shape 45×45 that has to be diagonalized for each frequency. We therefore started with fewer levels and photons and increased both until the results did no longer change noticeably.

First, the superoperators are constructed from the Lindblad equation as the matrix

$$\mathbf{P}_0 = (\mathcal{H}_0 \otimes \mathbb{1}) - (\mathbb{1} \otimes \mathcal{H}_0^\mathsf{T}) + \Gamma_i \mathrm{i} \left((L_i \otimes L_i^*) - \left((L_i^\dagger L_i \otimes \mathbb{1}) + (\mathbb{1} \otimes (L_i^\dagger L_i)^\mathsf{T}) \right) / 2 \right) \tag{2.75}$$

$$\mathbf{P}_\mathrm{d} = (\mathcal{H}_\mathrm{d} \otimes \mathbb{1}) - (\mathbb{1} \otimes \mathcal{H}_\mathrm{d}^\mathsf{T}), \tag{2.76}$$

where $\mathbf{P}_0$ describes the multilevel system subjected to the operators L_i later representing decay ($L_1 = a$) and dephasing ($L_2 = a^\dagger a$), and $\mathbf{P}_\mathrm{d}$ the external drive. $\mathbb{1}$ is an identity matrix with dimensions $(N \times N)$ where N is the number of levels considered.

To describe a multilevel system in a general form, we model the undriven Hamiltonian as

$$\mathcal{H}_0 = \left(\hbar \omega_{01} + \hbar \omega_\mathrm{s} \sqrt{\epsilon^2 / (\epsilon^2 + \Delta^2)} \right) \hat{n} - \hbar \omega_\mathrm{an} (\hat{n}^2 - \hat{n}), \tag{2.77}$$

with $\hat{n}$ denoting the bosonic number operator. This can be interpreted as anharmonic oscillator with frequency ω_{01} and anharmonicity ω_an. An additional term

allows for small shifts of the oscillator frequency by ω_s in a region around the main transition ω_{01} of width ϵ and reduced by the detuning $\Delta = \omega_{\text{drive}} - \omega_{01}$ of the drive. Such a shift can be induced for instance by the AC stark effect [Sch+18]. For the drive we define

$$\mathcal{H}_d = \hbar A(a + a^\dagger), \tag{2.78}$$

with the creation and annihilation operators defined in the basis of $\mathcal{H}_0$ and an amplitude factor A. The drive frequency is later set in the Floquet matrix for each value to be calculated.

With the superoperators defined, this Floquet matrix is constructed for each drive frequency as

$$\mathbf{P}_F = (\mathbb{1}_{N_\gamma} \otimes \mathbf{P}_0) + \hbar\omega(\mathbf{S}_\gamma \otimes \mathbb{1}_P) + (\mathbf{T} \otimes \mathbf{P}_d), \tag{2.79}$$

again with the identity matrices of fitting dimensions and the Toeplitz matrix $\mathbf{T}$ with ones on the first and minus first off-diagonals. $\mathbf{S}_\gamma$ in the second term represents the photon matrix defined by a vector denoting the rising photon number on the diagonal:

$$\mathbf{S}_\gamma = \text{diag}(-N_\gamma/2, \ -N_\gamma/2 + 1, \ \dots, \ 0, \ \dots N_\gamma/2). \tag{2.80}$$

Diagonalization of $\mathbf{P}_F$ yields the eigenvalues λ_i and eigenvectors $\mathbf{v}_i$ arranged in a matrix $\mathbf{V}$, which then define the time evolution of the system

$$U_F(t) = \mathbf{V} \cdot \text{diag}\left(e^{it\cdot\text{diag}(\lambda_i)}\right) \cdot \mathbf{V}^{-1} \tag{2.81}$$

where $U_F(0)$ is defined as the identity matrix on the zero photon manifold and zero on all others. Summing up these time evolution steps then yields the total time evolution. Multiplication with the initial density matrix ρ_0 (usually all zero except for the ground state) and calculating the trace of the result then yields the occupation probabilities $p_{|j\rangle}$ of the j-th level at time t when driven with frequency ω:

$$p_{|j\rangle}(t, \omega) = \text{Tr}\left(|j\rangle\langle j|\left(\sum_{n=-N_\gamma/2}^{N_\gamma/2} U_F(t)e^{in\omega t}\right) \cdot \rho_0\right), \tag{2.82}$$

which sums over the contributions from each of the Floquet manifolds. This is evaluated for all time and frequency points recorded in the measurement and multiplied with an additional factor of $\sqrt{N}$ to account for a reduced dispersive shift of the N-th level. A rendering as two-dimensional image with the calculated values color coded can then be compared to measurement. [Sch+20]

3 From metal to experiment

For material properties to manifest themselves in measurable quantities, two main requirements must be met. Since we are interested in dynamics arising from the nanoscale material structure, the scales have to be sufficiently reduced for them to emerge. Secondly, a suitable circuit is required to conduct the experiments.

3.1 Design

Superconducting quantum circuits are a matter of experimental research since more than twenty years [NPT99; BGO20]. Over time, the circuit designs have evolved and more complicated layouts aim at improving their performance and exploring new quantum effects and applications. This has been facilitated by progress in fabrication technologies and understanding of the circuit elements and their underlying physics. Implementing a new type of nonlinear element impacts the circuit's basic behavior. For experiments that focus on the physics inherent to this element and the material it is made of, the circuit environment is a tool with the main purpose of making these physics accessible. It is therefore of benefit to reduce the design complexity to limit additional effects and to profit from established methods thus allowing for a more direct study of our nanowire's intrinsic dynamics.

While DC transport measurements make the nanowire's superconducting properties directly accessible, important dynamical properties determining a circuit's energy spectrum and loss mechanisms can only be studied in a design allowing the free time evolution of excitations.

3.1.1 The (an)harmonic oscillator

The realization of an oscillating electrical circuit does not require many components. Already a capacitor shunted by an inductor will oscillate as soon as it is once charged. Its discharge current aiming at balancing the charge difference Q will

induce an inductive response. In the absence of dissipation, such an oscillation will continue forever. These dynamics are captured by a simple Hamiltonian governed by the two energies $E_C = e^2/2C$ and $E_L = \Phi^2/2L$:

$$\mathcal{H}_{LC} = \frac{e^2}{2C}\hat{N}^2 + \frac{\hat{\Phi}^2}{2L} \tag{3.1}$$

with $\hat{N}$ denoting the number operator of charges on the capacitor. In analogy to the quantum harmonic oscillator, the above Hamiltonian can be written in terms of the bosonic creation and annihilation operators as

$$\mathcal{H}_{LC} = \hbar\omega \left(a^\dagger a + \frac{1}{2} \right) \tag{3.2}$$

with a ground state energy of $\hbar\omega/2 = \hbar/2\sqrt{LC}$. The parabolic potential gives rise to evenly spaced energy levels with separation $\hbar\omega$.

The situation changes, however, when the inductor is replaced by a nonlinear element as found in a Josephson junction. In this case, the Hamiltonian combining the charging energy of the capacitor and the Josephson coupling energy E_J takes the same form as for an isolated junction introduced in section 2.1.2 (Eq. (2.25)) [SSH97; Bou+98]

$$\mathcal{H}_T = 4E_C \left(\hat{N} - N_g \right)^2 - E_J \cos(\hat{\varphi}) \tag{3.3}$$

with the difference that the charging energy is now defined by the total circuit capacitance. The sinusoidal current-phase relation of the junction gives rise to the cosine potential, which in turn induces anharmonicity into the level spectrum ($E_{12} - E_{01} = h\alpha \neq 0$). Figure 3.1 a) illustrates how the charging energy parabolas are broken into bands by the Josephson coupling as described in section 2.1.2.

In contrast to an isolated junction, the capacitance can now be varied independently of the junction properties by the circuit design and much larger capacitances are possible, decreasing E_C. Increasing the ratio E_J/E_C reduces the impact of the offset charge N_g, effectively flattening the bands (Fig. 3.1 b) & c)). This was introduced as a method to limit the effect of charge noise [Koc+07]. Circuits with $E_J/E_C \gtrsim 100$ are typically referred to as Transmon qubits [BGO20] and N_g is dropped. Their simplicity and good performance lead to wide use in many experiments, eventually including the demonstration of quantum supremacy in superconducting circuits [Aru+19].

A series expansion of the cosine term in equation (3.3) illustrates the resemblance of the Transmon to an anharmonic oscillator.

$$\mathcal{H}_T \approx 4E_C\hat{N}^2 - E_J + \frac{E_J}{2}\hat{\varphi}^2 - \frac{E_J}{4!}\hat{\varphi}^4 + \mathcal{O}(\hat{\varphi}^6) \tag{3.4}$$
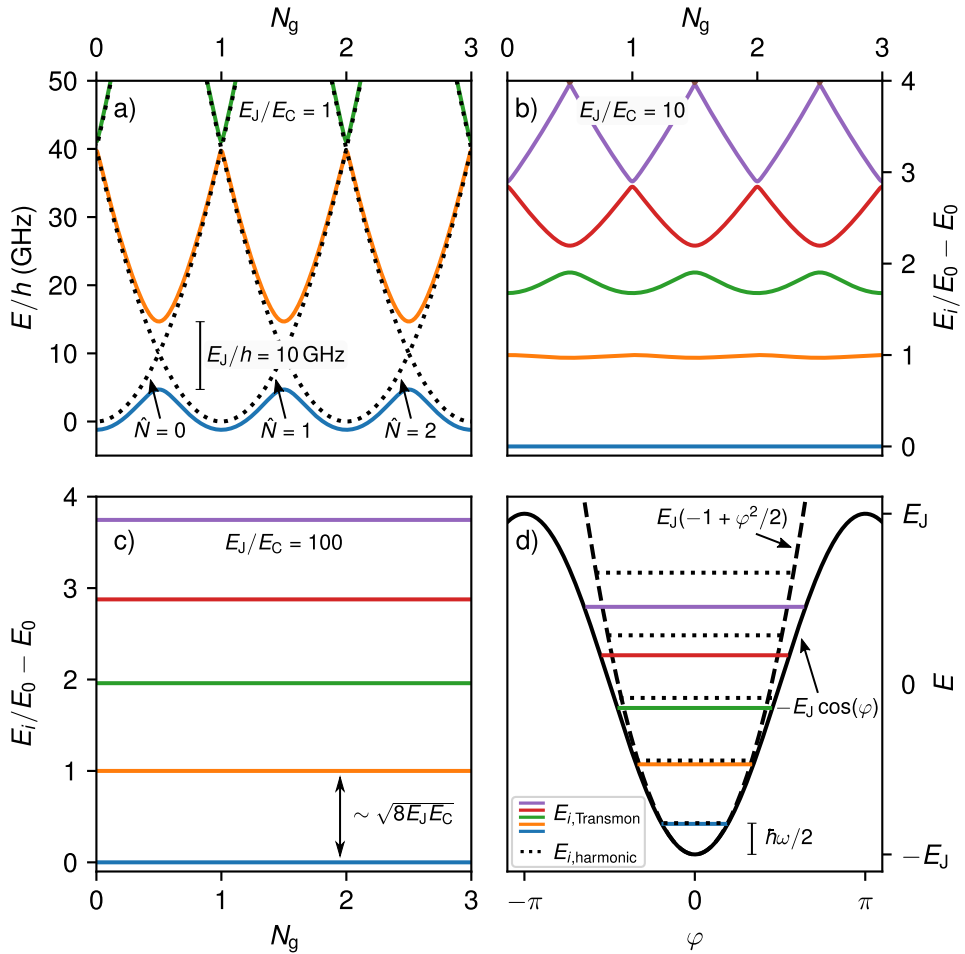
Figure 3.1: Energy bands of charge qubit and Transmon (a) The Josephson coupling term in Eq. (3.3) connects charging energy parabola defined by the first term of different charge numbers (dashed) into bands. **(b) & (c)** Increasing the circuit capacitance reduces the effect of offset charges N_g and thus also of charge noise while also reducing the anharmonicity. **(d)** Potentials and eigenenergies of the Transmon in comparison to the harmonic oscillator.

is equivalent to the harmonic case in equation (3.1) up to second order in $\hat{\varphi}$. Figure 3.1 d) illustrates the similarities, plotting together the Transmon eigenenergies and cosine potential with the evenly spaced levels resulting when orders greater than 2 are ignored. For the shown eigenenergies, the Hamiltonians were diagonalized numerically with the help of the Python framework QuTip [JNN12]. For large $E_J/E_C \to \infty$, perturbation theory yields the eigenenergies of the Transmon up to fourth order as [Koc+07]

$$E_i \approx -E_J + \sqrt{8 E_C E_J} \left(i + \frac{1}{2} \right) - \frac{E_C}{2} \left(i^2 + i \right) + \frac{E_C}{4} \tag{3.5}$$

and with this the lowest transition frequency ω_{01} and anharmonicity α:

$$\hbar\omega_{01} = E_{01} = E_1 - E_0 \sim \sqrt{8 E_C E_J} - E_C = \frac{\hbar}{\sqrt{L_J C}} - E_C \tag{3.6}$$

$$h\alpha = E_{12} - E_{01} \sim -E_C, \tag{3.7}$$

where $L_J = \hbar/2e I_c$ is the Josephson inductance.

3.1.2 Nanowires as nonlinear element

Introducing granular aluminum nanowires as nonlinear element leads to important consequences for the whole circuit. First, as discussed in section 2.1.5, it can no longer be regarded as zero-dimensional tunnel contact. Its response is not only governed by its critical current, but also by its geometry and material properties. At the same time, measuring the resulting circuit's response and the differences to what would be expected from a circuit with a Josephson tunnel contact yields insight into how these properties manifest.

Consisting of a material with intrinsic granular structure (Sec. 2.2.1) and with a geometrically constrained current path, the nanowire's behavior can be expected to range between that of a single boundary to the averaged out limit (Sec. 2.2.2). With an increased number of barriers, the total inductance increases, reducing the current and phase gradient over one barrier. As illustrated in figure 3.1, the difference between parabolic potential and the sinusoidal junction potential decreases for smaller values of φ and with it the nonlinearity of the element. Comparable to the discussion for homogeneous weak-links, the current-phase relation of the nanowire might therefore continuously approach the linear limit when its length increases.

Additionally, while the geometric circuit inductance is typically negligible with respect to the Josephson inductance of a single tunnel contact, this is not the case in circuits consisting of a material contributing a large kinetic inductance. In this case,

the circuit Hamiltonian needs to be extended by the additional inductive energy contribution. The challenge for a quantitative description lies in the uncertainty of how the total phase is split between the circuit elements and in the case of a nanowire also which parts of it need to be considered. To illustrate the effect of additional linear inductance in a circuit, we can use a model introduced for a Josephson junction Transmon circuit in a concentric geometry, in which a small contribution of geometric inductance needs to be considered [Bra+16; Bra18].

A method allowing for the derivation of a given circuit's Hamiltonian is found in circuit quantization [Dev97]. Assuming three circuit components of capacitance C, non-linear Josephson inductance with critical current I_c, and a linear inductance L in series, relations for the superconducting phase in the circuit are found [Bra18]:

$$\frac{\hbar}{2e} C \ddot{\varphi}_1 = I_c \sin(\varphi_2) = \frac{\hbar}{2e} \frac{1}{L} \varphi_3 \quad \text{and} \tag{3.8}$$

$$\varphi_1 + \varphi_2 + \varphi_3 = 0 \quad \Rightarrow \tag{3.9}$$

$$\varphi_3 + \arcsin(a\varphi_3) = -\varphi_1 \tag{3.10}$$

with $a = E_L/3E_J$ and the inductive energy $E_L = (\Phi_0/2\pi)^2/2L$. The φ_i relates to the voltage dropping over the three circuit elements. In the limit that $a \gg 1$ or φ_1 small this can be solved, leading to the equation of motion with $\varphi_1 \equiv \varphi$

$$\frac{\hbar}{2e} C \ddot{\varphi} + \frac{\hbar}{2eL} \frac{1}{(1+a)^2} \varphi + \frac{\hbar}{2eL} \frac{a}{(1+a)^2} \sin \varphi = 0. \tag{3.11}$$

The resulting Hamiltonian can be expressed in a form similar to equation (3.3) [Bra18]:

$$\mathcal{H}_{TL} = 4E_C \hat{N}^2 - \hat{E}_J \cos \varphi + \hat{E}_L \varphi^2 \tag{3.12}$$

by introducing the effective energies

$$\hat{E}_J = \frac{6E_L^2}{(6E_J + 2E_L)^2} E_J \quad \text{and} \quad \hat{E}_L = \frac{9E_J^2}{(6E_J + 2E_L)^2}. \tag{3.13}$$

The term $\hat{E}_L \varphi^2$ in equation (3.12) increases the parabolic contribution to the potential, reducing the anharmonicity to be expected. For $L \to 0$, $E_L \to \infty$ and therefore $\hat{E}_L \to 0$ leading back to the behavior of the Transmon.

While equation (3.12) was derived explicitly for circuits with a Josephson junction and sinusoidal current-phase relation and is valid only for a small inductance, comparison to the observed behavior in nanowire circuits can lead to insights into the parameter regime they operate in. As the non-sinusoidal current-phase relation of the nanowire and the additional inductance both lead to the system approaching the harmonic behavior, it can provide a useful approximation to treat the part of
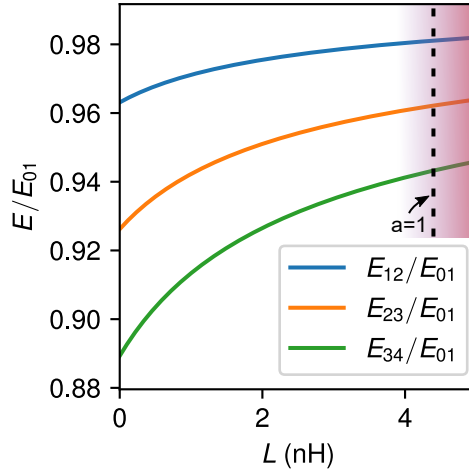
Figure 3.2: Relative anharmonicity in the presence of additional inductance. The transitions between four eigenenergies of the Hamiltonian (3.12) are plotted relative to the fundamental transition in dependence of added inductance L. The other parameters chosen here are $I_c = 50\,\text{nA}$ and $C = 77\,\text{fF}$. At $4\,\text{nH}$ additional inductance, the fundamental transition is at $E_{01}/h \sim 3.7\,\text{GHz}$ and $\alpha = (E_{12} - E_{01})/h \sim -70\,\text{MHz}$. $4\,\text{nH}$ corresponds to about $5.5\,\text{k}\Omega$ resistance of larger granular aluminum structures (Eq. (2.38)). The approximations are valid for small values of $a = E_L/3E_J$. The black dashed line marks $a = 1$.

the wire dominated by its critical current as an effective junction, with the rest combined in the linear inductance part.

This also allows us to conclude that, under the preceding assumptions, a maximal anharmonicity is to be expected for short nanowires with small critical current and minimum additional inductance. However, additional considerations come into play during the practical realization of a device. We will see that when additional inductance from surrounding circuit parts can not be completely prevented, longer wires from a less resistive material can have the advantage of increasing the relative inductance contribution of circuit parts of higher current density. To achieve small critical currents in short wires requires highly resistive metal films, imposing their own challenge and resulting in large inductances even from larger structures.

Anharmonicity is a prerequisite for the application of a circuit for quantum information applications. The control over a system's state depends on the ability to drive individual transitions. On the other hand, from the perspective of fundamental research it provides us with a valuable measure for how the disorder, intrinsic to our nanowires, manifests in the emerging circuit dynamics.

3.1.3 Nanowire oscillator designs

Two different designs have been realized in this PhD thesis. The first one is a compact, single-layer paddle capacitor shunted by a nanowire. This design represents the realization of an anharmonic oscillator from a single material layer gaining its anharmonicity from the granular aluminum nanowire with the goal of making individual quantum transitions accessible.

The paddle design (Fig. 3.3) has already found application in Transmon Josephson junction qubits [San+13]. It allows for the realization of relatively large capacitances without the use of interdigitated plates. Larger gaps, which reduce the local electric fields that couple to TLS or induce bulk dielectric loss, have been beneficial for the performance [Cho+12]. At the same time, an overall reduce in edge length and surface area can be beneficial in reducing the total number of TLS present in the circuit [Bil+20]. The so-called microstrip geometry places the ground plane on the bottom of the substrate separate from the rest of the circuit on the top side. This focuses the electric fields into the low-loss [Kru+99] sapphire substrate and is especially advantageous in the presence of organic residues on the surface. Additionally, the absence of a ground metallization between the circuit parts helps prevent slotline modes [PPT05], crosstalk via parasitic modes, and the local trapping of magnetic flux [Chi+16]. Also, changes in the placement of parts made in one lithography step does not immediately require a new mask for structures added in later steps. On the other hand, special care has to be taken after application of the ground plane so as not to scratch it and to ensure good electrical contact to the ground reference of the cryostat.

In a circuit made entirely from a high kinetic inductance material, additional factors need to be considered. All circuit parts in the current path between the plates with alternating charge contribute to the total inductance. Contributions to the desired nonlinearity, however, mainly arise in parts with small I_c and thus higher ratio I/I_c. It is thus important to reduce the "linear" inductance from parts outside the wire by reducing their number of squares. This gives another argument against the use of an interdigitated design in which each finger contributes several squares. On the other hand, it also limits the distance between the paddles.

As a trade-off, we chose a distance of $10\,\mu m$ and use successive constrictions to reduce the dimensions by several orders of magnitude from the width of the paddles toward the nanowire. The design is depicted in figure 3.3 a). The first step are two $((5-x)\times 5)\,\mu m^2$ squares from both sides, where x is adjusted to make room for the different nanowire lengths. While wider structures would contribute less squares, their opposing faces are separated by only $\sim 1\,\mu m$ creating a region of high fields, which we want to limit. From there, $400\,nm$ wide rectangles lead to

triangles of 400 nm width and 200 nm altitude. These triangles help to reduce the electron beam dose in close vicinity of the nanowire during lithography (Sec. 3.2.2) that otherwise limits the resolution.

The capacitance of the coplanar paddles was simulated and calculated in an analytical approximation for validation. For the capacitance between two parallel strip lines Gevorgian and Berg provide a closed form expression based on conformal mapping [GB01]. For two planar stripes of width w, length l, and distance d on a substrate with dielectric constant ϵ and thickness h it becomes:

$$C = \epsilon_0 \epsilon_{\text{eff}} \frac{K\left(\sqrt{1-k^2}\right)}{2K(k)} l \tag{3.14}$$

in which K are complete elliptic integrals,

$$k = \frac{\tanh\left(\frac{\pi d}{4h}\right)}{\tanh\left(\frac{\pi(w+d/2)}{2h}\right)} \tag{3.15}$$

the result of the transformation for the elliptic integral considering the given geometry, and $\epsilon_{\text{eff}} = 1 + (\epsilon - 1)q$ the effective dielectric constant in which

$$q = \frac{K\left(\sqrt{1-k^2}\right)}{2K(k)} \frac{K\left(\frac{d/2}{w+d/2}\right)}{K\left(\sqrt{1-\frac{d^2}{4(w+d/2)^2}}\right)} \tag{3.16}$$

denotes a filling factor. For our design with parameters

$$w = 60 \, \mu\text{m}, \, l = 160 \, \mu\text{m}, \text{ and } d = 10 \, \mu\text{m} \tag{3.17}$$

on a substrate of $h = 350 \, \mu\text{m}$ thickness and with a dielectric constant of $\epsilon = 10$, this yields a capacitance of $C_{\text{calc.}} = 20.8 \, \text{fF}$ in good agreement with the value from simulation of $C_{\text{sim.}} = 21.2 \, \text{fF}$ (Fig. 3.4 a)).

For the latter, the paddle capacitor geometry was simulated with the finite element simulation suite *Sonnet*[1]. The nanowire was modeled by a varied lumped element inductance L_{v}. When the nanowire oscillator crosses the frequency of the $\lambda/2$ readout resonator (detailed at the end of the section) the two modes hybridize, resulting in a distinct anticrossing of the resonance dip observed in the transmission through the feedline. This anticrossing can be fitted to the eigenvalues of the matrix describing this two mode system in the Jaynes-Cummings form (Eq. (2.46)):

$$\mathcal{H}_{\text{JC}} = \begin{pmatrix} \hbar\omega_{\text{r}} & \hbar g \\ \hbar g & \hbar/\sqrt{L_{\text{v}}C} \end{pmatrix}. \tag{3.18}$$

---

[1] Sonnet Software, Inc., `https://www.sonnetsoftware.com/`
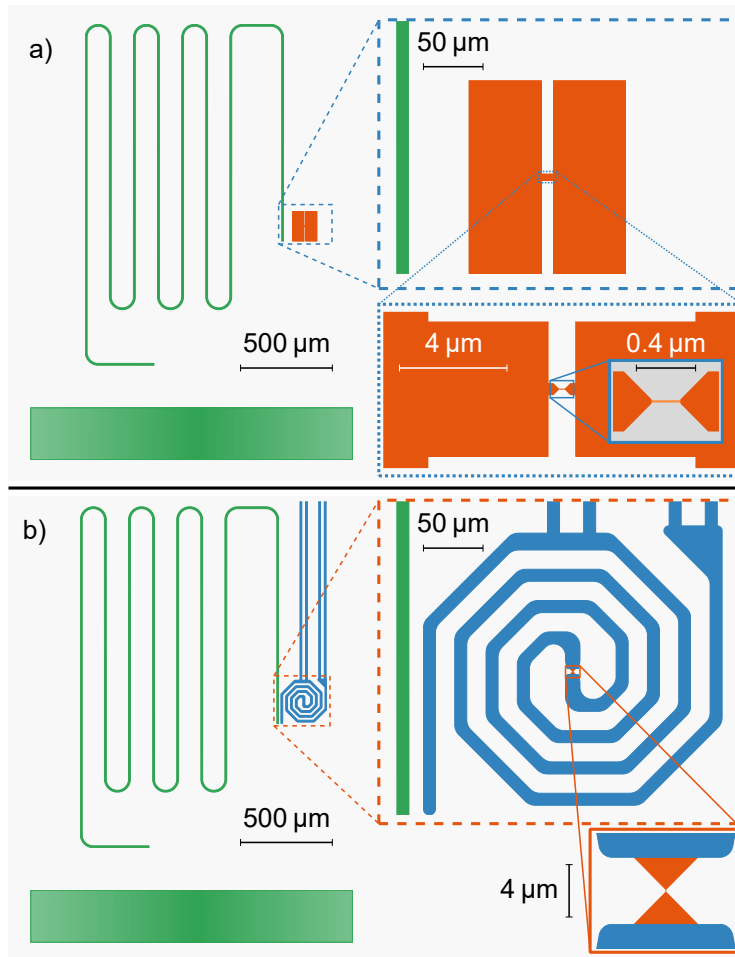
Figure 3.3: Circuit designs for this project. (a) Nanowire oscillator in a single-layer paddle design capacitively coupled to a $\lambda/2$ microstrip readout resonator and part of the microwave transmission line. The circuit elements for readout and control fabricated from aluminum are colored in green. Granular aluminum is colored in orange. Closeups depict the smaller circuit parts. The width of the nanowire shunting the paddles is not to scale since it is defined by the fabrication process (see Sec. 3.2.2). The stepwise constrictions leading to the wire are designed to limit the number of squares and electron beam dose. **(b)** Nanowire oscillator with spiral capacitor. The latter made from pure aluminum and connected to DC contact lines (blue, see also Fig. 3.5) shunts part of the kinetic inductance. The spiral design results in a compact circuit with increased capacitance to compensate for the reduced inductance. At the same time, the circuit's dipole moment is suppressed (manifesting in the smaller coupling distance to the resonator) reducing potential crosstalk between neighboring circuits.
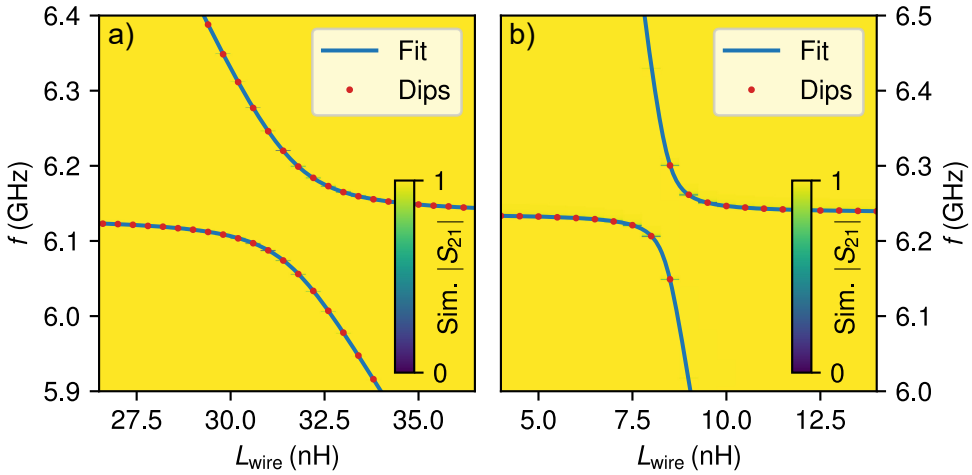
Figure 3.4: Simulation of circuit capacitance and coupling. The colormap represents the transmission amplitude through the feedline with the resonance dip of the $\lambda/2$ resonator. **(a)** Simulation of an oscillator in the paddle design (Fig. 3.3 a)) coupled to the $\lambda/2$ resonator. The nanowire is modeled as a lumped element inductance L_{wire} which is varied. The splitting of the resonance dip in the anticrossing yields their coupling $g/2\pi = 71\,\text{MHz}$ and the tails yield the capacitance $C = 21\,\text{fF}$. **(b)** The spiral capacitor (Fig. 3.3 b)) constitutes a 77 fF capacitance in a compact design with low dipole moment. The latter resulting in a coupling of 75 MHz at 1/5th of the spatial distance to the resonator.

A fit to the frequencies of the simulated dips in figure 3.4 then yields the capacitance C together with the coupling g between the two systems on resonance. The coupling was designed by varying the distance between the paddles and the readout resonator. For 50 µm distance, the simulation yields $g/2\pi = 71\,\text{MHz}$ facilitating clear dispersive shifts without Purcell limiting the oscillator lifetime.

For fits like this and all data analysis, data acquisition, as well as control of the measurement devices we strongly rely on our in-house developed open source software package *qkit* [qkit].

In a second design presented in figure 3.3 b) we put the focus on a reduced inductance from circuit elements outside the nanowire by shunting the parts constituting the capacitor with pure aluminum. Doing so also reduces the overall inductance and thus requires an increased capacitance, which finally reduces the frequency dependence on the sheet resistance of the granular aluminum film. At the same time we introduced DC contact lines to allow for four-point measurements of the resistance. These lines are to be removed later, before microwave measurements are conducted. Since our granular aluminum nanowires have been found to be adjustable in resistance by current pulses (Sec. 2.2.3), this DC contact not only gives

more insight into the circuit's parameters but also introduces the ability to control them.

While the use of pure aluminum, which does not contribute a large inductance for the capacitive circuit elements, eases some of the previous design limitations, the increased size of the resulting circuit imposes new challenges. With a limited available chip area, larger oscillators are bound to be closer to each other and possibly interact via their further reaching fields. This becomes especially important for experiments with circuits adjusted to very similar parameters, for instance to study the effect of the wire length isolated from other changes.

We therefore chose a double spiral design with two intertwined arms shunted in the middle by the nanowire. In the charged state the two arms have opposite charges alternating in all directions outgoing from the center. The dipole moment is thus suppressed. This manifests in a much smaller required distance to the readout resonator of only 10 μm to achieve a coupling comparable to the paddle design. The more complicated geometry impedes a calculation of the resulting capacitance. Following the validation of the simulated value for the paddle design, we apply the same method (Fig. 3.4 b)) yielding a capacitance of 77 fF in a two-turn spiral with 10 μm wide arms and 16 μm spacing. Together with rounded corners, the latter is intended to reduce local fields.

Contact between the two material layers is established via two $(8 \times 18)\,\mu m^2$ rectangles on both sides of the wire fully covered by aluminum. Leading to the wire are triangles of 8 μm width and 4 μm altitude. Their symmetry is intended to yield the same inductance independent of a potential misalignment of the 4 μm gap between the aluminum arms.

Four nanowire oscillators with individual readout resonators fit on each $(5 \times 5)\,mm^2$ chip featuring one microwave transmission line for contact to the measurement setup (Sec. 3.3). The paddle design without additional contact lines allows for fabricating nine such chips on one $(2 \times 2)\,cm^2$ wafer. The arrangement of the chips featuring DC contacts is shown in figure 3.5. Each of the lines leads to an individual bond pad, from where a wire bond can connect to the sample holder. After the DC experiments are performed on the full wafer, the contact lines are removed by etching and the wafer is diced into four microwave chips (darker gray squares in Fig. 3.5).

The length of the nanowire was varied between 50 and 400 nm in 50 nm steps and divided into two groups of four shorter and four longer wires. For both groups, the circuits featuring the shortest wires were paired with the readout resonators of highest frequency to limit the frequency detuning between them.
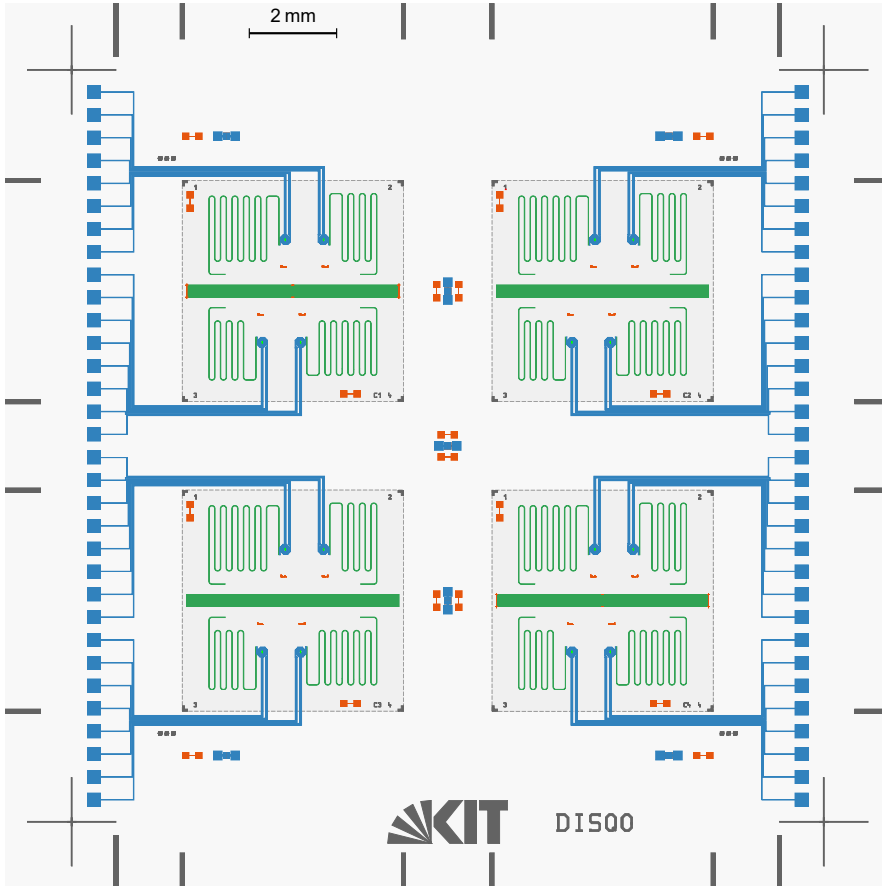
Figure 3.5: Layout of the 2 cm × 2 cm wafer design featuring DC contact lines. Each nanowire oscillator is contacted by four DC lines leading to bond pads at the wafer edge (blue) allowing for 4-point measurements of the circuit's resistance and critical current. These lines are later removed and the wafer diced to yield four individual (5×5) mm^2 chips (shaded in darker gray) for microwave measurements. Each of them features four $\lambda/2$ microstrip readout resonators ranged, between 5 and 7 GHz, capacitively coupled to a microwave transmission line (green). Test structures exist for the granular aluminum (red) sheet resistance and inter-layer contact resistance.

For readout and manipulation, four different aluminum $\lambda/2$ resonators (Sec. 2.3.4) were designed. A relatively wide spacing of about 800 MHz between each other was chosen for these experiments with nanowire oscillators since the latter might vary in frequency between different experiments due to varying film and nanowire resistances. From simulation of the chip with only the readout resonators on a 350 μm thick sapphire substrate we obtained their frequencies of 4.53, 5.32, 6.10, and 6.89 GHz agreeing well with the values later measured of 4.52, 5.27, 6.10, and 6.85 GHz. Small deviations can occur due to substrate thickness variations, anisotropy of its dielectric constant, inhomogeneities or scratches in the ground plane on the bottom side of the chip, or meshing effects in the finite element simulation of the rounded resonators.

3.2 Fabrication

Fabrication of nanostructures is challenging. In the context of this project, nanoscopic scales arise both at the material as well as the circuit level. The intrinsic granular structure of the oxidized aluminum (Sec. 2.2) and the amount and thickness of the insulating barriers determine the accessible parameter range of resistances, inductances, and consequently anharmonicities in the circuit. Additionally, structuring the material to nanometer scales is required to define a low dimensional current path strongly affected by the material composition. All structuring steps of our fabrication were conducted in the cleanroom of the Center for Functional Nanostructures (CFN) at the KIT.

3.2.1 Sputter deposition and control

Our granular aluminum films are grown in an in-house made sputter deposition tool. The machine consists of a high vacuum chamber housing the mounting for the substrate, the ion gun, and the sputter target. Connected to the chamber are the gas handling system and the power supply for the plasma. To reduce the time required to pump the vacuum after sample installation the table can be transferred into a load lock, which is separable from the main chamber by a sliding seal.

During the sputter process, an argon plasma is ignited in the ion gun. The aluminum target itself serves as the cathode and a circular aperture above it as the anode. A high voltage ~400 V, applied between them, accelerates argon ions toward the target and free electrons in the opposite direction. After one initial ionization, occurring due to scattering with naturally present charged particles, scattering of

freed electrons and argon atoms on their opposite paths gives rise to an avalanche effect. This scattering rate is increased by a circular array of permanent magnets beneath the target, creating a static magnetic field that forces the charged particles on circular paths. Finally, ions hitting the target eject clusters of aluminum atoms which then fly toward the substrate. Argon is used as main sputter gas for its low reactivity. An additional mixture of 90% argon and 10% oxygen is used to oxidize the aluminum. The advantage of using a mixture lies in the increased precision when the total flow through the mass flow controller (MFC) is higher. A cleaning plasma can be ignited by applying the voltage between the shutter and the sample holder. This argon/oxygen plasma removes organic residues and water from the wafer surface.

The resistance of the metal film is determined by the scattering efficiency between sputtered aluminum and oxygen in the sputter atmosphere. Variable parameters are the plasma power and gas pressure, which both affect the sputter rate, and the oxygen partial pressure by adjusting the gas flow ratio of pure argon and the argon oxygen mixture, which then determines the sheet resistance. Doing so, films can be grown ranging from pure aluminum to granular films with sheet resistances well above the resistance quantum $R_Q = h/4e^2 = 6.45\,\text{k}\Omega$ [Rot+16].

Since the design of our nanowire oscillators strongly depends on their inductance, which for a given geometry in turn is defined by the film resistance, our fabrication depends on the ability to grow them with the desired resistance. To this end, we implemented a method of sputter monitoring and control.

Before sputtering, the sapphire substrate is cleaned in a piranha solution, a mix of hydrogen peroxide and sulfuric acid, removing organic residues including photo resist. Subsequently, $\sim$1 mm wide stripes of silver are deposited under an angle of $15°$ in the shadow evaporator later also used for the optical lithography (Sec. 3.2.3). The tilt leads to a wedge shape for better contact to the thin film to be sputtered. The rest of the substrate is covered with an aluminum hardmask. The so prepared wafer is then mounted on the plate of the sputter machine where it is fixed by two clamps. The latter are electrically connected to an ohmmeter outside (Fig. 3.6 a)). The measured resistance, together with values for the film thickness and sputter rate obtained from a quartz oscillator, is logged and displayed live by a toolset now included in qkit [qkit]. Extrapolation and comparison to previously recorded sputter traces (Fig. 3.6) allows for a prediction of the resistance at the target thickness resulting from the given settings. In-situ adjustments to the argon/oxygen mix flow can then be applied.

To reduce the necessary adjustments and prevent large gradients, we still perform tests on glass to determine starting values before the final film is sputtered. Due to
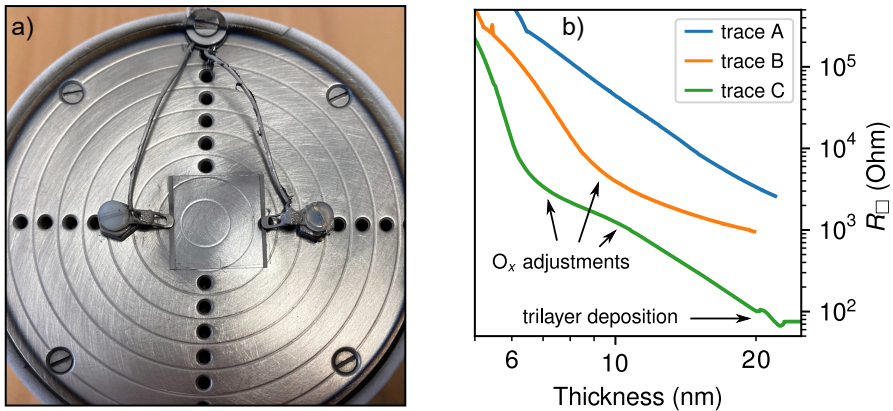
Figure 3.6: Photo of the sputter sample holder with DC contacts and measured resistance traces. **(a)** A $(2 \times 2)\,cm^2$ wafer is held by two clamps. The thin silver stripes on both chip edges ensure good electric contact to the film over the full width of the wafer. **(b)** Traces of resistances measured during the sputter process. The films form a well-conducting closed surface above around 6 nm thickness. Trace A was sputtered without adjustments until 2.45 kΩ were reached at 22.5 nm. During the deposition of trace B, the oxygen flow was increased between 8 and 11 nm resulting in a distinct kink and a resistance of 950 Ω at 20 nm. Trace C also features adjustments and additionally the signature of a trilayer deposition in a separate project dealing with long junctions [Wil+20]. After the first layer is deposited, a thin pure aluminum layer is sputtered and oxidized to form an insulating tunnel barrier to the third layer, which is added subsequently.

the sensitivity to slight changes in the gas composition or quality of the vacuum, variations in room temperature and humidity, even between the test and final run, immediately affect the result. Thus, the ability to fine tune and stop when the target resistance is reached in a tolerable range around the target thickness is of great benefit.

3.2.2 Defining nanowires

Starting from an unstructured granular aluminum film has several advantages. The sputter deposition is independent of the pattern so that films of different resistances can be prepared to be available on demand. During the deposition monitoring of the resistance is simpler as it is not influenced by conductor geometry and only given by the film conductivity and wafer dimensions. Additionally, the film is grown on a substrate not roughened by previous etching and can be cleaned more aggressively.

With a goal of 20 nm nanowire width, we have strong resolution requirements for the patterning. We therefore make use of electron beam (e-beam) lithogra-

phy. The Nanostructure Service Laboratory at KIT provides a JEOL JBX-5500ZD 50 kV e-beam writer. Additional to the writer's stage mechanics and alignment, factors limiting the resolution are found in scattering of the electron beam, the photoresist's structure, and finally anisotropies during transfer of the pattern into the metallization.

Overexposure quickly manifests in the inadvertent exposure of areas surrounding the written pattern by scattered electrons. Too small doses, on the other hand, lead to displacement or even dissolution of the exposed resist during developing. Therefore, test structures are written with varied e-beam doses to be subsequently checked with the help of a scanning electron microscope (SEM). Once the larger structures come out well, the dose used for the nanowires can be independently adjusted. Two different beam currents are used with the higher one offering greater speed for larger parts of the pattern. Switching between two currents requires the change of the aperture and re-alignment, which is performed by scanning marks on a separate chip. To make up for possible alignment errors, overlap regions are included in the design. While the constrictions leading to the nanowires are already written with the smaller current, the wires themselves are defined by single shots placed linearly along it. The dose of these shots is defined by a multiplier relative to the base dose in the order of 10. This multiplier is set close to the minimum necessary for the resist to form solid wires. The nanowire width is thus defined by this dose, scattering, and the resist.

Hydrogen silsesquioxane (HSQ) offers a sufficiently high resolution and, due to its inorganic nature, also a high resistance to chlorine and oxygen based etching processes. Diluted tetramethylammonium hydroxide (TMAH) is used as developer removing the HSQ that has not been exposed to the electron beam. The remaining HSQ then serves as etching mask in the shape of the structures, which are to be transferred into the metal. While organic photo resists are typically removed by solvents after etching, this is not possible with HSQ. After its molecular structure is cross-linked by e-beam exposure, it forms a hard, glassy, and electrically insulating surface. [Nam+98; HGK03]

For low-loss quantum circuits, clean surfaces are preferable as any contaminant potentially contributes dielectric loss (Sec. 2.3.3). Additionally, contacts between metal layers or directly to the granular aluminum by wire bonds are not possible through the insulating HSQ layer. Over the course of this project, two different processes (sketched in figure 3.7) have been implemented facilitating the subsequent removal of the HSQ. A listing of parameters applied in the following processes is included in the appendix.
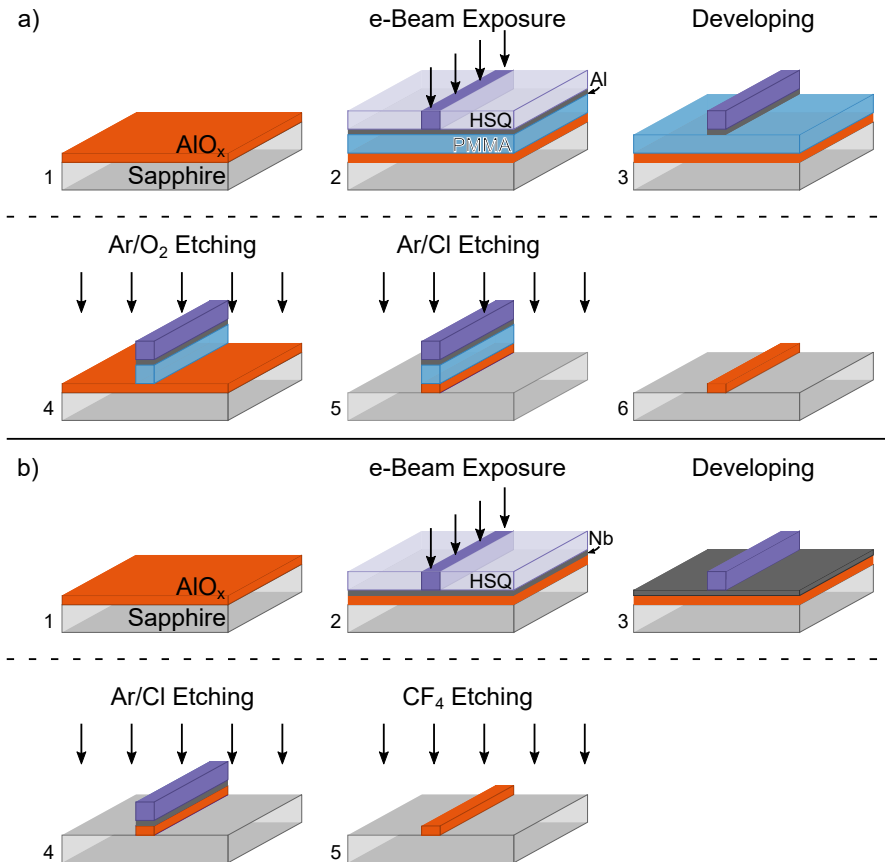
Figure 3.7: Illustration of the fabrication processes for our granular aluminum circuits. Layer thicknesses not to scale. **(a)** Double stack process: After sputter deposition of the metal film (1), PMMA is spun on top and covered with a thin aluminum layer to protect it from the solvents of the HSQ. After adding the HSQ, it is exposed with the e-beam writer (2). Developing with diluted TMAH removes the rest of the HSQ and the aluminum layer under it (3). A first etching step by an argon/oxygen plasma etches the uncovered PMMA (4). The structures are then transferred into the granular aluminum by etching in an argon/chlorine plasma (5). A last step removes the resist stack by solving the PMMA in organic solvents like NEP (6). **(b)** HSQ etching process: The HSQ is spun directly onto a thin niobium layer that later protects the film from the TMAH. After exposure (2) and developing (3) as in (a), the sample is directly etched with argon/chlorine (4). In a second etching step in a fluorine plasma the HSQ is etched off the metal surface (5).

Double stack approach

The first approach, in the following called the 'double stack process', makes use of an additional layer of the organic photoresist polymethylmethacrylat (PMMA) beneath the HSQ. After etching, the chip is cleaned in N-ethylpyrrolidone (NEP), an organic solvent with low vapor pressure, which removes the lower layer and thereby lifts the HSQ. This kind of double stack was introduced for high resolution lift-off processes, in which the metal is deposited on top of the resist [Yan+08].

PMMA is also used for e-beam lithography in processes with less stringent resolution requirements. In our case, its advantage in contrast to other optical photoresists lies in the reduced thickness of the layer, reducing the total height of the resist stack, which can limit the resolution. Additionally, the PMMA coating protects the aluminum from contact with the TMAH during development of the HSQ. Without this protection, the developer would quickly etch the metal, potentially destroying the structures. We use AR-P 672.03, a PMMA with 3% concentration from Allresist GmBH, and spin it on at 7500 rpm. The manufacturer states a thickness of 100 nm when spun on at 6000 rpm [All14].

After cleaning the substrate and spinning on the PMMA, a 3 nm thin layer of aluminum is evaporated on top of the PMMA to protect it from the solvents of the HSQ, which is spun on on top. The bake-out temperatures of 160 °C for the PMMA and 150 °C for the HSQ remain below the critical range above 200 °C where the sheet resistance of granular aluminum films was observed to start decreasing [Rot+16]. For our HSQ, Dow Corning XR-1541 with 2% concentration, we measured a layer thickness of (36 ± 4) nm with an atomic force microscope (AFM) after spinning on at 2000 rpm and after development. Exposure in the e-beam writer and subsequent developing leaves the pattern defined in HSQ on top of the PMMA. The aluminum layer underneath the unexposed HSQ is removed by the developer. Subsequently, etching is performed in an Oxford Plasma Technology – Plasma 100 inductively coupled plasma etcher. The process is sketched in figure 3.7 a).

First, the uncovered PMMA is removed by an argon/oxygen plasma. Next, the structures are transferred into the metallization in an argon/chlorine process. The oxidized aluminum films are etched up to ten times slower compared to pure aluminum, posing challenges to the resilience of the resist stack. To facilitate a clean transfer of the pattern from the relatively high resist stack into the hard metallization, the plasma power must not be too low. On the other hand, PMMA is known to exhibit a low tolerance to plasma etching [Mad18]. In first experiments with higher etching power we observed increased sheet resistances already after etching times that the HSQ can withstand. We attribute this to lifting of the HSQ during the plasma etching by softening of the PMMA underneath. Figure 3.8 a)
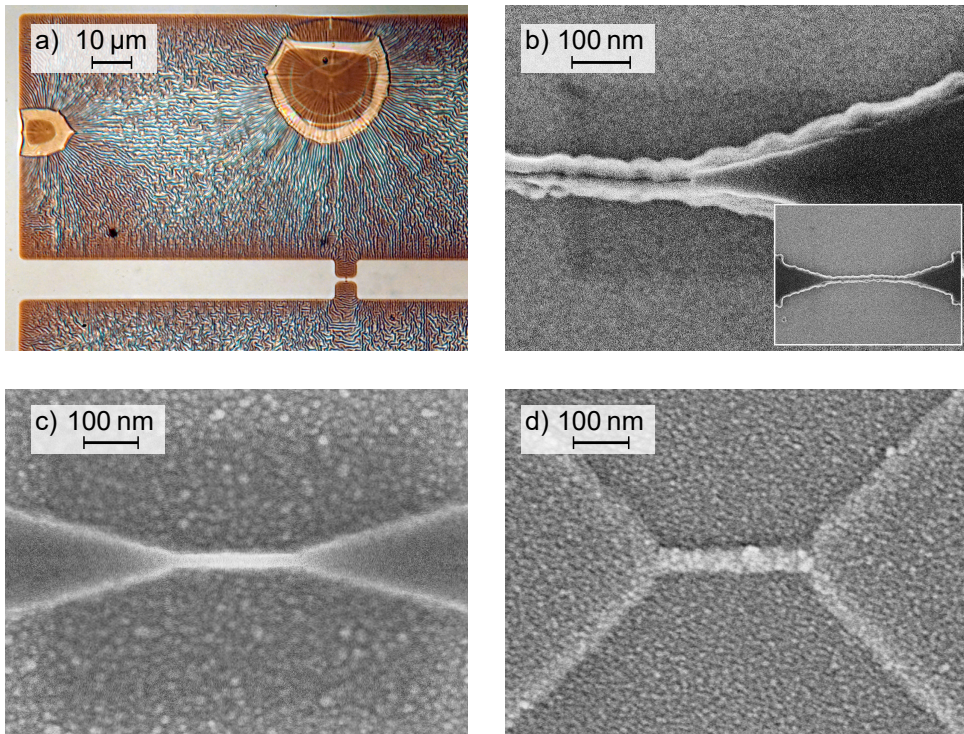
Figure 3.8: Microscopy images of etched samples. (a) Double-stack resist etched for 150 s during a trial of a more physical argon/chlorine plasma. When the PMMA becomes too hot, it can start flowing. This can result in cracking or even lifting of the HSQ on top. **(b)** SEM microscopy of the sample depicted in a). The PMMA is seen flowing out from under the darker HSQ on the constriction on the right. In the area of the wire, the HSQ seems to have broken away. **(c)** Nanowire after argon/chlorine etching without the PMMA layer but before CF$_4$ etching of the HSQ. The granular structure of the background is due to the platinum deposited on top for the conductive surface required in SEM microscopy. **(d)** Nanowire after both, argon/chlorine and CF$_4$ plasma etching. A thicker layer of Pt than in c) limits the picture resolution. The wider constrictions leading to the wire in contrast to b) and c) correspond to the final nanowire oscillator design.

and b) depict the result of tests with an increased etching time. Optical microscopy reveals a distinct schlieren pattern and places where the glassy HSQ top-layer broke due to tension. In the SEM photograph the PMMA can be seen to have flown out from underneath the HSQ. To prevent these effects, we limited the plasma power to 50 W and divided the process into steps of 7 s length with breaks in between, allowing the sample to cool down.

While intentional high power etching, during which the resist stack gets removed, might yield very narrow wires, their resistances and homogeneity will be questionable. Tests with a sample etched additionally, after the HSQ was removed, revealed

a fast rise of resistance (up to a factor of 2 in the large test structures after 10 s), above what would be expected from the thinning of the metallization. This can be explained by the faster etching of the pure aluminum grains in contrast to the oxide matrix they are embedded in.

For the resist stack lift-off the samples are put into NEP and heated to 80 °C for several hours. Additional ultrasonic helps remove the last residues.

HSQ etching

The second approach or "HSQ etching process" aims at removing the HSQ by etching it off the metallization after the patterns have been transferred. The challenge in doing so is the required selectivity of a process intended to etch only the resist but not the underlying metal. After exposure the HSQ behaves similar to SiO_x with a high chemical etch resistance [RW13]. Hydrofluoric acid (HF) can be used for HSQ removal in high resolution lift-off processes [Dua+11]. Highly aggressive and difficult to handle, HF is compatible only with a limited variety of materials like gold and fortunately also aluminum. Very large selectivities between SiO_x and aluminum can be obtained in dependence of the HF solution [Gab+20]. Easier to handle, fluorine based reactive-ion dry etching offers an alternative. Due to its resistance toward fluorine compounds aluminum oxide has already been proposed as mask material for the structuring of glass [Kol08].

For the process we implemented (sketched in Fig. 3.7 b)), HSQ is spun onto a 3 nm thin niobium layer, which was before evaporated onto the granular aluminum film. This passivation layer again serves to protect the film underneath from the TMAH containing developer. After exposure and developing as in the double stack process, the sample is directly etched in the argon/chlorine plasma, transferring the pattern into the metallization. Without the PMMA layer underneath the HSQ, the stack is less high and also less sensitive to the plasma power. We therefore etch with 100 W without interruptions. Figure 3.8 c) depicts a nanowire etched in the argon/chlorine plasma with the HSQ still on top, illustrating the high resolution facilitated by the HSQ.

A Sentech SI 220 Plasma Etcher is available in the CFN cleanroom for fluorine based dry etching. The HSQ remaining after the chlorine etch was observed to be quickly etched in a CF_4 plasma. Tests were conducted by measuring the film thickness with an AFM and the sheet resistance after several steps of etching. After around 20 s in a 100 W CF_4 plasma the resistance was measured around the value obtained from the film before etching and the ~15 nm HSQ left after the argon/chlorine etching appeared removed. After 80 additional seconds the resistance had only increased

by between 23 and 30% underlining the large selectivity. Especially in contrast to the effects of over-etching in a chlorine plasma, the timing appears much less critical. Figure 3.8 d) depicts a sample after the HSQ had been removed.

So far, no bad effects from possible aluminum fluoride residues have been observed, including in the performance of circuits fabricated with this process. If, however, they were found worth removing, this can be accomplished in the same machine by one additional step of milling in a pure argon plasma, similar to the milling used for inter-layer contacts (Sec. 3.2.4).

3.2.3 Optical lithography

For structures with less stringent resolution requirements, optical lithography offers a faster and less cost intensive alternative. We thus applied it to the fabrication of all larger structures added later. These are circuit parts providing the environment for microwave experiments as well as the DC contacts to our spiral oscillators. Using pure aluminum for these parts, the resonator frequencies are defined geometrically with good reproducibility and the lower room temperature resistance allows for DC pre-characterization before cooling down. The full process is illustrated in figure 3.9.

With the structuring of the granular aluminum parts finished, an optical photoresist is spun onto the wafer. We have made use of two different resists: Microposit[2] S1805 and AZ[3] 5214E. With both resists we achieved sufficient resolutions of 1 to 2 µm. Exposure is done with a Süss MA6 mask aligner through a chromium mask. The mask itself is written in a Heidelberg DWL 66 laser writer. Under irradiation with the light of a mercury-xenon lamp with 365 nm wavelength, the photoactive component of the resist reacts, making it soluble in the alkaline developer [Mad18].

Pure aluminum is added on top of the structured resist in a Plassys MEB 550S shadow evaporation tool using a focused electron beam to evaporate the metal. While S1805 is thinner with about 0.5 µm layer thickness and yielded sharper edges, the increased height of the AZ resist of about 1.2 µm appeared beneficial for the lift-off process. The greater ratio of resist to metallization thickness results in higher edges through which the NEP can attack. Heating of the sample in NEP to 90 °C

---

[2] Trademark of "DuPont de Nemours, Inc." formerly "Rohm and Haas Company":
`https://www.dupont.com/electronic-materials/litho-photoresists.html`
[3] Trademark of "Merck KGaA": `https://www.merckgroup.com/en/expertise/semiconductors/solutions/wafer-fabrication/photosensitive-patterning-materials.html`
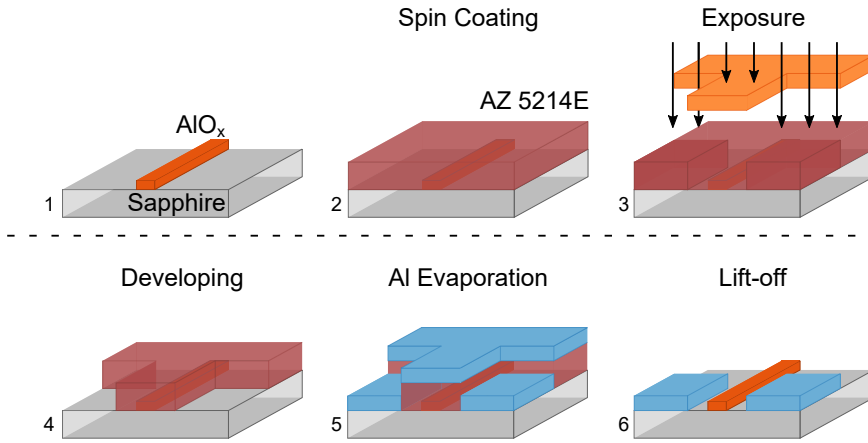
Figure 3.9: Illustration of the optical lithography steps. Starting from a sample with existing granular aluminum structures, the optical photoresist is spun on and exposed through an optical mask. The developer then removes the exposed resist, opening windows for the then added aluminum layer. In a lift-off process with organic solvents like NEP the resist with the superfluous metal on top is removed, uncovering again the previous structures and leaving the new ones in place. Layer thicknesses are not to scale.

and subsequent immersion in an ultrasonic bath is repeated until all superfluous metallization is removed.

3.2.4 Argon milling

Since our design features circuit parts structured in different lithography steps, inter-layer contacts require cleaning of the first layer before adding the second. While in situ oxidization of aluminum allows for the fabrication of tunnel barriers with the desired parameters, contact to normal atmosphere leads to a 3 to 4 nm thick [Eve+15] insulating layer of aluminum oxide that might also incorporate impurities.

One method of removing this insulating layer is by milling the structures with an argon ion beam. The ion beam is generated by the Kaufman source available in the shadow evaporator used for our pure aluminum layers. After ionization, the gas is accelerated by an acceleration voltage and passes a neutralization stage to prevent electrical charging of the target. The milling is performed with pure argon in a purely physical process, removing target material by momentum transfer. As a noble gas, argon does not chemically react with the film and does not remain on the surface. Tests of aluminum resonators that underwent this milling showed little to no negative effect on their performance, making the method applicable to
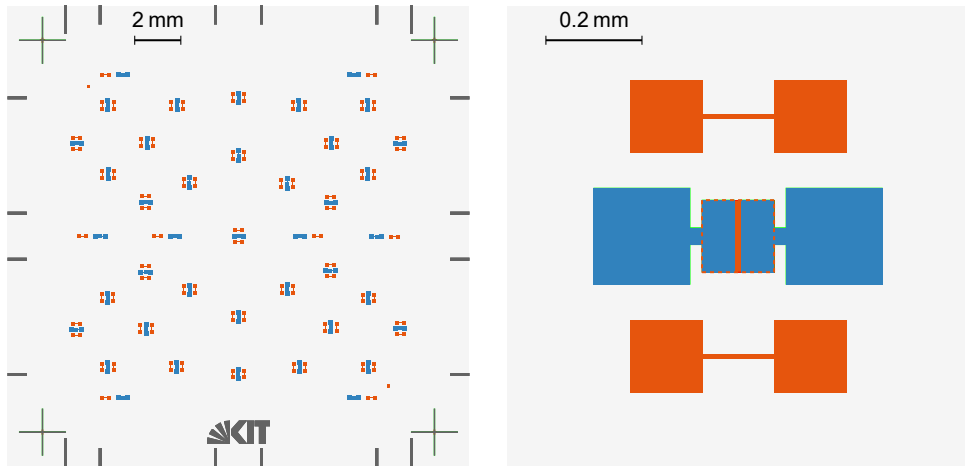
Figure 3.10: Inter-layer contact test structures. To enable good contact between metal layers added in different fabrication steps, the native oxide on the lower layer is removed by an argon milling process. These test structures, consisting of an granular aluminum square (orange) contacted by two overlapping aluminum contacts (blue), yield twice the contact resistance plus 1/10th of a square of the sheet resistance. The latter can be compared with the square reference strips.

high quality quantum circuits [Grü+17]. The same technique is commonly used for substrate cleaning, then usually with oxygen added for a more effective removal of organic residues.

While a similar native oxide layer is expected on the surface of granular aluminum films, there are certain differences. Since aluminum oxide makes up the insulating matrix of our films, it can be expected to get similarly milled by the ion beam and at a different rate than the pure aluminum grains. This might result in an uneven surface. Additionally, with only 20 nm thickness, our films require additional precision to prevent them from becoming too thin and thus highly resistive themselves. We thus conducted tests to determine working milling parameters.

The test structures depicted in figure 3.10 feature a $(150 \times 150)\,\mu m^2$ square of granular aluminum (orange) etched after a first step of optical lithography. In a second step, windows in the resist are defined where aluminum is to be added after milling (blue). They form two $(67 \times 150)\,\mu m^2$ overlap regions connected via 1/10th square of granular aluminum. The resistance measured between the two large pads multiplied by 10 should thus equal the sheet resistance if there is no additional contact resistance between the layers. For comparison, two $(10$ by $150)\,\mu m^2$ strips next to the contact test connect two pads for a measurement of the local sheet resistance.

Similar test structures are included on all later samples with inter-layer contacts. The strips for determination of the sheet resistance are then only 1 µm wide giving 150 squares since they are then defined by e-beam lithography.

3.2.5 Removal of DC contacts

One more step of optical lithography is required for samples that feature DC contact lines. Before microwave experiments, these lines have to be removed so as not to interfere with the circuit's dynamics. As they were previously contacted by wire bonds, residues along the two wafer edges featuring the bond pads prevent further lithographic steps. These edges are thus first cut away with a wafer saw. After removal of the protective coating, an optical photoresist is applied again on the now smooth surface. Exposure with a mask defining the regions on the $(5 \times 5)\,\text{mm}^2$ chips featuring the contact lines results in windows after development of the photoresist. These are then etched by an argon chlorine reactive ion etching process similar to the one used for the granular aluminum nanowires (Sec. 3.2.2). Finally, the photoresist is cleaned from the substrate by NEP, protective coating is applied once more, and the wafer is diced, yielding the four $(5 \times 5)\,\text{mm}^2$ chips for microwave experiments.

3.3 Experimental setup

Our experimental setup can be divided into the part required to establish suitable conditions, namely cryogenic temperatures and shielding, and the parts for measurement and control of our circuits.

3.3.1 Cryogenic refrigeration

The observation of quantum dynamics in superconducting circuits requires cooling to temperatures well below the critical temperature of the circuit material. Since measurement and control in our experiments is realized through coupling to microwave fields, shielding from thermal radiation is a prerequisite. For a single two-level transition in thermal equilibrium, the Maxwell-Boltzmann distribution yields the temperature dependent population probability as $p_{\text{MB}} = \exp(-\hbar\omega_{01}/k_{\text{B}}T)$. For a typical frequency of $\omega_{01}/2\pi = 4\,\text{GHz}$, this population becomes smaller than 1% only below $T = 42\,\text{mK}$. Therefore, our experiments are conducted in a dry dilution

cryostat cooling the sample to temperatures of around 20 mK. These temperatures are reached by a multi stage process in a vacuum environment.

A two stage pulse-tube cooler is used for pre-cooling down to ~ 3 K. This closed cycle system makes the cryostat independent of liquefied helium that otherwise requires an extensive infrastructure. Similar to a reversely operated Stirling engine with regenerator, the pulse tube derives its cooling power from the periodic expansion and compression of the helium used as working gas. In contrast to a Stirling engine in which a piston moves the gas, the geometry of the pulse tube itself acts as an impedance resulting in an effective displacement of the helium relative to the fixed regenerator. The compressor generating the pressure can be placed in some distance from the pulse tube, shielding the setup from noise and vibrations. [Rad03]

To reach millikelvin temperatures, a mixture of ^{4}He and its rare isotope ^{3}He is circulated in a second closed cycle. After being pre-cooled, the mixture is forced through a so-called Joule–Thomson valve. Sudden expansion of the gas volume results in a further temperature decrease and its condensation. Additionally, as the mixture is cooled below 1 K by a set of heat exchangers coupled to the return flow, two phases separate in the mixing-chamber. One is heavier with a smaller concentration of ^{3}He, one lighter and ^{3}He rich floating on top. The return flow is lead from the lower part of the mixing chamber to the still plate where it is heated, resulting in a continuous flow of ^{3}He out of the diluted phase. This outflow is compensated by ^{3}He from the concentrated phase. Similar to evaporation, this is an endothermic process taking energy from the surrounding and thus yielding the cooling power of the system. [EH00]

For sample characterization, transport measurements with less stringent temperature requirements can be performed in a pure ^{3}He cryostat reaching temperatures down to ~ 300 mK. This type of cryostat consists of an inner part, inside a vacuum cylinder, which is immersed into liquid helium. Through a capillary, ^{4}He is pumped from the bath into a small (1 K) pot. Once the cryostat is cold enough, this pot remains filled with a small amount of liquid ^{4}He. Its evaporation represents a first order phase transition, resulting in an exponential relationship of vapor pressure and temperature. By pumping on the ^{4}He vapor, its pressure and with it the temperature is reduced until about 1 K. This is cold enough for the condensation of ^{3}He contained in a closed cycle in a separate pot. Through the same mechanism as for the ^{4}He, now employing a sorption pump, this stage gets cooled to about 300 mK. The different temperatures are due to the difference of the latent heat in ^{4}He and ^{3}He [EH00]. While the length of a cooldown is limited to several hours before the ^{3}He needs to be re-condensed, such a system has the advantage of faster cooldown cycles, making it ideal for shorter measurements with changing samples.

3.3.2 Microwave setup

The devices used for generation and measurement of the microwave signals differ depending on the conducted experiment (Fig. 3.11). For spectroscopy, a vector network analyzer (VNA) is used as measurement device. VNAs allow for direct measurement of the complex scattering parameters (Sec. 2.3.4). Comparison of the emitted and the received signal yields the sample's influence on the amplitude and phase of a microwave in dependence of its frequency and power. While the frequency is continuously swept over a set range, the intermediate frequency (IF) bandwidth corresponds to the inverse of the time each point is measured. Commonly, the IF-bandwidth is in the range of few kHz. Compared to the ns timescales of the sample's dynamics, this can be viewed as a quasi continuous drive. The sample's response is thus in equilibrium with the measurement signal.

A second tone from a microwave source can be applied through a directional coupler combining two microwave inputs to one output. Independent in frequency and power from the VNA, this allows for two-tone spectroscopy. While the VNA sweeps its frequency trace recording the response of one circuit element (the readout), the second tone remains fixed exciting, for instance, a different circuit element. Two dimensional scans then map the frequency space, revealing excitations that couple to the readout influencing its response. The size of the parameter space and the required averaging can make these scans time consuming.

Once the sample's excitation frequencies are discovered, a different setup is used for measurements in the time domain. Arbitrary waveform generators (AWG) used for pulse generation have a finite time resolution, typically few gigasamples per second. This limits the frequency of the output waveform. Therefore, frequency mixing is used. The pulses are then generated at a lower intermediate frequency of typically 50 to 70 MHz. IQ-mixers[4] combine the AWG output with the GHz measurement and control tone (LO). The result are pulsed signals at the sum[5] of the frequencies with nanosecond resolution. This technique was introduced already for pulsed magnetic resonance measurements [FR81].

Observing single quantum transitions requires operating with a small number of photons. This is possible by employing a sophisticated chain of attenuation and amplification. Thermal radiation is also expected to be fed into the coaxial cables connecting the measurement equipment at room temperature to the sample. To achieve a desirable ratio of noise photons to signal of $< 10^{-3}$, a total of 60 dB

---

[4] IQ: In-phase and quadrature; the latter denoting the 90° phase shifted component
[5] or difference, depending on the relative phases
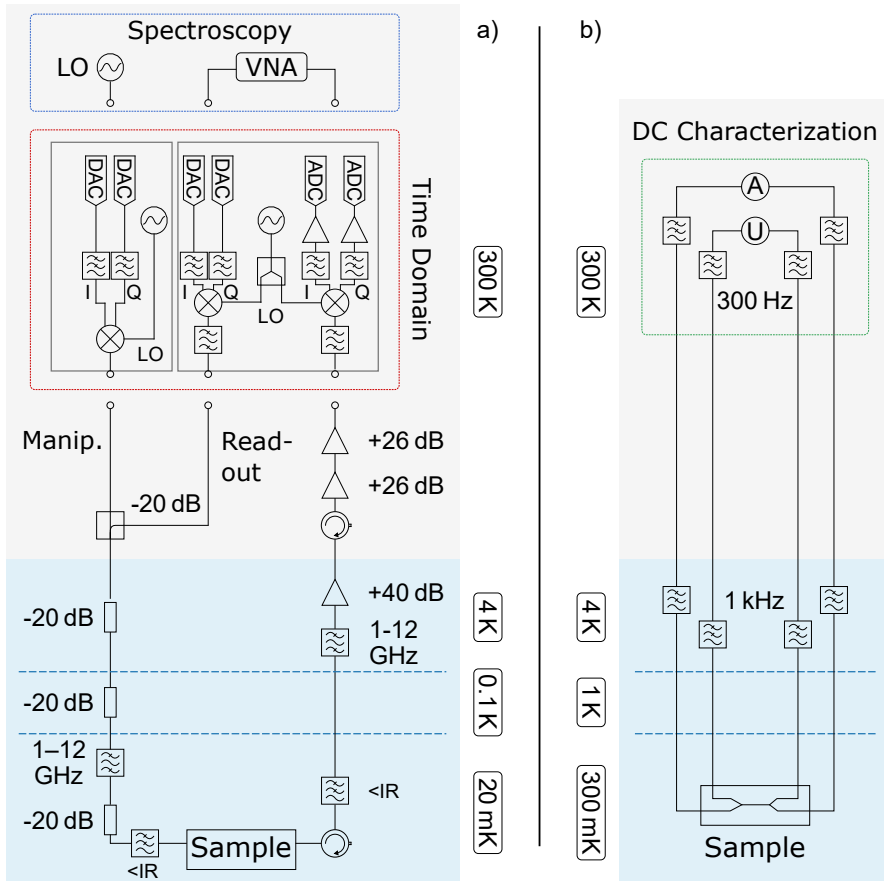
Figure 3.11: Measurement Setups. (a) The microwave setup (left) consists of the room temperature measurement equipment as well as the attenuated and re-amplified microwave lines leading to the sample in a dilution cryostat. The microwave signals are generated either by a VNA and a microwave source for continuous drive two-tone spectroscopy measurements or by a pulse generating time-domain setup, mixing fast digitally generated low-frequency pulses with the high frequency signal from a microwave source. The signal is filtered, attenuated and thermalized by 60 dB on consecutive temperature stages. After interaction with the sample, it is then re-amplified first by a HEMT and additional room temperature amplifiers. **(b)** For DC characterization, a four-point measurement setup is connected through filters with the sample at 300 mK in a ³He cryostat. Additionally, current pulses can be applied with subsequent recording of an I-V curve for controlled adjustments of the wire resistance.

attenuation along the input line is required [Kri+19]. Since each attenuator itself emits black body radiation with a spectrum depending on its temperature, they need to be well thermalized at the low temperature stages of the cryostat. This is typically done in subsequent steps to reduce the thermal load on the millikelvin measurement stage where the cooling power is minimal.

After interaction with the sample, the measurement signal needs to be amplified again to be observable at room temperature noise levels. To this end, high electron mobility transistor (HEMT) amplifiers are installed at the 4 K stage. Circulators, which transmit the signal only in one direction, are used to shield the sample from noise emitted by the amplifier traveling back through the not attenuated superconducting output line.

The nanowire oscillators in the spiral geometry featuring DC contact lines are designed to be characterized at low temperature before microwave measurements. This is possible with the help of a second setup (Fig. 3.11) connecting the sample in a ^{3}He cryostat. Through two lines per oscillator a current can be applied. The locally dropping voltage is then measured with a second pair of lines. Doing so, I-V curves are recorded, sweeping the current in both directions. The critical current of a superconducting wire is observed on a trace coming from negative to positive currents at $+I_c$ and at $-I_c$ in the return trace. Coming from currents greater than I_c, the wire will become superconducting at lower currents due to heating effects and limited damping of the superconducting phase. In voltage-bias mode, the setup is operated conversely, applying a voltage and measuring a current. This is especially necessary for the measurement of nanowires with insulating behavior. In current-bias mode, the current source would always provide the voltage necessary to drive the set current, while by setting a voltage the insulating regime can be slowly scanned below the critical voltage, above which the nanowire conducts resistively and thus induces heating.

3.3.3 Sample holder and shielding

Protection of the sample is of great importance for quantum experiments. Additional to carefully designed circuits, the sample holder provides a first layer of protection from the environment and its interference with the studied system (Sec. 2.3.3).

For microwave measurements, the sample chip is glued into an aluminum box (Fig. 3.12) providing the SMP plugs connecting it to the microwave setup, additional shielding, and physical protection. From two milled copper lines, wire bonds connect to the sample's transmission line. Together with the lid, the box encloses
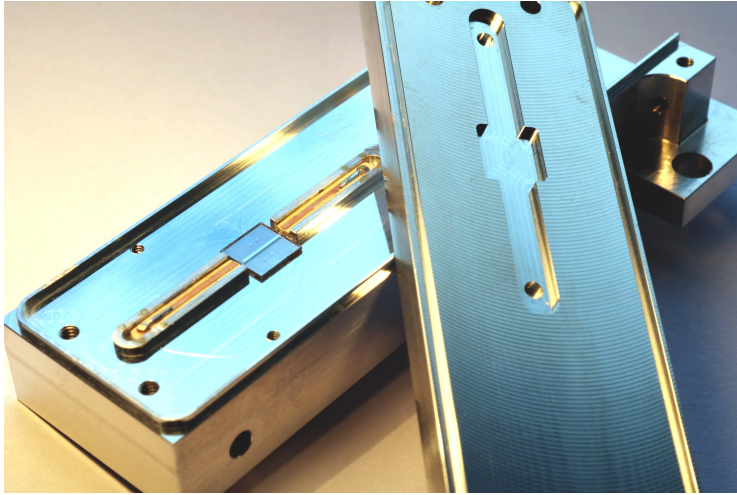
Figure 3.12: Sample in aluminum microwave sample box. A $(5 \times 5)\,\mathrm{mm}^2$ microchip is mounted in an aluminum sample holder. The on-chip transmission line is connected via wire-bonds and copper leads to SMP plugs in the bottom of the box. Conductive silver paste is used to fix the chip, establishing a connection between its backside metallization and the sample holder. The body of the latter is connected to ground via the outer coaxial cables and the cryostat. The lid features a notch for the chip and connectors.

the chip in a superconducting cavity designed to have no modes in the relevant frequency range.

While the aluminum sample box becomes superconducting itself and thus provides shielding from external magnetic fields, it does so only below its critical temperature of $1.2\,\mathrm{K}$. To prevent the trapping of flux vortices in parts of the sample metallization with a higher T_c, additional shielding is preferable. For this, we make use of two layers of shielding. First, the sample box is inserted into a shell of lead which becomes superconducting already above $7\,\mathrm{K}$. Both together are then again shielded by an outer layer made from a high-permeability nickel iron alloy like cryoperm[6], which retains its permeability at cryogenic temperature. Magnetic fields are pulled into the outer shield, deflecting them around the sample before reaching the inner layers.

For the low-temperature DC measurements of our spiral oscillators with contact lines, a second sample holder allows for mounting the full $(2 \times 2)\,\mathrm{cm}^2$ wafer. Two screws clamp the wafer onto a raised copper base, around which a milled circuit board is fitted (Fig. 5.1). The clamping obviates the use of glue, which

---

[6] Trademark of "Vacuumschmelze GmbH & Co. KG": `https://www.vacuumschmelze.com`

65
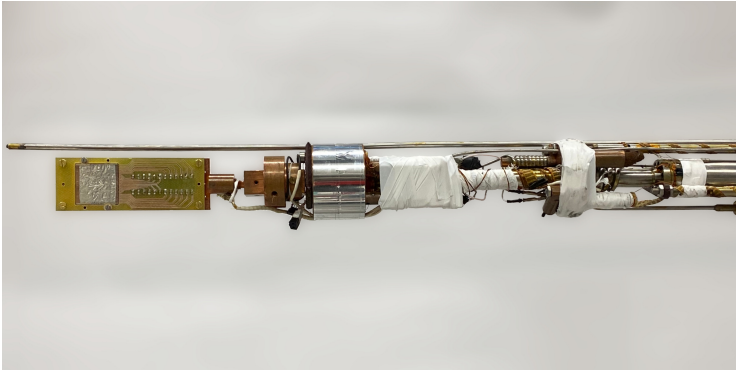
Figure 3.13: ^{3}He Cryostat and DC sample holder. Inset of the ^{3}He cryostat with the DC sample holder providing 24 contacts to a $(2 \times 2)\,\text{cm}^2$ wafer mounted to its end. Closed by a vacuum shield and inserted into liquid helium, the sample can be cooled down to 300 mK for characterization and adjustments of its superconducting transport properties.

would have to be carefully cleaned before further processing of the sample for microwave measurements. The circuit board provides 24 copper lines connected to the measurement setup. The wafer, on the other hand, featuring 16 nanowire oscillators with four contact lines each, has 32 bond pads on opposite sides (Fig. 3.5). Measuring all samples thus requires four cooldowns, reconnecting the wire bonds, and turning the chip by $180°$, which also is facilitated by the clamping. In addition to eliminating the line resistance from room temperature to the sample, the use of four-point contacts also provides redundancy and the ability to test the lines at low temperatures. By measuring the resistance between two lines leading to the same side of the nanowire, broken lines can be detected. Such a circuit can then still be measured by two-point probing.

4 Into the quantum regime

Our motive for employing granular aluminum nanowires in superconducting quantum circuits is twofold. The first is to gain new insights into the physics of disordered nanowires. We have introduced the material properties making granular aluminum an interesting material for applications (Sec. 2.2). While these properties emerge from the intrinsic disorder, new properties can be expected to arise when the dimensions of the system are additionally constrained. As the large kinetic inductance and resulting high impedance are determined by the macroscopic normal state resistance of a given circuit, they do not depend on the exact dimensions. This is illustrated by the commonly used measure of sheet resistance, yielding the same result for the same number of dimensionless squares. For the presented model describing the nonlinearity of the material in the picture of a series array of effective junctions (Sec. 2.2.2), the only geometric prerequisite was for the structure to be well larger than the physical grains, averaging out local disorder. This boundary is the one we intend to cross.

In section 2.2.3 we described how single granular aluminum nanowires can exhibit very different transport regimes. The underlying dynamics are unique to narrow wires with a width close to the coherence length ($w \sim \xi$). Depending on the resistance, the critical current in a given geometry can vary over a wide range, or even be fully suppressed in the presence of a high phase slip rate. The differences in behavior of wires with similar resistances but different geometries enable probing of the transition between macroscopic material properties and those dominated by the microscopic internal structure.

Complementary to the DC characteristics, the internal dynamics of nanowires manifest in the response of a circuit in the microwave regime. The observed frequencies account for the system's energy spectrum. Anharmonicity, lowering transition frequencies with rising excitation, gives insight into the nonlinearity. Finally, excited state lifetimes and coherence are measures for the circuit's coupling to the environment and susceptibility to fluctuations like external noise or phase slips. Importantly, by employing our disordered nanowires in an experimental platform well understood, observed differences can be attributed to the novel circuit element.

In addition to fundamental research, benefits can also be found for applications of quantum circuits. Not only could specific applications profit from high nonlinear inductance circuit elements made from a single material layer, but understanding of observed limitations in comparison with existing Josephson junction designs can help locating their origins.

Once coherence is established, transferring to the high resistance regime might enable distinguishing dissipative from dissipationless phase slips and the realization of coherent phase slip devices with granular aluminum nanowires. After all, a system naturally exhibiting both, insulating and supercurrent carrying behavior, seems to be an appropriate choice for studying duality.

For a first realization of our nanowire oscillators, we chose the single-layer design introduced in section 3.1.3. By fabricating the whole circuit from the same material, we foremost aimed at simplicity. Since in first-order approximation the nonlinearity is proportional to the relation $(I/I_\mathrm{c})^2$, a large total inductance outside of the nanowire limiting I_c will reduce it. On the other hand, the circuits become very compact and the electric field across the nanowire is smaller. The latter might be beneficial in terms of dielectric loss. In terms of simplicity, the absence of inter-layer contacts is valuable and additionally reduces the complexity of the fabrication process.

4.1 Microwave response

The nanowire oscillators studied in this chapter were fabricated by the PMMA/HSQ double stack process detailed in section 3.2.2. Microscopy images (Fig. 4.1) show the half-wavelength ($\lambda/2$) readout resonator and the nanowire oscillator coupled to it capacitively. Installed into their microwave sample boxes and magnetic shields, the samples were cooled down in a dry dilution cryostat to $\sim$20 mK. The microwave response was probed by feeding signals through a microwave transmission line (just below the image region), which then couple capacitively into the readout resonator, resulting in an absorption dip and phase shift at the resonance frequency $\omega_\mathrm{r}/2\pi$.

Three nanowire oscillators were studied for their response in spectroscopy as well as the time-domain. S1 features a 350 nm long wire, in S2 its length is 50 nm, and in S3 100 nm. Applying a dispersive readout scheme (Sec. 2.3), the readout resonators' microwave response was first probed while scanning a wide frequency range with a second microwave tone. Excitation of the nanowire oscillators manifest in the shift of the resonance probed in a single point and thus a shift in its amplitude and
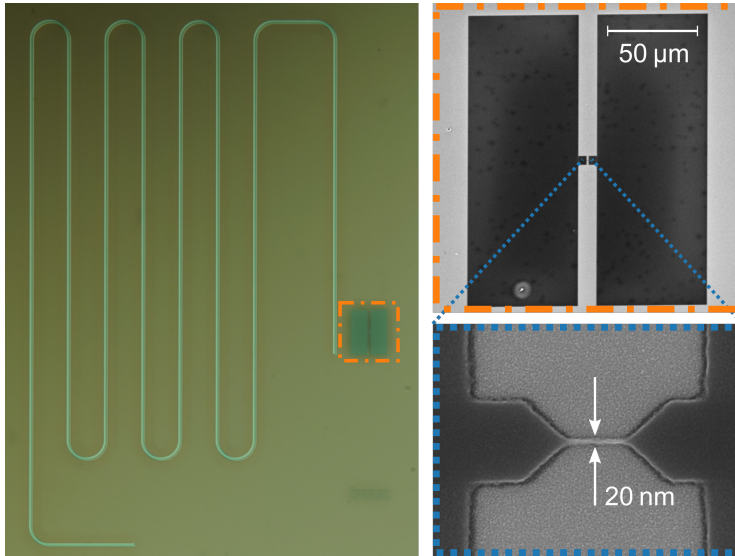
Figure 4.1: Microscope images of a nanowire oscillator and readout resonator. On the left, an optical microscopy image depicts the a nanowire oscillator (in orange frame) capacitively coupled to its $\lambda/2$ readout resonator. At the lower edge, the coupling arm of the resonator to the transmission line (outside the image region) is seen. SEM images show closeups of the nanowire oscillator in the single layer design. The paddles constitute the capacitance. From there, stepwise constrictions lead to the nanowire.

phase. Figure 4.2 shows the resulting lines in the amplitude signal for the three samples in dependence of the second tone's drive power. Toward higher powers, the lines broaden and exhibit a distinct asymmetry with their peak appearing at lower frequencies. Multi-photon transitions to higher levels require higher drive powers and, in case of a negative anharmonicity $\alpha = (\omega_{12} - \omega_{01})/2\pi$, appear below the fundamental transition. At the same time, the lines broaden with increasing power, making it impossible to resolve separate lines when the anharmonicity is small.

The coupling between nanowire oscillator and readout resonator was measured in S1 by observing the shift of the resonator while increasing the power driving the nanowire oscillator at the frequency obtained from two-tone spectroscopy. This results in a shift seen in figure 4.3 b) toward higher powers, where it reaches an equilibrium. Continuous driving of a two-level transition averages to a population of $1/2$. Higher transitions that can be driven at high powers in a system with small anharmonicity make the derived coupling an effective quantity for the combined system. From the derived shift of (0.6 ± 0.1) MHz and the frequency detuning between the two systems of $\Delta = (488 \pm 1)$ MHz, this coupling is calculated to
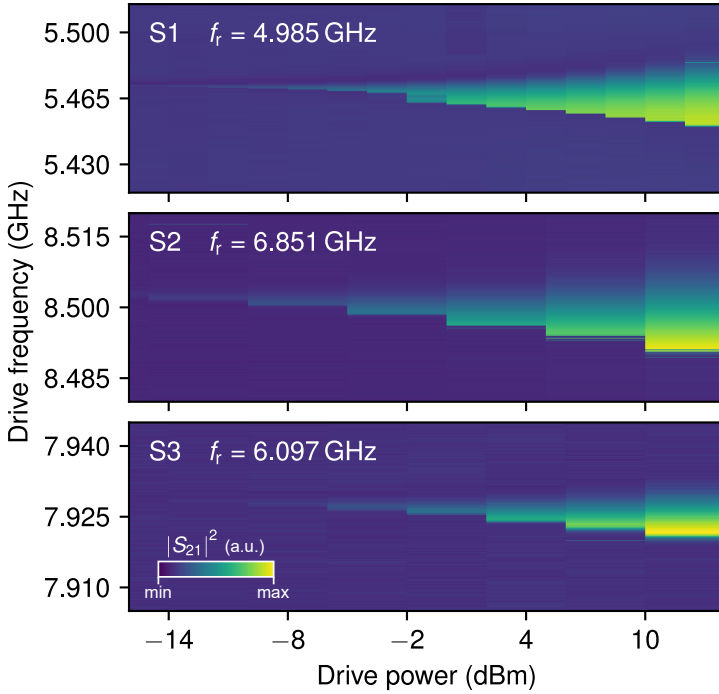
Figure 4.2: Spectroscopy of nanowire oscillators. Sweeping a second microwave tone while observing a single point in the resonance dip of the readout resonator results in an observed peak in $|S_{21}|^2$ when the dip shifts. These are here color coded for the three studied samples. Due to the line broadening at higher drive powers, lines due to higher level excitations are not resolved separately but manifest in the visible asymmetry. At low drive powers, the lines become very narrow with linewidths below 1 MHz. [Sch+20]

be (17 ± 2) MHz. The disparity between this value and the one from simulation (Fig. 3.4) could be explained by the high kinetic inductance material also of the capacitive paddles altering the current distribution and adding to the difference expected due to the frequency detuning. In S2 and S3, which on the other hand were much further detuned from their readout resonators, the coupling distance was reduced from 50 to 30 μm.

Prior to cooling down, we measured the resistance of sample S1 at room temperature with a needle probe. This is challenging because of the small sizes and due to the required care with the current excitation. The values for S2 and S3 were therefore obtained after low temperature measurements to avoid scratches in the capacitive parts of the circuit. From the measured total circuit resistance 6 squares with the wafer's sheet resistance $((2 \pm 1)$ kΩ for S2 and S3) were attributed to parts outside the wire, following geometric considerations of the design. A
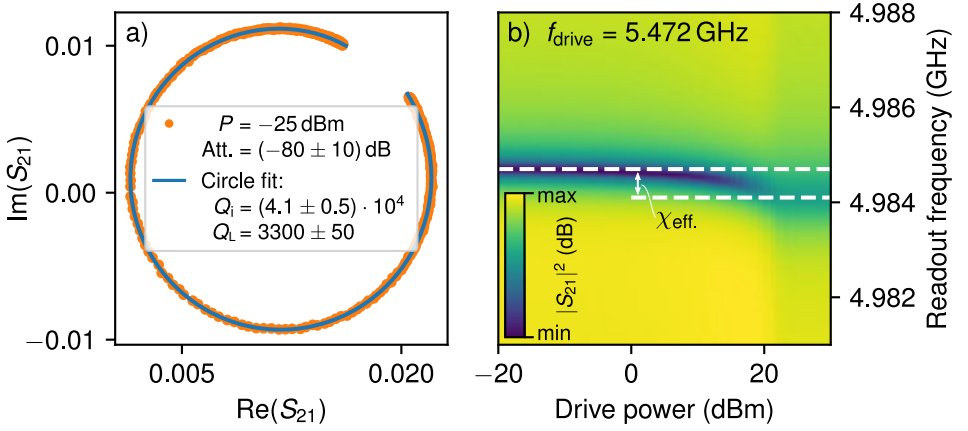
Figure 4.3: Readout resonance circle and dispersive shift. (a) The quality factors of the readout resonator coupled to S1 are obtained from a circle fit to its resonance observed in the scattered microwave signal S_{21}. **(b)** Increasing the drive power at the frequency obtained from two-tone spectroscopy (Fig. 4.2) results in a shift of the resonator by $\chi_{eff.} = (0.6 \pm 0.1)$ MHz. Since the shift increases to higher powers, higher levels are excited and this yields an effective, combined coupling.

higher precision for the wire resistance can be achieved by a scheme of four-probe measurements at low temperature, which is presented in the next chapter. The measurement in S1 preceded the systematic study of the effect of current pulses on the nanowire resistance (Sec. 2.2.3) and might have reduced the latter, which is therefore given only as a bound. Such a reduction would also reduce the ratio of inductance contributed by the wire compared to the total inductance of the circuit. For S1, the chlorine etching was performed in the manner applied in the HSQ etching process, while for S2 and S3 it was adjusted to the sensitivities of the PMMA. Table 4.1 provides an overview of the sample parameters. The given frequency estimate was calculated as $1/2\pi\sqrt{L_kC}$ with L_k being the kinetic inductance calculated from the full circuit resistances (Eq. (2.38)) and C the capacitance. This estimate does therefore not include any effects arising due to nonlinearity and lies above the observed frequencies in the samples with larger wire resistance.

4.2 Rabi oscillations

Two-tone spectroscopy revealed information about the energy and coupling of the nanowire circuit. In this section, we will ascertain whether we can drive a single transition in a controlled manner and find information about the level spectrum without direct spectroscopy of the transitions.

Table 4.1: Properties of the sample circuits. For the three samples S1, S2, and S3 with wire length l_W and room temperature wire resistance R_W estimated from the total circuit resistance, two-tone spectroscopy yields the transition frequencies f_{01}. Their readout resonators have frequencies f_r. A harmonic frequency estimate $f_{est.}$ is calculated by $1/2\pi\sqrt{L_k C}$. Time-domain measurements (Sec. 4.3) yield the circuit's lifetimes. [Sch+20]

Sample	l_W (nm)	R_W (kΩ)	f_r (GHz)	f_{01} (GHz)	$f_{est.}$ (GHz)	Lifetime (μs)
S1	350	< 7	4.99	5.47	5.2 ± 0.3	3.4 ± 0.1 ($0.8 \pm 0.2\ T_2$)
S2	50	7 ± 1	6.85	8.50	9.2 ± 0.4	4.0 ± 0.1
S3	100	10 ± 1	6.10	7.93	8.3 ± 0.4	3.4 ± 0.1

Pulsed time-domain measurements allow the observation of an excited system's time evolution. Repeated application of drive pulses of varied length and subsequent measurement of the system's excitation in a dispersive readout scheme (Sec. 2.3) amounts to a recording of the system's Rabi oscillations. For a two-level transition, the Rabi frequency $\Omega = \sqrt{g_m^2 + \Delta_m^2}$ (Sec 2.3.1) is expected to increase linearly with the drive amplitude. The second term leads to a zero-drive offset, corresponding to the detuning of drive tone and transition frequency for off-resonant driving. Thus, driving these oscillations with varied amplitudes allows for a test of the two-level character of the coupled system and a precise measurement of the transition frequency. The IQ mixers used in the generation of fast microwave pulses have a limited power range and their response is not perfectly linear. This limits the studied amplitude range in the following and requires a calibration. The power of the pulses has thus been additionally measured for calibration with a spectrum analyzer.

Indeed, the Rabi frequency of our samples was found to exhibit a clear dependence on the drive amplitude [Sch+20]. Figure 4.4 a) depicts the relative excitation of the driven transition in sample S2 oscillating with time for different drive amplitudes. The acquired data was fitted to a damped sine, yielding the the Rabi frequency. For the two samples S1 and S2, the result is shown in figure 4.4 b).

At low drive amplitudes, the observed behavior agrees with the two-level model. Data points lie in a small error band obtained by variation of the amount of fitted points between 6 and 16. The obtained offset agrees with the detuning expected from comparison with direct spectroscopy. Primarily, a small offset yielded cleaner oscillations, which is explained in the next section by investigation of the frequency dependence.

Deviation from the model is observed for higher Rabi frequencies. This behavior is expected as a consequence of higher order transitions to additional levels beyond the two-level model [Cla+04; Dut+08]. When Ω exceeds the system's anharmonicity,
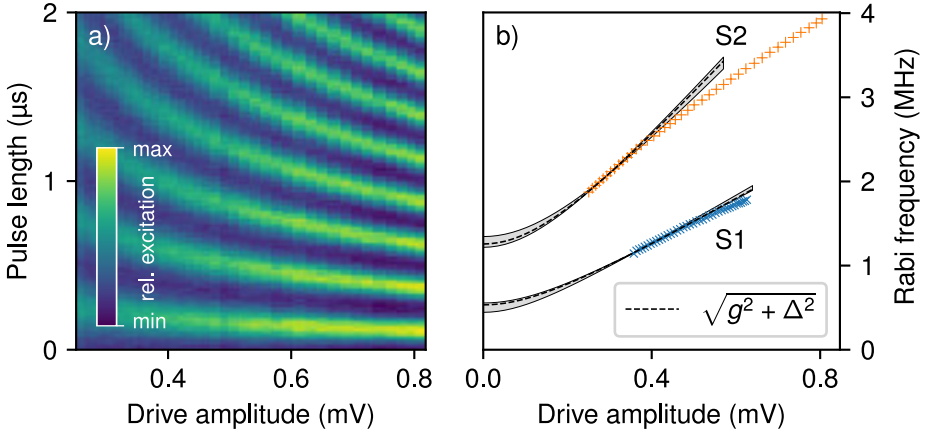
Figure 4.4: Rabi oscillations and frequencies in dependence of the drive amplitude. (a) Rabi oscillations measured in S2 by applying drive pulses at the transition frequency ω_{01} of varied length and subsequent measurement of the circuit's state. The Rabi frequency increases with increased drive amplitude. **(b)** $\Omega/2\pi$ of S1 and S2 plotted against the drive amplitude. Until the trends start to deviate at higher amplitudes, they fit to the model for two-level systems. Deviations are expected when $\Omega/2\pi$ exceeds the anharmonicity. For the error bands, the points included in the fit were varied between 6 and 16. Higher level excitations can also explain the larger dispersive shift observed toward the right edge in (a). The extracted detunings $\Delta_{S1}^{fit} = (0.5 \pm 0.1)\,\text{MHz}$ and $\Delta_{S2}^{fit} = (1.3 \pm 0.1)\,\text{MHz}$ agree with the values from comparison to spectroscopy measurements of $\Delta_{S1} = (0.8 \pm 0.5)\,\text{MHz}$ and $\Delta_{S2} = (1.8 \pm 1)\,\text{MHz}$ respectively. In S1, a smaller anharmonicity can be expected from the smaller ratio of wire to full circuit inductance. [Sch+20]

leakage into higher levels reduces the power driving the fundamental transition and thus Ω for higher powers.

So far, we have shown that transitions in our nanowire oscillators can be excited and measured. To gain further insight into the presence of higher level transitions, we examined the dependence of Ω on the drive frequency.

Since in the absence of higher levels the effect of the detuning term in equation (2.52) is symmetrical, so is the expected increase of Ω around ω_{01} for a fixed drive power. At the same time, an off-resonant drive can no longer excite transitions around the whole Bloch sphere [HR06], resulting in a decrease of the Rabi amplitude. However, a clear asymmetry was observed in our circuits (Fig. 4.5 a)). At drive frequencies greater than ω_{01}, the Rabi fringes run closer with increasing frequency and fade out with decreasing amplitude as expected. Below ω_{01} by contrast, Ω continues to decrease before the pattern is sharply interrupted. In this region, the oscillations quickly decay with increased pulse lengths.

In systems with small negative anharmonicity, multi-photon transitions to the n-th level can be excited at frequency below ω_{01} given by ω_{0n}/n [Bra+15]. As
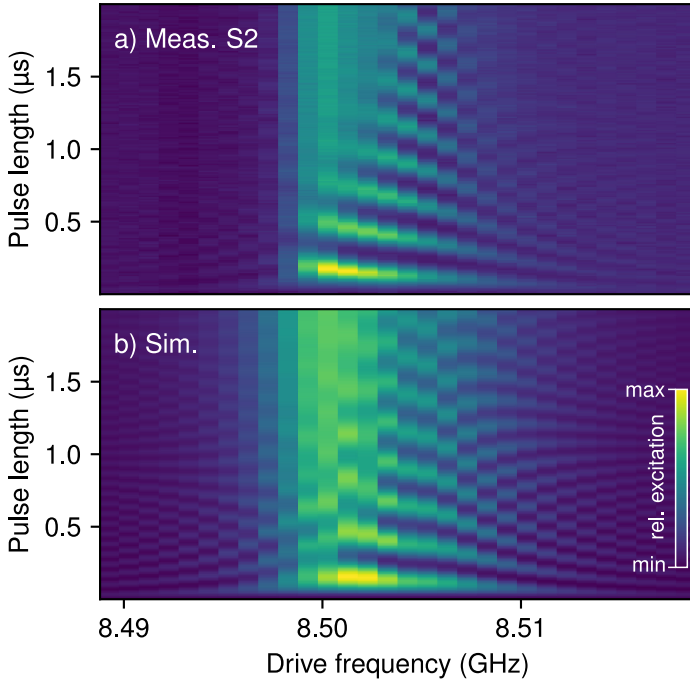
Figure 4.5: Rabi oscillations in dependence of the drive frequency. (a) Rabi oscillations measured with S2 exhibit a clear asymmetry. The Rabi frequency of a driven two-level system is expected to increase symmetrically around ω_{01} while their amplitude decreases as the system is only partially excited. While this behavior is here observed at frequencies larger than ω_{01}, the continued decrease of Ω below ω_{01} can be attributed to higher level excitations occurring at these lower frequencies. **(b)** Numerical Floquet matrix calculations yield a similar behavior for an anharmonic oscillator, here with 1.3 MHz anharmonicity. This is also in agreement to the estimate from figure 4.4. [Sch+20]

drive pulses have a finite linewidth, a region deviating from the two-level model is expected around and below ω_{01} while above at low enough powers only the fundamental transition may be excited. To support this interpretation, we applied a numerical master equation simulation to our circuit. The model introduced in section 2.4 considers multi-photon transitions to higher levels and loss by decay and dephasing. To reduce the amount of varied parameters, some were fixed at values extracted from separate measurements. In the result depicted in figure 4.5 b), the decay times were set to 4 μs energy lifetime and 1 μs dephasing time, in the order of what was observed in measurements (Sec. 4.3). The drive amplitude parameter in the model of 0.0023 was adjusted by focusing on the off-resonant edges, where higher order transitions are not dominant. To flatten the approach toward ω_{01}, a small shift of the transition frequency of $\omega_{\mathrm{s}}/2\pi = -2\,\mathrm{MHz}$ in a small region $\epsilon = 1\,\mathrm{MHz}$ around ω_{01} is considered, which might be due to the AC Stark effect

[Sch+18] and the nonlinearity of the inductance. We simulated 6 Floquet states and 5 circuit levels, above which the time required for the matrix diagonalizations strongly increased while the result did not noticeably differ. With this approach, the key characteristics of the measurement are reproduced, assuming an anharmonicity of $(1.5 \pm 0.3)\,\mathrm{MHz}$. [Sch+20]

Still, differences between the applied model and measurements should be expected since its Hamiltonian is of the phenomenological form of an anharmonic oscillator. The precise form of the energy shape depends on physical properties, which at this time are not fully known. This includes for instance the exact current-phase relation of the nanowires and the manifestation of inhomogeneities in the wire. Future models that include these can then also account for differences in the coupling of the drive to higher levels and their individual decay rates. The latter have so far not been directly measured and we focused on reducing the amount of free parameters in a simpler model. [Sch+20]

At this point, we can conclude that our circuits allow for the controlled excitation of two-level excitations, providing anharmonicities sufficient at low enough drive powers, especially when driven slightly detuned above ω_{01}.

4.3 Lifetimes and coherence

With control over the state of our nanowire oscillators, we now focus on the excitations' lifetimes. The pulse length required for the system's excitation t_π is extracted from a fit to the Rabi oscillations. To extract the energy relaxation T_1, the waiting time after each applied π-pulse is varied before the system is read out. The relative excitation depicted in figure 4.6 a) corresponds to the probability of finding the system in its excited state after a given waiting time and decays exponentially $\propto \mathrm{e}^{-t/T_1}$ (Sec. 2.3.3). In the measured nanowire oscillators, the recorded T_1-times ranged between 3.1 and 4 µs. [Sch+20]

By applying two pulses with a frequency slightly detuned from ω_{01} and length $t_\pi/2$ separated by a varied delay, Ramsey fringes can be recorded. The frequency of their oscillation corresponds to the detuning and the exponential decay of their envelope yields the coherence time T_2 of the system. Figure 4.6 b) depicts a measurement performed on S1 yielding a coherence time of 0.82 µs. [Sch+20]

To uncover further potential for optimization, we examine factors that might limit the performance. One often dominant decay channel is loss into the readout resonator. This is estimated by the single-mode Purcell formalism (Sec. 2.3.3) $\gamma_{\mathrm{P}} = (g_{\mathrm{r}}/\Delta_{\mathrm{r}})^2 \kappa$ [Pur46; Hou+08]. Spectroscopy measurements of sample S1 described
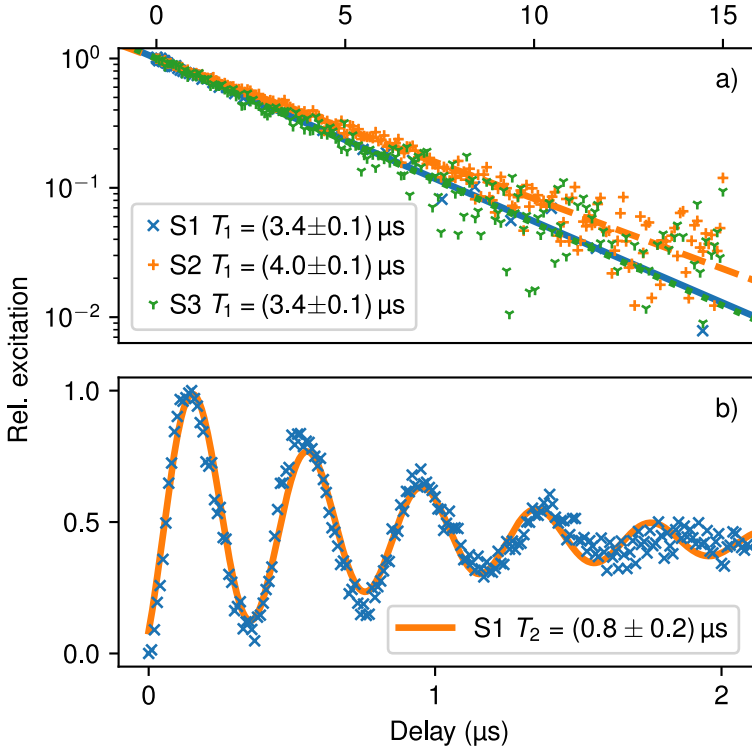
Figure 4.6: Lifetimes measured in nanowire oscillators. (a) T_1 measurements in the three samples S1, S2, and S3 yield lifetimes between 3.4 and 4 µs. **(b)** In S1, a Ramsey experiment yields the characteristic fringes due to coherent phase oscillations with a T_2 of about 0.8 µs. [Sch+20]

before yielded an effective coupling strength of $g_r = (17 \pm 2)$ MHz and a resonator linewidth $\kappa = (1.5 \pm 0.2)$ MHz from the fit depicted in figure 4.3 a). Together with the frequency detuning $\Delta_r = (487 \pm 1)$MHz between the two oscillators, the Purcell lifetime limitation for S1 is (85 ± 14) µs. Due to the character of the coupling strength as effective quantity, this value is to be seen as a boundary for combined excitations. Still, it is found to be much larger than the observed T_1 time and Purcell loss is not a dominant mechanism. [Sch+20]

An often cited loss mechanism is found in coupling to parasitic two-level systems (TLS) in the material surrounding the circuit and even making up the circuit. Because they are always present in superconducting quantum circuits, their dynamics and physical origin are currently a big topic in research [Lis+19; Bil+20]. Were our circuits dominated by loss due to coupling to randomly distributed dissipators, shorter lifetimes would be expected at higher frequencies [Hou+08]. In the presented samples, we observed no direct correlation of transition frequency

and T_1 times [Sch+20]. To extend on this argument and to quantize the TLS loss contribution, temperature, field and strain dependent measurements have proven to be useful tools [Goe+17; MCL19] that can be applied to nanowire oscillators in the future.

Optimizing the circuit's anharmonicity can additionally help distinguishing loss channels contributed by transitions to higher levels occurring at frequencies close to ω_{01}. This is especially relevant since the short control pulses have a finite bandwidth in the MHz range. While optimized pulse shapes have been shown to reduce the rate at which unintended transitions are excited [Mot+09], the first approach to understand and reduce the amount of loss contributed by these higher transitions is to increase their distance.

The Ramsey fringes measured to determine the circuit's coherence time are sensitive to additional levels. Since they are further detuned from the drive pulses, their presence results in additional frequency components modulating the damped sine response, especially at higher powers and when driven close to ω_{01}. Consequently, identifying the pure dephasing of the fundamental transition is challenging.

As was pointed out in our design considerations, a limiting factor for the anharmonicity in these circuits is the linear inductance contribution of the granular aluminum making up the capacitive shunt. This contribution can be reduced by using a low kinetic inductance material like pure aluminum for the circuit's capacitance, concentrating the inductance in the nanowire. Consequently, the total inductance of the circuit would decrease and the capacitance would need to be increased to reach the same transition frequency range. This has been realized in the second, spiral oscillator design (Fig. 3.3) and first results are presented in the next chapter.

In this design, the large charging energy $e^2/2hC$ of $(880 \pm 80)\,\text{MHz}$ gives rise to a sensitivity toward charge noise that can cause dephasing. Additionally to the benefit of a larger anharmonicity, which allows for a study of the effect higher levels have on the measured lifetimes, increasing the capacitance helps decreasing the effect of charge noise [Koc+07] and thus has potential for further improving the circuit's performance. Together, while they increase fabrication complexity, these design changes offer a first step toward optimized nanowire qubits and understanding of factors imposing limits on their performance.

We demonstrated coherence in disordered superconducting nanowire circuits with sufficient anharmonicity for controlled excitations. Granular aluminum nanowires show great promise already in the presented compact, one-layer design, combining a large, nonlinear kinetic inductance with low loss. Since their dynamic properties

are manifestations of their microscopic structure, making these properties accessible in coherent quantum circuits offers a pathway to their systematic investigation.

5 Managing disorder

The disordered superconducting nanowire oscillators have already shown promising properties. We have demonstrated coherence, control over individual transitions, and microsecond excited state lifetimes. All this has been realized in compact circuits fabricated from a single layer of granular aluminum [Sch+20].

We now want to take this further by addressing the challenges that have been uncovered. Advancing the design and implementing a characterization scheme prior to operation in the microwave regime, we make use of the observed controllability of the nanowire transport properties by current pulses [Vos+20]. After all, exploiting intrinsic disorder depends on the ability to manage it.

The initial approach depended on the sheet resistance of the metal film as measure for the final circuit's normal state resistance and inductance then derived from its geometry. While our in situ sputter control (Sec. 3.2.1) allows for the preparation of AlO_x films with the desired resistance, variations introduced at different steps and scales can induce considerable deviations of the final circuit parameters. There are large scale fluctuations like film thickness fluctuations induced during the sputter deposition or later during etching. Even more defining and less susceptible to fabrication process optimizations, however, are fluctuations arising on the nanometer scale of the nanowire's dimensions. Being composed of a granular material with typical grain sizes of around 4 nm, wires of 20 to 30 nm are intensely sensitive to unavoidable statistical variations in individual intrinsic barrier thicknesses on a nearly molecular scale. Variations of the circuit's resistance directly translate into variations of its inductance (Eq. (2.38)). In a single layer design featuring capacitive shunts also made from granular aluminum and thus contributing to the total kinetic inductance, the impact of these variations on the circuit's transition frequency can be in the order of GHz.

Adding superconducting contact lines makes the circuit's DC properties accessible for measurement and control, also at low temperatures. Without the risk of damage from probe needles, the resistance can be determined close to the temperature at which the circuits are later operated. A combination of resistance and critical current with the later observed frequencies and anharmonicities can help test model Hamiltonians describing the system's dynamics.
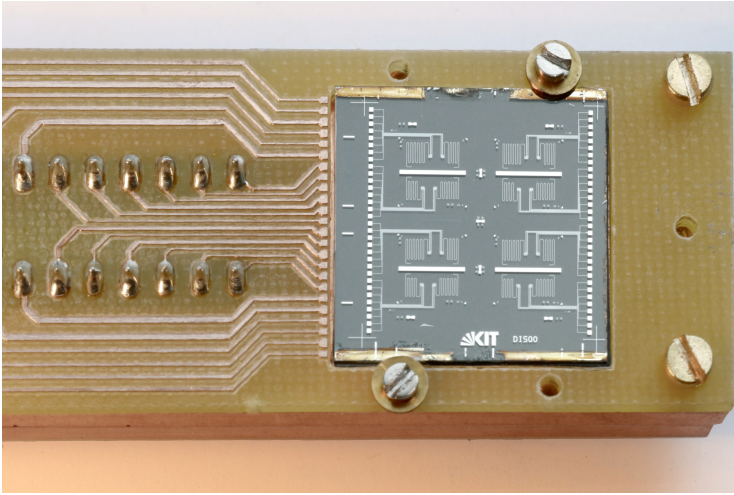
Figure 5.1: 2 cm by 2 cm wafer mounted on the DC sample holder. Contact lines from each nanowire oscillator on the four parts of the wafer lead to bond pads along both edges. Wire bonds successively connect them to the 24 copper lines leading to the DC connector of the sample holder. The wafer is held by two screws without glue, enabling easy release. Black paper added below the wafer for increased contrast in the photo.

While allowing for fabrication from a single layer, the kinetic inductance of the circuit parts outside the nanowire has been found to limit the circuit's anharmonicity. This inductance can be shunted by fabricating the contact lines and the capacitance from pure aluminum, thus allowing for an increased anharmonicity and particularly testing its limit. By facilitating their direct spectroscopy and in combination with knowledge of the geometry as well as DC properties, the distribution of higher transitions then becomes a measure for the physics governing the circuit's dynamics. In terms of applications, increased anharmonicities improve the usability of nanowires as nonlinear element in quantum circuits. For qubit control, a larger frequency spacing of the transitions allows for faster (and thus wider) control pulses and increases fidelity.

To differentiate between our single layer nanowire oscillators and the advanced design, we refer to the latter as disordered superconducting quantum oscillators (DiSQO).
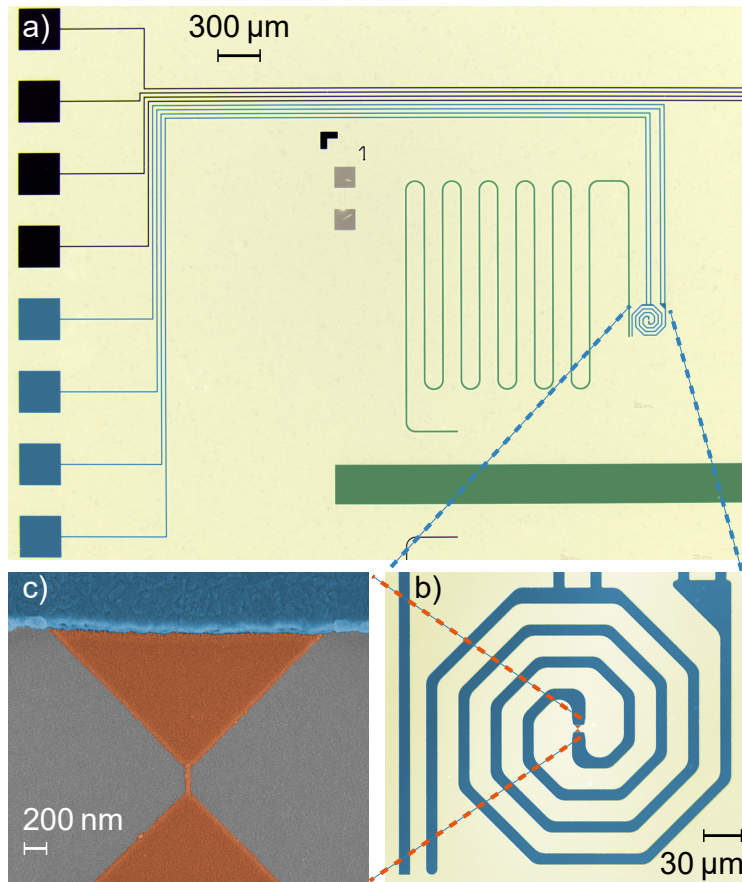
Figure 5.2: Microscope images of nanowire oscillator, contact lines, and readout. (a) The four contact lines from the spiral shaped oscillator (colored in blue) lead to wire bond pads at the wafer edge. Colored in green are the capacitively coupled $\lambda/2$ readout resonator and the microwave transmission line. **(b)** Closeup of the spiral making up the capacitance shunting the nanowire. **(c)** Colored scanning electron microscopy (SEM) image of the granular aluminum constrictions and nanowire (in orange) with part of the aluminum shunt (in blue).

5.1 Circuit characterization and adjustment

We apply the gained ability to perform four-point transport measurements to the characterization of a full $(2 \times 2)\,cm^2$ wafer. To this end, the wafer is mounted on the DC sample holder providing 24 contacts (Fig. 5.1). With 32 contacts on each side of the wafer, leading to the eight DiSQOs, two cooldowns per side are required with the possibility to leave two circuits bonded during both cooldowns. Our first wafer was cooled down in our 300 mK ^{3}He-cryostat five times over a period of ten days. The fifth time was added to verify whether the observed values remained stable. One cooldown extended over two days warming up over night to ~60 K without venting the vacuum chamber.

Before characterization of the nanowires, first the contact lines were tested. By measuring the resistance between pairs of lines leading to the same side of the DiSQO, broken lines can be detected without current flowing through the nanowire. Doing so, high resistances arising due to defects in the contact lines can be distinguished from high nanowire resistances. Additional to facilitating the measurement of the resistance locally at the DiSQO and the ability of testing the lines independently of the nanowire, the four-point approach has the advantage of offering redundancy.

Of the 64 on-chip contact lines, all but three were found working. The latter were interrupted by scratches. Two of these lines lead to the same side of one circuit (D42), rendering it inaccessible to characterization in this setup. The second affected circuit (D14) was subsequently measured using only two lines, only adding the line resistance to the measurement.

Once cooled down to ~300 mK, the current-voltage (I-V) characteristics of the DiSQOs were recorded. In current-bias, a variable bias current is fed through two lines to the circuit while the other pair of lines is used to measure the voltage dropping over it with the measurement setup depicted in figure 3.11. Typically, one trace is recorded varying the bias current from a maximum value through zero to its negative, followed by one trace swept in the opposite direction. Doing so, superconducting transport manifests in a clear zero voltage current and sharp jumps to the resistive branch above I_c. Coming from higher bias currents, the jump appears at lower values due to heating in the nanowire while sensing the resistive branch. I_c was thus extracted from the jumps occurring while sweeping out of the superconducting region.

A wire not exhibiting clear supercurrent transport might be insulating up to some critical voltage V_c or showing an intermediate, metallic-like state with a resistance that can vary closely around zero [Vos+20]. To clearly resolve the insulating regime,

voltage biasing allows for sweeping the bias voltage to identify V_c, which has to be exceeded before a resistively flowing current can be measured.

The normal state resistances of the wires were extracted from the slope of the I-V trace above I_c, typically between 70 and 100 nA. Changes in the slope appear when parts of the constrictions leading to the wire become normal conductive (Fig. 5.3). In circuits with a high nanowire resistance, these jumps can occur already at small currents, giving an offset on the extracted R_W. Since the kinetic inductance of these parts is not negligible, this was not excluded from the given values. A systematic deviation however is assumed when R_W had to be measured at higher bias currents due to higher critical currents, resulting in overestimated R_W in the shortest wires, which was considered in the larger errors. In the wires with $I_c > 170$ nA a reduction of I_c was observed in slow scans above 200 nA possibly due to heating effects.

All 16 nanowires on the wafer were found able to conduct a current, albeit in very different transport regimes. Table 5.1 lists the observed resistances and critical currents before any alteration as $R_{W,0}$ and $I_{c,0}$. Half the circuits immediately showed superconductive transport with $R_{W,0}$ ranging from around 9 to 32 kΩ and $I_{c,0}$ from 30 to 210 nA. Two were found in the intermediate regime showing the onset of superconductive transport still with a distinct impact of phase diffusion. The latter manifests in rounded edges near I_c, where the phase potential is shallow and the phase drifts, manifesting as an observed voltage (Sec. 2.1.3). Five nanowires were initially insulating with their normal state resistances reaching far above 100 kΩ. The circuit with interrupted contact lines was measured at room temperature with a two-point needle probe showing a resistance of 30 kΩ including the whole circuit, its transport regime not determined.

Figure 5.3 depicts two different regimes observed in our nanowires during initial characterization. D12 features a 300 nm long wire immediately permitting supercurrents up to $i_{c,0} = (47 \pm 1)$ nA. D44, on the other hand, was found in the insulating regime. The dotted lines illustrate the linear fit to the resistive branches of the I-V curve above 70 nA yielding R_W. A change in the slope between 60 and 70 nA indicates an increase of R by about 2 kΩ. The part of the circuit becoming normal-conductive exhibits a slightly higher I_c than the nanowire itself but is far enough not to switch to the normal state immediately with the wire due to the latter's heating.

The initially large differences in nanowire resistances even in wires of equal length underlines the importance of this characterization. Knowledge of R_W and I_c enables estimates of the transition frequency and, together with additional spectroscopy measurements, comparison to quantitative models. Additionally, circuits not in the supercurrent regime can be identified and addressed.

Table 5.1: Characterization of a full wafer by DC measurements at 300 mK. Four parts with individual transmission lines to be made into separate samples later feature four oscillators each with different nanowire length l_W, all with individual readout resonators. All of the 16 nanowires were functioning after fabrication. Their initial normal state resistances $R_{W,0}$, however, spread over a wide range between 10 and >1000 kΩ. Only D42 was measured with a needle probe due to damaged contact lines not affecting the oscillator itself. Their initial superconducting behavior varied between insulating and critical currents $I_{c,0}$ >200 nA. Applying current pulses, circuits were adjusted to R_W and I_c in the desired range. Circuits with only two values given have not been altered.

Sample	l_W (nm)	$R_{W,0}$ (kΩ)	R_W (kΩ)	$I_{c,0}$ (nA)	I_c (nA)
D11	400	>1000	25.6 ± 0.5	insulating	60 ± 3
D12	300		32.1 ± 0.5		47 ± 1
D13	250	>1000	20.8 ± 0.5	insulating	62 ± 1
D14	350	150 ± 10	31.7 ± 0.5	insulating	51 ± 3
D21	200	900 ± 20	23.3 ± 0.3	insulating	58 ± 3
D22	100	$17 \pm 1^{(1)}$			80 ± 3
D23	50	$12 \pm 2^{(1)}$			$180 \pm 20^{(2)}$
D24	150	20 ± 1			64 ± 4
D31	200	27 ± 1			56 ± 1
D32	100	$10 \pm 2^{(1)}$			155 ± 5
D33	50	$12 \pm 2^{(1)}$			$210 \pm 20^{(2)}$
D34	150	29 ± 1	20.3 ± 0.5	30 ± 1	56 ± 2
D41	400	45.8 ± 0.5	28.5 ± 0.5	$< 20^{(3)}$	57 ± 2
D42	300	$30^{(4)}$			—
D43	250	37.5 ± 0.3	22.3 ± 0.3	$< 25^{(3)}$	61 ± 1
D44	350	>1000	28.2 ± 0.3	insulating	43 ± 3

[1] Due to the large I_c, R_W was determined at higher currents and thus might include bigger parts of the constrictions leading to the nanowire.

[2] Larger errors due to possible heating during scans to higher excitations.

[3] The IV-curve shows increased phase diffusion and rounding in the transition, suggesting that superconductivity is not fully established.

[4] Probe station measurement at room temperature. D42 was not characterized at 300 mK due to scratches in the contact lines. The value thus includes the room temperature resistance of the full circuit.
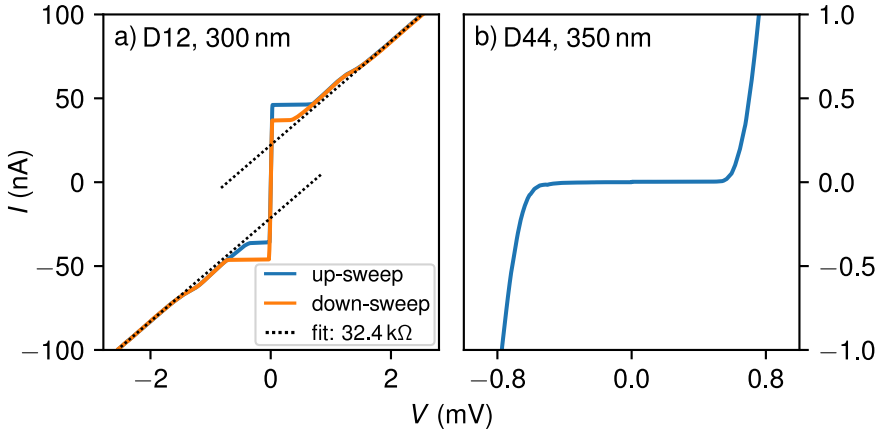
Figure 5.3: I-V characteristics of two nanowires. (a) D12 with a 300 nm long nanowire initially found in the supercurrent regime with an I_c of (47 ± 1) nm and R_W of (32.1 ± 0.5) kΩ. Between 60 and 70 nA, a change of the slope indicates additional parts of the wire or constrictions becoming normal-conductive and increasing R by about 2 kΩ. **(b)** D44 (350 nm) in the insulating regime, blocking currents below a voltage of ~0.5 mV.

Making use of the method described in section 2.2.3 and [Vos+20], we iteratively applied current pulses of (1.5 ± 0.1) s length and increasing amplitude between 5 and 250 mA to nanowires that were found not to carry supercurrents. After each of the pulses, a 2 min waiting period was introduced to allow the sample to thermalize again. Subsequently, a full I-V curve was recorded, on the basis of which it was decided whether to continue increasing the pulse amplitude or not.

All nanowires could be reduced in resistance and brought into the supercurrent regime. Table 5.1 lists the final values as R_W and I_c. In addition to increasing the yield or proportion of wires in the desired regime, the iterative nature of the method also allows for reducing the parameter spread. Between the critical current extracted from the last I-V curve taken during the adjustments and after additional waiting of several minutes to hours, we observed variations of few nA typically to higher values later. These are considered in the given errors.

We adjusted some of the circuits featuring wires of different lengths to comparable critical currents. D11 (400 nm), D13 and D43 (both 250 nm) were brought to 60 ± 2, 62 ± 1, and (61 ± 1) nA respectively. Slightly lower, D41 (400 nm), D21 (200 nm), and D34 (150 nm) were left at 57 ± 1, 58 ± 2, and (56 ± 2) nA. Figure 5.4 depicts the adjustments of D21 and D41. Though shorter, D21 started off with a much higher resistance of (900 ± 20) kΩ and exhibiting a clear blockade (Fig. 5.4 c)). D41, on the other hand, with $R_{W,0}$ of (45.8 ± 0.2) kΩ was found in the intermediate regime.

Applying current pulses up to 250 µA, the circuits were adjusted to similar critical currents (Fig. 5.4 d)).

Synchronization of the critical currents in circuits with different nanowires makes it possible to differentiate between effects caused by the circuit geometry and those caused by their electrical properties. Clearly visible in figure 5.4 d) are the different normal state resistances of the two wires even after the adjustment. In this case, the shorter wire had (23.3 ± 0.3) kΩ while the longer one had (28.5 ± 0.5) kΩ. In the picture describing the wires as ensembles of grain boundaries, multiples of which can be seen as effective junctions, the critical current is dominated by those boundaries in the current path with the thickest barriers. The normal state resistance, on the other hand, is then given by all boundaries forming the conductive channel, of which more are expected in longer wires. This also leads to different frequencies, either calculated by considering the kinetic inductance from the granular aluminum defined by R_W or by considering the Josephson inductance defined by I_c. Both effects are expected to contribute. Later, with the contact lines etched away, spectroscopy measurements thus will offer insight as to how much single barriers dominate the response in different geometries. A second interesting question regards the differences in anharmonicity. A smaller inductance in wires with equal critical current allows for a higher ratio of I/I_c and thus increases the system's nonlinearity, which directly manifests in the anharmonicity. Furthermore, if the performed adjustments can be seen as a reduction of the total number of grain boundaries and thus as a shift away from the regime dominated by individual barriers, this effect can become visible in comparison with circuits that have not been altered. Finally, removing the dominating barriers with the smallest I_c and thus increasing homogeneity can be beneficial to the circuit's performance. A current path that is dominated by few barriers is more susceptible to fluctuators coupled to these barriers and to local fluctuations of the superconducting gap.

As an outlook regarding this DC characterization method, one can envision an implementation in a dilution refrigerator. Longer cooldowns there allow for more extensive statistics and longer waiting times between current pulses, which increase the adjustments' precision. Measurements at 20 mK also eliminates the differences of I_c between the characterization at 300 mK and later microwave measurements. Since 300 mK is less than 17 % of $T_c = 1.8$ K, this difference, however, is small (Sec. 2.1). Additionally, a design that allows for microwave measurements simultaneous with DC characterizations can make their effects immediately visible. This would, however, impact the circuit's coherence. Already in the current form, this design and characterization scheme opens the pathway to a systematic study of the interplay between DC properties and internal dynamics of disordered superconducting nanowire circuits.
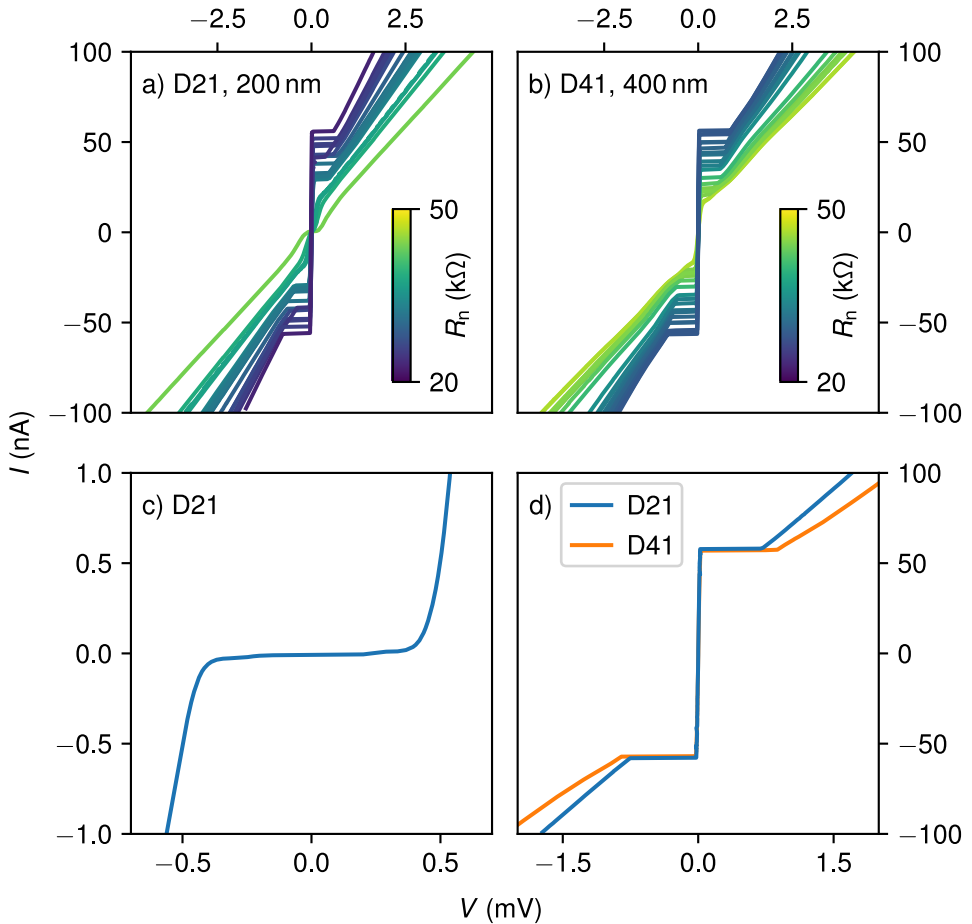
Figure 5.4: Adjustment of the superconducting behavior in two nanowires of different length at 300 mK. (a) and **(b)** I-V curves of D21 and D41 respectively. All currents are in nA and voltages in mV. Starting out as insulating, the 200 nm wire was adjusted with current pulses of 10 to 220 μA in 10 μA steps. The 400 nm long wire had a lower starting resistance showing the onset of superconductivity and was adjusted by current pulses from 10 to 250 μA. **(c)** The insulating behavior of D21 before tuning, measured by voltage biasing. Up to a voltage of 0.4 mV, the transmitted current stays below 2 pA. **(d)** I-V curves of both wires after tuning. D21 shows an I_c of (58 ± 3) nA and D41 of (57 ± 2) nA. While their I_c is the same within errors, their R_n differ with D21 having (23.3 ± 0.3) kΩ and D41 (28.5 ± 0.5) kΩ. Additional to the critical current, the different wire length is thus expected to effect their dynamics.
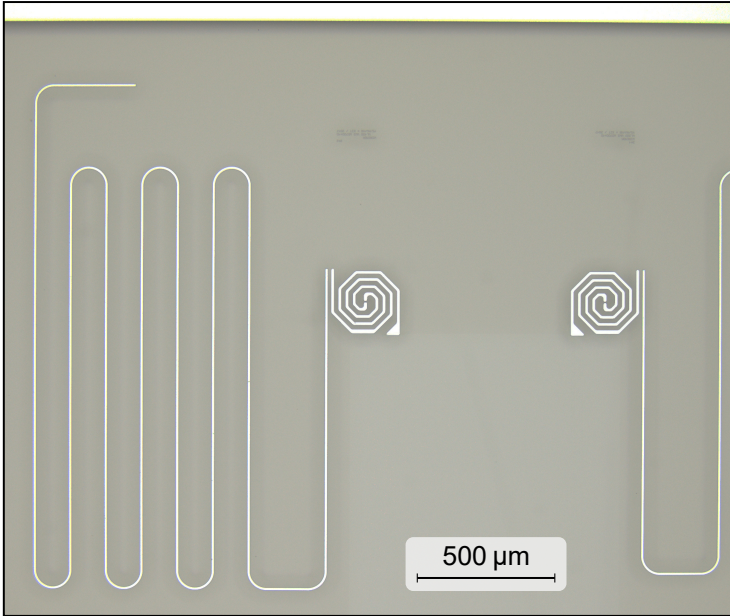
Figure 5.5: Microscope image of two nanowire oscillators and readout resonators without contact lines. After DC characterization, the contact lines were etched away, leaving the spiral oscillators, readout resonators, and transmission line (bright upper edge). An aluminum backside metallization was added as ground plane, changing the image contrast (in comparison to Fig. 5.2). The slightly brighter area below the spirals marks the area where the sapphire substrate has been etched during the removal of the contact lines.

5.2 Quantum oscillator dynamics

The internal dynamics of our DiSQO circuits were studied in our microwave setup at millikelvin temperatures. Having characterized our circuit's DC properties, the same wafer was prepared for these measurements by adding the backside metallization, removing the wafer edges with the bond pads, performing one more optical lithography, and subsequently etching away the contact lines. The required steps are outlined in greater detail in section 3.2.5. We thus obtained four (5×5) mm^2 chips that were mounted in individual microwave sample boxes providing the interface to the measurement setup and additional shielding (Sec. 3.3.3). Each of the chips features four DiSQO spiral oscillators capacitively coupled to four individual $\lambda/2$ readout resonators (Sec. 3.1.3). Figure 5.5 shows part of one chip from which the contact lines were removed.

The evaluation of the spiral oscillator design starts by observing their eigenmodes and comparison with their DC properties. This provides a first test of the com-

pact spiral capacitor. Additionally, we thereby want to determine whether small critical currents dominate their frequency in some of the geometric regimes or in dependence of the performed adjustments. Subsequent pulsed time-domain measurements can yield insights into the circuit's performance and, via the circuit anharmonicity, into the energy spectrum.

This section treats measurements that, at the time of writing, are still ongoing.

Starting by spectroscopy measurements, all 16 readout resonators were found to be working. While their design had not been changed since the previous experiments, their resonance frequencies were found slightly higher at 4.69, 5.49, 6.23, and 7.03 GHz. This is in agreement with an increased thickness of the sapphire wafer of 430 μm, which before had been 350 μm. The increased distance to the ground plane decreases the capacitance and thus yields increased frequencies. Resonators and DiSQOs are paired so that the circuits featuring longer wires are coupled to resonators of lower frequency. The listed frequencies thus correspond to samples in the order Dx1, Dx4, Dx2, and Dx3 (x denoting the chip number 1 to 4).

Applying a second microwave tone in the same way as in experiments with the single-layer design, a frequency band between 2 and 8 GHz was scanned for transitions manifesting in a shift of the readout resonator's frequency. The required coupling between readout and DiSQO manifests in a distinct decoupling of the readout resonator with increased power, as depicted in figure 5.6. For sample D24, a transition was later found at 4.28 GHz (Fig. 5.7) or $\Delta = 1.21$ GHz detuned from this resonator. Together with the observed shift of $\chi = 2.4$ MHz, the coupling is calculated as $g/2\pi = \sqrt{\chi\Delta} = (53.9 \pm 0.4)$ MHz. Finally, with the linewidth of the resonator extracted from the circle fit in figure 5.6, we obtain a Purcell limitation [Pur46; Hou+08] of $T_\mathrm{P} = (56 \pm 1)$ μs.

So far, a response was observed for most of the circuits, including all eight on chip 2 and 3 featuring the shorter wires between 50 and 200 nm and including wires that had started out as insulating and were adjusted into the supercurrent regime. Not yet identified are some of the longer wires with higher resistances. Their length increases the chances of small defects, which are more susceptible to alterations. However, their larger resistances also increase the frequency detuning from the respective readout resonator, quickly approaching the lower end of the observable frequency band. This increases the required microwave power, affecting also the background. It can thus not yet be concluded whether these circuits are working.

The observed transition frequencies are plotted in figure 5.7 with the wire resistances on the x-axis. Ranging from 3.3 to 5.6 GHz, they nearly monotonously decrease with increasing resistance. For comparison, the kinetic inductance L_k was calculated from the wire resistances R_W (Eq. (2.38)). With this, frequencies were
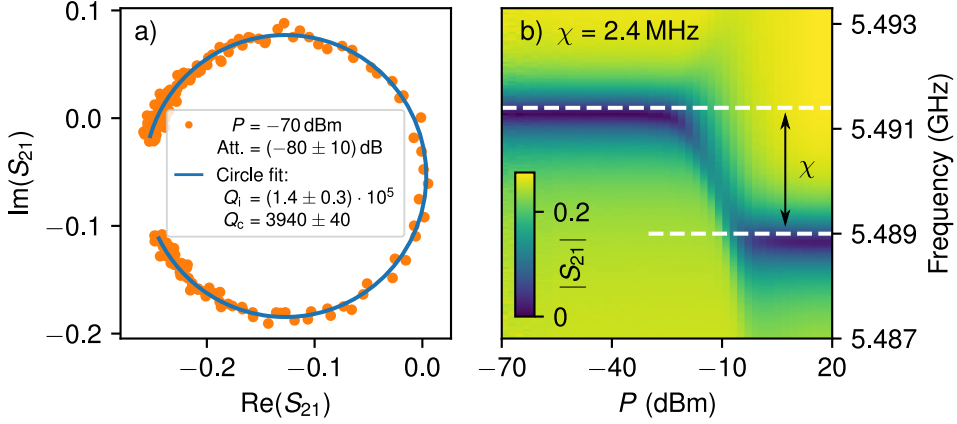
Figure 5.6: Decoupling of the readout resonator coupled to D24. (a) A circle fit to the low-power complex S_{21} resonance circle yields its quality factors $Q_i = (1.4 \pm 0.3) \cdot 10^5$ and $Q_c = 3940 \pm 40$. The additional attenuation of (-80 ± 10) dB is due to the cabling and attenuation in the cryostat and extracted from a room temperature measurement. **(b)** Increasing the readout power, the resonator decouples from the DiSQO, resulting in a shift of its resonance frequency of $\chi = 2.4$ MHz. The power is given excluding the additional attenuation of (80 ± 10) dB in the cryostat. The detuning between resonator and D24 is $\Delta = f_r - f_{01} = 1.21$ GHz.

calculated once by $1/2\pi\sqrt{L_k C}$ for a harmonic oscillator with $C = (77 \pm 2)$ fF, and once by additionally subtracting $E_C/h = e^2/2hC = 252$ MHz. The latter would constitute the eigenfrequency of a Transmon qubit with a Josephson junction of corresponding inductance L_J. Such a tunnel barrier, however, would exhibit a larger I_c than the ones observed in the nanowires. This indicates the importance of the total kinetic inductance arising from the nanowire itself. While the circuit parts constituting the capacitance are shunted by pure aluminum, the parts of the nanowire not limiting the critical current still add to its inductance.

Two DiSQOs with 150 nm long wires and comparable resistance were measured at frequencies differing by 260 MHz. The lower frequency arises in the circuit with a lower I_c of (56 ± 2) nA compared to (64 ± 2) nA in the other. Two factors can contribute to this difference. First, one circuit's resistance had been adjusted during the DC characterization. This affects mainly the nanowire where the current density is highest, leaving the environment unaffected. A possibly locally higher sheet resistance in this circuit thus still manifests in an additional inductance contribution by the constrictions between the nanowire and aluminum shunts. Additionally, the nonlinearity of the wire inductance can be expected to reduce the frequency more in those wires with smaller critical currents. Further studies of the circuit's anharmonicity and their differences can help distinguish these two factors. A reduction of the wire inductance, while maintaining the contribution
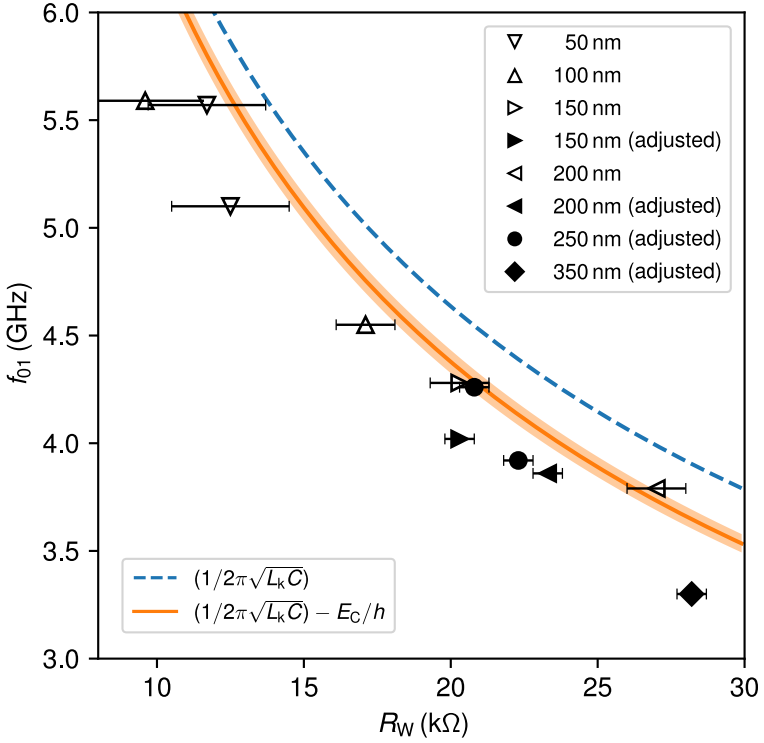
Figure 5.7: Frequencies of the DiSQOs over their wire resistance. The presented frequencies are obtained by two-tone spectroscopy. R_W corresponds to the wire resistance extracted from the I-V curves. Larger errors are assumed for circuits where R_W was fitted at higher excitations and thus might include contributions from the environment (Tab. 5.1). $C = (77 \pm 2)$ fF obtained from simulations (Sec. 3.1.3). L_k denotes the kinetic inductance calculated from R_W (Eq. (2.38)).

of the environment, is expected to reduce the fraction of nonlinear inductance and thus also the anharmonicity. A smaller critical current in a circuit of similar inductance, on the other hand, increases the fraction I/I_c and thus yields a higher anharmonicity.

To gain insight into the performance of the spiral design with increased capacitance and shunted circuit inductance, time domain measurements were conducted (Fig. 5.8 a)). The observed T_1 time of (9.1 ± 0.1) μs is longer than values previously measured (Fig. 4.6). This demonstrates that a changed circuit design can have substantial effects and we are not yet limited by loss due to the nanowires themselves.
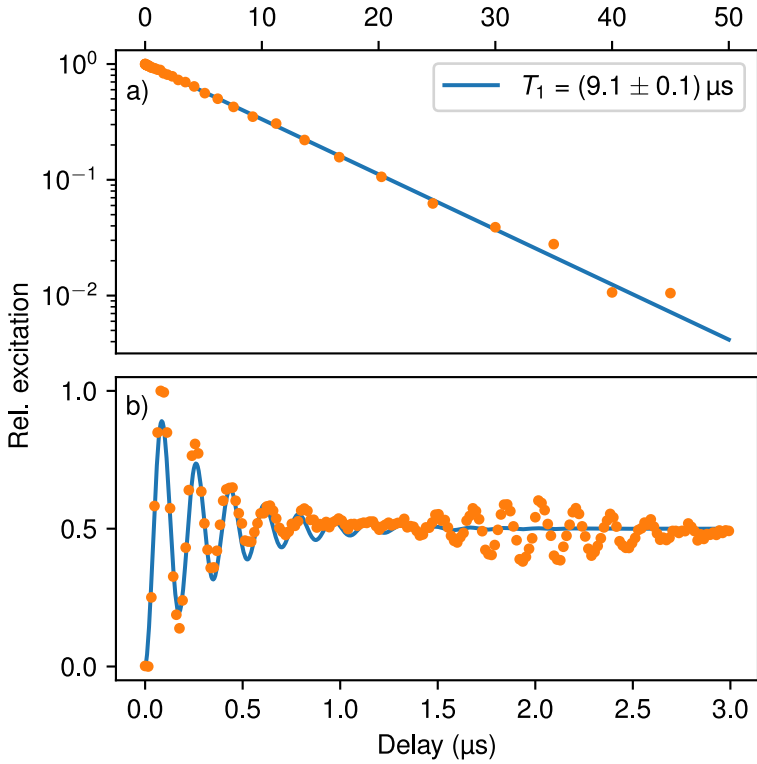
Figure 5.8: Preliminary time domain measurements of D24. (a) T_1 measurement with D24 yielding a lifetime of $(9.1 \pm 0.1)\,\mu s$. **(b)** Ramsey experiment with D24 establishing coherence in the DiSQO design. The observed frequency beating and modulation suppresses the Ramsey fringes on a first timescale of $0.35\,\mu s$ while T_2 might well extend over a longer period. The origin of the revival still needs to be determined.

A first Ramsey experiment (Fig. 5.8 b)) shows the characteristic fringes arising from coherent phase oscillations. Additionally, a revival after a first decay hints at a longer T_2, with a beating suppressing the oscillations.

To provide an outlook, we expect that a comprehensive study of the frequency and power dependence of the Rabi and Ramsey experiments will help clarify the anharmonicity arising from different nanowires and the origin of additional frequency components in the presented Ramsey experiment. The trends observed in these measurements distinguish higher transitions from potentially emerging mode splittings. T_1 and T_2 measurements for all samples can reveal limitations and whether systematic dependencies on the wire geometry or adjustments exist.

If the inductance in the nanowire itself is found to limit the anharmonicity, shorter wires with smaller I_c could be advantageous. This requires fabrication from films

with larger sheet resistance, likely making adjustments necessary and increasing the fraction of the inductance contributed by the environment. As pointed out, the latter then limits I/I_c. This contribution from outside the wire can then be further reduced by switching to e-beam lithography for the capacitive shunts, reducing the size of the gap between the leads to just the area of the wire.

Our DiSQO circuits with spiral capacitor successfully demonstrated their applicability in the studies of dynamics arising in nanowires from disordered granular aluminum in the quantum regime. The low temperature DC characterization proves a valuable tool to gain precision in quantitative models depending on DC properties like resistance and critical currents. Inhomogeneities inherent to circuits fabricated from disordered materials can be controlled by the introduced adjustments, also increasing the yield. Circuits initially insulating showed clear resonances after the application of this scheme. In comparison to tunnel contacts with properties fully defined during fabrication, our method allows for modifications of these properties after fabrication and even with simultaneous measurement.

6 Conclusion

This thesis presented superconducting circuits employing granular aluminum nanowires as nonlinear element. We showed coherent dynamics even in nanowires made from a highly disordered superconductor. These nanowires were found to provide sufficient anharmonicity to allow for the controlled excitation of individual transitions in a quantum circuit.

Two designs were introduced and realized. Derived from the anharmonic oscillator designs of the Transmon qubit, they allow for the studying of a novel circuit element in a well known environment. This highlights the differences arising due to the material and nanowires. Replacing zero-dimensional tunnel contacts commonly used in superconducting quantum circuits by granular aluminum nanowires allows for the realization of the circuit from a single material layer without inter-layer contacts and in a very compact layout. The material is grown on a clean substrate and provides the necessary large kinetic inductance when structured into nanoscopic dimensions. In a second design, an additional layer of pure aluminum was introduced for larger structures.

Probing our circuits by microwave spectroscopy and by pulsed time-domain measurements, we observed Rabi oscillations, which we studied in dependence of drive power and frequency. At higher powers and at frequencies below the main transition, deviations from the two-level model occur. The observed behavior was interpreted to stem from higher order transitions in a circuit with small anharmonicity. Additional numerical calculations reproduced the observed asymmetry in the frequency dependent Rabi pattern for a model of an oscillator with anharmonicity in the low MHz range. At lower drive powers, individual transitions could be controllably excited. Measurements of the energy relaxation yielded lifetimes in the µs range. This further underlines the promising properties of granular aluminum as high kinetic inductance material in superconducting quantum circuits. By measuring Ramsey fringes, we were moreover able to demonstrate the coherent nature of the oscillations, even in nanowires far longer than the superconducting coherence length and with high intrinsic disorder.

A factor limiting the anharmonicity in these circuits has been identified as the inductance contributed from larger circuit parts with much smaller current densi-

ties, which do not contribute to the nonlinear response. To reduce this additional inductance, the added layer of pure aluminum in the second design shunts these larger circuit parts. Together with the implemented fabrication methods removing the dielectric photoresist, this has been facilitated by adapting an argon milling process to our 20 nm thin granular aluminum films. To further the ability to correlate the observed dynamic response with the DC properties of the nanowires, additional DC contact lines were introduced in this design. This facilitates the low temperature characterization of the samples before their microwave response is probed.

We combined this characterization with the application of the effect that allows for the adjustment of nanowire resistances and critical currents through short current pulses. Doing so, it was possible to adjust the superconducting regimes of all contacted circuits to the desired critical currents, including those that initially exhibited insulating behavior. By demonstrating the possibility of adjusting wires of different lengths made from the same metal film to comparable critical currents and resistances, this method enables studies of the different effects of length and resistance independent from each other. Measurements of these circuits' microwave response after the removal of the contact lines confirmed the applicability of this approach to quantum circuits, which further show promising performances with T_1 times greater than 9 µs.

As an outlook, one can imagine to take the presented method a step further: Sacrificing long lifetimes for DC lines that remain attached also during spectroscopy. Carefully designed impedance mismatches allow the observation of oscillations and the changes in their frequency and anharmonicity while the nanowire resistance is adjusted. Also, the precise characterization and adjustability of nanowires facilitates experiments that require multiple wires with precisely defined properties. Devices that operate in regimes that are otherwise difficult to reach benefit too. For instance, phase slip devices depend on the ability to set their critical voltage in a narrow range.

In summary, we successfully realized new types of quantum circuits with superconducting nanowires, studied their dynamics, showed coherent excitations with µs lifetimes, and presented a method for DC characterizations and post-fabrication circuit adjustments.

Bibliography

[ACC66]   B. Abeles, R. W. Cohen, and G. W. Cullen: *Enhancement of Superconductivity in Metal Films*. Physical Review Letters **17**.12 (1966), pp. 632–634. DOI: 10.1103/PhysRevLett.17.632 (cit. on p. 17).

[All14]   Allresist GmBH: *Positive PMMA E-Beam Resists AR-P 630-670 series*. (2014). URL: https://www.allresist.com/wp-content/uploads/sites/2/2015/12/allresist%7B%5C_%7Dproduktinfos%7B%5C_%7Dar-p630-670%7B%5C_%7Denglisch.pdf (visited on 2020-11-26) (cit. on p. 54).

[AB63a]   V. Ambegaokar and A. Baratoff: *Tunneling Between Superconductors*. Physical Review Letters **10**.11 (1963), pp. 486–489. DOI: 10.1103/PhysRevLett.10.486 (cit. on pp. 2, 11).

[AB63b]   V. Ambegaokar and A. Baratoff: *Tunneling Between Superconductors (Erratum)*. Physical Review Letters **11**.2 (1963), pp. 104–104. DOI: 10.1103/PhysRevLett.11.104 (cit. on p. 11).

[AR63]   P. W. Anderson and J. M. Rowell: *Probable Observation of the Josephson Superconducting Tunneling Effect*. Physical Review Letters **10**.6 (1963), pp. 230–232. DOI: 10.1103/PhysRevLett.10.230 (cit. on p. 23).

[And70]   P. W. Anderson: *How Josephson discovered his effect*. Physics Today **23**.11 (1970), pp. 23–29. DOI: 10.1063/1.3021826 (cit. on p. 10).

[ASB89]   S. M. Anlage, H. J. Snortland, and M. R. Beasley: *A current controlled variable delay superconducting transmission line*. IEEE Transactions on Magnetics **25**.2 (1989), pp. 1388–1391. DOI: 10.1109/20.92554 (cit. on p. 19).

[Ann+10]   A. J. Annunziata, D. F. Santavicca, L. Frunzio, G. Catelani, M. J. Rooks, A. Frydman, and D. E. Prober: *Tunable superconducting nanoinductors*. Nanotechnology **21**.44 (2010), p. 445202. DOI: 10.1088/0957-4484/21/44/445202 (cit. on p. 19).

[Aru+19]   F. Arute, K. Arya, R. Babbush, D. Bacon, J. C. Bardin, et al.: *Quantum supremacy using a programmable superconducting processor*. Nature **574**.7779 (2019), pp. 505–510. DOI: 10.1038/s41586-019-1666-5 (cit. on p. 38).

[BD01]   A. D. Bain and R. S. Dumont: *Introduction to Floquet theory: The calculation of spinning sideband intensities in magic-angle spinning NMR.* Concepts in Magnetic Resonance **13**.3 (2001), pp. 159–170. DOI: 10. 1002/cmr.1006 (cit. on p. 34).

[BCS57]   J. Bardeen, L. N. Cooper, and J. R. Schrieffer: *Theory of Superconductivity.* Physical Review **108**.5 (1957), pp. 1175–1204. DOI: 10.1103/PhysRev. 108.1175 (cit. on p. 5).

[Bez12]   A. Bezryadin: *Superconductivity in Nanowires: Fabrication and Quantum Transport.* Weinheim: Wiley-VCH, 2012 (cit. on p. 12).

[Bil19]   A. Bilmes: *Resolving locations of defects in superconducting transmon qubits.* PhD thesis. Karlsruhe Institute of Technology (KIT), 2019. DOI: 10.5445/KSP/1000097557 (cit. on p. 28).

[Bil+20]   A. Bilmes, A. Megrant, P. Klimov, G. Weiss, J. M. Martinis, A. V. Ustinov, and J. Lisenfeld: *Resolving the positions of defects in superconducting quantum bits.* Scientific Reports **10**.1 (2020), pp. 1–6. DOI: 10.1038/s41598- 020-59749-y (cit. on pp. 28, 43, 76).

[BGO20]   A. Blais, S. M. Girvin, and W. D. Oliver: *Quantum information processing and quantum optics with circuit quantum electrodynamics.* Nature Physics **16**.3 (2020), pp. 247–256. DOI: 10.1038/s41567-020-0806-z (cit. on pp. 24, 37, 38).

[Bla+04]   A. Blais, R.-S. Huang, A. Wallraff, S. M. Girvin, and R. J. Schoelkopf: *Cavity quantum electrodynamics for superconducting electrical circuits: An architecture for quantum computation.* Physical Review A **69**.6 (2004), p. 062320. DOI: 10.1103/PhysRevA.69.062320 (cit. on pp. 23–25).

[Bou+98]   V. Bouchiat, D. Vion, P. Joyez, D. Esteve, and M. H. Devoret: *Quantum Coherence with a Single Cooper Pair.* Physica Scripta **T76**.1 (1998), p. 165. DOI: 10.1238/Physica.Topical.076a00165 (cit. on pp. 10, 38).

[Bra+15]   J. Braumüller, J. Cramer, S. Schlör, H. Rotzinger, L. Radtke, A. Lukashenko, P. Yang, S. T. Skacel, S. Probst, M. Marthaler, L. Guo, A. V. Ustinov, and M. P. Weides: *Multiphoton dressing of an anharmonic superconducting many-level quantum circuit.* Physical Review B **91**.5 (2015), p. 054523. DOI: 10.1103/PhysRevB.91.054523 (cit. on p. 73).

[Bra+16]   J. Braumüller, M. Sandberg, M. R. Vissers, A. Schneider, S. Schlör, L. Grünhaupt, H. Rotzinger, M. Marthaler, A. Lukashenko, A. Dieter, A. V. Ustinov, M. P. Weides, and D. P. Pappas: *Concentric transmon qubit featuring fast tunability and an anisotropic magnetic dipole moment.* Applied Physics Letters **108**.3 (2016), p. 032601. DOI: 10.1063/1.4940230 (cit. on p. 41).

[Bra18]   J. Braumüller: *Quantum simulation experiments with superconducting circuits*. PhD thesis. Karlsruhe Institute of Technology (KIT), 2018. 149 pp. DOI: `10.5445/KSP/1000081315` (cit. on pp. 33, 34, 41).

[Bru+96]   M. Brune, F. Schmidt-Kaler, A. Maali, J. Dreyer, E. Hagley, J. M. Raimond, and S. Haroche: *Quantum Rabi Oscillation: A Direct Test of Field Quantization in a Cavity*. Physical Review Letters **76**.11 (1996), pp. 1800–1803. DOI: `10.1103/PhysRevLett.76.1800` (cit. on p. 23).

[BH54]   W. Buckel and R. Hilsch: *Einfluss der Kondensation bei tiefen Temperaturen auf den elektrischen Widerstand und die Supraleitung fuer verschiedene Metalle*. Zeitschrift fuer Physik **138**.2 (1954), pp. 109–120. DOI: `10.1007/BF01337903` (cit. on p. 17).

[CLS59]   G. Chanin, E. A. Lynton, and B. Serin: *Impurity Effects on the Superconductive Critical Temperature of Indium and Aluminum*. Physical Review **114**.3 (1959), pp. 719–724. DOI: `10.1103/PhysRev.114.719` (cit. on p. 17).

[Chi+16]   B. Chiaro, A. Megrant, A. Dunsworth, Z. Chen, R. Barends, B. Campbell, Y. Chen, A. Fowler, I. C. Hoi, E. Jeffrey, J. Kelly, J. Mutus, C. Neill, P. J. J. O'Malley, C. Quintana, P. Roushan, D. Sank, A. Vainsencher, J. Wenner, T. C. White, and J. M. Martinis: *Dielectric surface loss in superconducting resonators with flux-trapping holes*. Superconductor Science and Technology **29**.10 (2016), p. 104006. DOI: `10.1088/0953-2048/29/10/104006` (cit. on p. 43).

[Cho+12]   J. M. Chow, J. M. Gambetta, A. D. Córcoles, S. T. Merkel, J. A. Smolin, C. Rigetti, S. Poletto, G. A. Keefe, M. B. Rothwell, J. R. Rozen, M. B. Ketchen, and M. Steffen: *Universal Quantum Gate Set Approaching Fault-Tolerant Thresholds with Superconducting Qubits*. Physical Review Letters **109**.6 (2012), p. 060501. DOI: `10.1103/PhysRevLett.109.060501` (cit. on p. 43).

[Cla+04]   J. Claudon, F. Balestro, F. W. J. Hekking, and O. Buisson: *Coherent Oscillations in a Superconducting Multilevel Quantum System*. Physical Review Letters **93**.18 (2004), p. 187003. DOI: `10.1103/PhysRevLett.93.187003` (cit. on p. 72).

[CA68]   R. W. Cohen and B. Abeles: *Superconductivity in Granular Aluminum Films*. Physical Review **168**.2 (1968), pp. 444–450. DOI: `10.1103/PhysRev.168.444` (cit. on p. 17).

[CC-BY]   *Creative Commons Attribution 4.0 International Public License*. URL: `https://creativecommons.org/licenses/by/4.0/` (visited on 2020-12-21) (cit. on p. 20).

[DK10]   D. van Delft and P. Kes: *The discovery of superconductivity*. Physics Today **63**.9 (2010), pp. 38–43. DOI: 10.1063/1.3490499 (cit. on p. 17).

[Deu+73]   G. Deutscher, H. Fenichel, M. Gershenson, E. Grünbaum, and Z. Ovadyahu: *Transition to zero dimensionality in granular aluminum superconducting films*. Journal of Low Temperature Physics **10**.1-2 (1973), pp. 231–243. DOI: 10.1007/BF00655256 (cit. on p. 17).

[Dev97]   M. H. Devoret: "Quantum Fluctuations in Electrical Circuits". *Quantum Fluctuations (Les Houches, Session LXIII, 1995)*. Ed. by S. Reynaud, E. Giacobino, and F. David. North-Holland, 1997, pp. 351–386. URL: https://qulab.eng.yale.edu/documents/reprints/Houches_fluctuations.pdf (cit. on pp. 11, 24, 41).

[DMC85]   M. H. Devoret, J. M. Martinis, and J. Clarke: *Measurements of Macroscopic Quantum Tunneling out of the Zero-Voltage State of a Current-Biased Josephson Junction*. Physical Review Letters **55**.18 (1985), pp. 1908–1911. DOI: 10.1103/PhysRevLett.55.1908 (cit. on p. 12).

[Dua+11]   H. Duan, H. Hu, K. Kumar, Z. Shen, and J. K. W. Yang: *Direct and Reliable Patterning of Plasmonic Nanostructures with Sub-10-nm Gaps*. ACS Nano **5**.9 (2011), pp. 7593–7600. DOI: 10.1021/nn2025868 (cit. on p. 56).

[Dut+08]   S. K. Dutta, F. W. Strauch, R. M. Lewis, K. Mitra, H. Paik, T. A. Palomaki, E. Tiesinga, J. R. Anderson, A. J. Dragt, C. J. Lobb, and F. C. Wellstood: *Multilevel effects in the Rabi oscillations of a Josephson phase qubit*. Physical Review B **78**.10 (2008), p. 104510. DOI: 10.1103/PhysRevB.78.104510 (cit. on p. 72).

[EH00]   C. Enss and S. Hunklinger: *Tieftemperaturphysik*. Berlin: Springer-Verlag, 2000 (cit. on p. 61).

[Eve+15]   J. Evertsson, F. Bertram, F. Zhang, L. Rullik, L. Merte, M. Shipilin, M. Soldemo, S. Ahmadi, N. Vinogradov, F. Carlà, J. Weissenrieder, M. Göthelid, J. Pan, A. Mikkelsen, J.-O. Nilsson, and E. Lundgren: *The thickness of native oxides on aluminum alloys and single crystals*. Applied Surface Science **349** (2015), pp. 826–832. DOI: 10.1016/j.apsusc.2015.05.043 (cit. on p. 58).

[Fey82]   R. P. Feynman: *Simulating physics with computers*. International Journal of Theoretical Physics **21**.6-7 (1982), pp. 467–488. DOI: 10.1007/BF02650179 (cit. on p. 2).

[FLS11]   R. Feynman, R. B. Leighton, and M. Sands: *The Feynman Lectures on Physics: The Millennium Edition*. New York: Basic Books, 2011 (cit. on p. 9).

[Fis86]   M. P. A. Fisher: *Quantum Phase Slips and Superconductivity in Granular Films*. Physical Review Letters **57**.7 (1986), pp. 885–888. DOI: 10.1103/PhysRevLett.57.885 (cit. on pp. 3, 13, 17).

[Frö50]   H. Fröhlich: *Theory of the Superconducting State. I. The Ground State at the Absolute Zero of Temperature*. Physical Review **79**.5 (1950), pp. 845–856. DOI: 10.1103/PhysRev.79.845 (cit. on p. 5).

[FR81]   E. Fukushima and S. B. W. Roeder: *Experimental Pulse NMR*. Boca Raton: CRC Press, 1981. DOI: 10.1201/9780429493867 (cit. on p. 62).

[Gab+20]   I. Gablech, J. Brodský, J. Pekárek, and P. Neužil: *Infinite Selectivity of Wet SiO2 Etching in Respect to Al*. Micromachines **11**.4 (2020), p. 365. DOI: 10.3390/mi11040365 (cit. on p. 56).

[Gao08]   J. Gao: *The Physics of Superconducting Microwave Resonators*. PhD thesis. California Institute of Technology, 2008. DOI: 10.7907/RAT0-VM75 (cit. on p. 30).

[GZ04]   C. Gardiner and P. Zoller: *Quantum noise: A handbook of Markovian and non-Markovian quantum stochastic methods with applications to quantum optics*. 3rd ed. Berlin, Heidelberg: Springer-Verlag, 2004 (cit. on p. 34).

[GB01]   S. Gevorgian and H. Berg: *Line Capacitance and Impedance of Coplanar-Strip Waveguides on Substrates with Multiple Dielectric Layers. 31st European Microwave Conference, 2001*. IEEE, 2001. DOI: 10.1109/EUMA.2001.339161 (cit. on p. 44).

[Gia60]   I. Giaever: *Energy Gap in Superconductors Measured by Electron Tunneling*. Physical Review Letters **5**.4 (1960), pp. 147–148. DOI: 10.1103/PhysRevLett.5.147 (cit. on p. 8).

[GL50]   V. L. Ginzburg and L. D. Landau: *On the Theory of Superconductivity*. Journal of Experimental and Theoretical Physics **20** (1950), p. 1064 (cit. on pp. 1, 7, 9).

[GL65]   V. L. Ginzburg and L. D. Landau: "On the Theory of Superconductivity". *Collected Papers of L.D. Landau*. Ed. by D. ter Haar. Oxford: Pergamon Press, 1965, pp. 546–568. DOI: 10.1016/B978-0-08-010586-4.50078-X (cit. on pp. 7, 9).

[Gio88]   N. Giordano: *Evidence for Macroscopic Quantum Tunneling in One-Dimensional Superconductors*. Physical Review Letters **61**.18 (1988), pp. 2137–2140. DOI: 10.1103/PhysRevLett.61.2137 (cit. on p. 12).

[Goe+17] J. Goetz, F. Deppe, P. Eder, M. Fischer, M. Müting, J. P. Martínez, S. Pogorzalek, F. Wulschner, E. Xie, K. G. Fedorov, A. Marx, and R. Gross: *Second-order decoherence mechanisms of a transmon qubit probed with thermal microwave states*. Quantum Science and Technology **2**.2 (2017), p. 025002. DOI: `10.1088/2058-9565/aa66e7` (cit. on p. 77).

[Gor59] L. P. Gor'kov: *Microscopic Derivation of the Ginzburg-Landau Equations in the Theory of Superconductivity*. Journal of Experimental and Theoretical Physics **9**.6 (1959), pp. 1364–1367 (cit. on pp. 7, 8).

[GKS76] V. Gorini, A. Kossakowski, and E. C. G. Sudarshan: *Completely positive dynamical semigroups of N-level systems*. Journal of Mathematical Physics **17**.5 (1976), pp. 821–825. DOI: `10.1063/1.522979` (cit. on p. 33).

[Gra+12] G. J. Grabovskij, T. Peichl, J. Lisenfeld, G. Weiss, and A. V. Ustinov: *Strain Tuning of Individual Atomic Tunneling Systems Detected by a Superconducting Qubit*. Science **338**.6104 (2012), pp. 232–234. DOI: `10.1126/science.1226487` (cit. on p. 28).

[Grü+17] L. Grünhaupt, U. von Lüpke, D. Gusenkova, S. T. Skacel, N. Maleeva, S. Schlör, A. Bilmes, H. Rotzinger, A. V. Ustinov, M. Weides, and I. M. Pop: *An argon ion beam milling process for native AlO x layers enabling coherent superconducting contacts*. Applied Physics Letters **111**.7 (2017), p. 072601. DOI: `10.1063/1.4990491` (cit. on p. 59).

[Grü+18] L. Grünhaupt, N. Maleeva, S. T. Skacel, M. Calvo, F. Levy-Bertrand, A. V. Ustinov, H. Rotzinger, A. Monfardini, G. Catelani, and I. M. Pop: *Loss Mechanisms and Quasiparticle Dynamics in Superconducting Microwave Resonators Made of Thin-Film Granular Aluminum*. Physical Review Letters **121**.11 (2018), p. 117001. DOI: `10.1103/PhysRevLett.121.117001` (cit. on p. 18).

[Grü+19] L. Grünhaupt, M. Spiecker, D. Gusenkova, N. Maleeva, S. T. Skacel, I. Takmakov, F. Valenti, P. Winkel, H. Rotzinger, W. Wernsdorfer, A. V. Ustinov, and I. M. Pop: *Granular aluminium as a superconducting material for high-impedance quantum circuits*. Nature Materials **18**.8 (2019), pp. 816–819. DOI: `10.1038/s41563-019-0350-3` (cit. on pp. 2, 18).

[Har13] S. Haroche: *Nobel Lecture: Controlling photons in a box and exploring the quantum to classical boundary*. Reviews of Modern Physics **85**.3 (2013), pp. 1083–1102. DOI: `10.1103/RevModPhys.85.1083` (cit. on pp. 1, 23).

[HR06] S. Haroche and J.-M. Raimond: *Exploring the Quantum: Atoms, Cavities, and Photons*. 1st ed. Oxford: Oxford University Press, 2006 (cit. on pp. 24–27, 73).

[Hen+19]   F. Henriques, F. Valenti, T. Charpentier, M. Lagoin, C. Gouriou, M. Martínez, L. Cardani, M. Vignati, L. Grünhaupt, D. Gusenkova, J. Ferrero, S. T. Skacel, W. Wernsdorfer, A. V. Ustinov, G. Catelani, O. Sander, and I. M. Pop: *Phonon traps reduce the quasiparticle density in superconducting circuits*. Applied Physics Letters **115**.21 (2019), p. 212601. DOI: 10.1063/1.5124967 (cit. on p. 29).

[HGK03]   W. Henschel, Y. M. Georgiev, and H. Kurz: *Study of a high contrast process for hydrogen silsesquioxane as a negative tone electron beam resist*. Journal of Vacuum Science & Technology B: Microelectronics and Nanometer Structures **21**.5 (2003), p. 2018. DOI: 10.1116/1.1603284 (cit. on p. 52).

[Hou+08]   A. A. Houck, J. A. Schreier, B. R. Johnson, J. M. Chow, J. Koch, J. M. Gambetta, D. I. Schuster, L. Frunzio, M. H. Devoret, S. M. Girvin, and R. J. Schoelkopf: *Controlling the Spontaneous Emission of a Superconducting Transmon Qubit*. Physical Review Letters **101**.8 (2008), p. 080502. DOI: 10.1103/PhysRevLett.101.080502 (cit. on pp. 29, 75, 76, 89).

[Ith+05]   G. Ithier, E. Collin, P. Joyez, P. J. Meeson, D. Vion, D. Esteve, F. Chiarello, A. Shnirman, Y. Makhlin, J. Schriefl, and G. Schön: *Decoherence in a superconducting quantum bit circuit*. Physical Review B **72**.13 (2005), p. 134519. DOI: 10.1103/PhysRevB.72.134519 (cit. on pp. 26–28).

[Jae+89]   H. M. Jaeger, D. B. Haviland, B. G. Orr, and A. M. Goldman: *Onset of superconductivity in ultrathin granular metal films*. Physical Review B **40**.1 (1989), pp. 182–196. DOI: 10.1103/PhysRevB.40.182 (cit. on p. 17).

[JC63]   E. T. Jaynes and F. W. Cummings: *Comparison of Quantum and Semiclassical Radiation Theories with Application to the Beam Maser*. Proceedings of the IEEE **51**.1 (1963), pp. 89–109. DOI: 10.1109/PROC.1963.1664 (cit. on p. 24).

[JNN12]   J. R. Johansson, P. D. Nation, and F. Nori: *QuTiP: An open-source Python framework for the dynamics of open quantum systems*. Computer Physics Communications **183**.8 (2012), pp. 1760–1772. DOI: 10.1016/j.cpc.2012.02.021 (cit. on p. 40).

[Jos62]   B. D. Josephson: *Possible new effects in superconductive tunnelling*. Physics Letters **1**.7 (1962), pp. 251–253. DOI: 10.1016/0031-9163(62)91369-0 (cit. on p. 9).

[Jos74]   B. D. Josephson: *The discovery of tunnelling supercurrents*. Reviews of Modern Physics **46**.2 (1974), pp. 251–254. DOI: 10.1103/RevModPhys.46.251 (cit. on p. 9).

[Kam11]   H. Kamerlingh Onnes: *Further experiments with liquid helium.* KNAW, Proceedings **13** (1911), pp. 1093–1113. URL: https://www.dwc.knaw.nl/DL/publications/PU00013343.pdf (cit. on p. 17).

[Kar+19]   K. Karatsu, A. Endo, J. Bueno, P. J. de Visser, R. Barends, D. J. Thoen, V. Murugesan, N. Tomita, and J. J. A. Baselmans: *Mitigation of cosmic ray effect on microwave kinetic inductance detector arrays*. Applied Physics Letters **114**.3 (2019), p. 032601. DOI: 10.1063/1.5052419 (cit. on p. 29).

[Kel02]   L. Kelvin: *XXIX. Aepinus atomized*. The London, Edinburgh, and Dublin Philosophical Magazine and Journal of Science **3**.15 (1902), pp. 257–283. DOI: 10.1080/14786440209462764 (cit. on p. 17).

[Kja+20]   M. Kjaergaard, M. E. Schwartz, J. Braumüller, P. Krantz, J. I.-J. Wang, S. Gustavsson, and W. D. Oliver: *Superconducting Qubits: Current State of Play*. Annual Review of Condensed Matter Physics **11**.1 (2020), pp. 369–395. DOI: 10.1146/annurev-conmatphys-031119-050605 (cit. on pp. 2, 29).

[Koc+07]   J. Koch, T. M. Yu, J. M. Gambetta, A. A. Houck, D. I. Schuster, J. Majer, A. Blais, M. H. Devoret, S. M. Girvin, and R. J. Schoelkopf: *Charge-insensitive qubit design derived from the Cooper pair box*. Physical Review A **76**.4 (2007), p. 042319. DOI: 10.1103/PhysRevA.76.042319 (cit. on pp. 38, 40, 77).

[Kol08]   K. Kolari: *High etch selectivity for plasma etching SiO2 with AlN and Al2O3 masks*. Microelectronic Engineering **85**.5-6 (2008), pp. 985–987. DOI: 10.1016/j.mee.2007.12.037 (cit. on p. 56).

[Kra+19]   P. Krantz, M. Kjaergaard, F. Yan, T. P. Orlando, S. Gustavsson, and W. D. Oliver: *A quantum engineer's guide to superconducting qubits*. Applied Physics Reviews **6**.2 (2019), p. 021318. DOI: 10.1063/1.5089550 (cit. on p. 28).

[Kri+19]   S. Krinner, S. Storz, P. Kurpiers, P. Magnard, J. Heinsoo, R. Keller, J. Lütolf, C. Eichler, and A. Wallraff: *Engineering cryogenic setups for 100-qubit scale superconducting circuit systems*. EPJ Quantum Technology **6**.1 (2019), p. 2. DOI: 10.1140/epjqt/s40507-019-0072-0 (cit. on pp. 29, 64).

[Kru+99]   J. Krupka, K. Derzakowski, M. Tobar, J. Hartnett, and R. G. Geyer: *Complex permittivity of some ultralow loss dielectric crystals at cryogenic temperatures*. Measurement Science and Technology **10**.5 (1999), pp. 387–392. DOI: 10.1088/0957-0233/10/5/308 (cit. on p. 43).

[KO75]   I. O. Kulik and A. N. Omel'Yanchuk: *Contribution to the microscopic theory of the Josephson effect in superconducting bridges*. Journal of Experimental and Theoretical Physics Letters **21**.4 (1975), p. 96. URL: http://www.jetpletters.ac.ru/ps/1463/article_22289.shtml (cit. on p. 15).

[Lan37]   L. D. Landau: *On the Theory of Phase Transitions*. Journal of Experimental and Theoretical Physics **7** (1937), p. 19 (cit. on p. 7).

[Lik79]   K. K. Likharev: *Superconducting weak links*. Reviews of Modern Physics **51**.1 (1979), pp. 101–159. DOI: 10.1103/RevModPhys.51.101 (cit. on pp. 15, 16).

[Lin76]   G. Lindblad: *On the generators of quantum dynamical semigroups*. Communications in Mathematical Physics **48**.2 (1976), pp. 119–130. DOI: 10.1007/BF01608499 (cit. on p. 33).

[Lis+19]   J. Lisenfeld, A. Bilmes, A. Megrant, R. Barends, J. Kelly, P. Klimov, G. Weiss, J. M. Martinis, and A. V. Ustinov: *Electric field spectroscopy of material defects in transmon qubits*. npj Quantum Information **5**.1 (2019), p. 105. DOI: 10.1038/s41534-019-0224-1 (cit. on p. 76).

[Mad18]   M. J. Madou: *Manufacturing Techniques for Microfabrication and Nanotechnology*. 3rd ed. Boca Raton: CRC Press, 2018. DOI: 10.1201/9781315274164 (cit. on pp. 54, 57).

[Mal+18]   N. Maleeva, L. Grünhaupt, T. Klein, F. Levy-Bertrand, O. Dupre, M. Calvo, F. Valenti, P. Winkel, F. Friedrich, W. Wernsdorfer, A. V. Ustinov, H. Rotzinger, A. Monfardini, M. V. Fistul, and I. M. Pop: *Circuit quantum electrodynamics of granular aluminum resonators*. Nature Communications **9**.1 (2018), p. 3889. DOI: 10.1038/s41467-018-06386-9 (cit. on pp. 19, 20).

[Mar+05]   J. M. Martinis, K. B. Cooper, R. McDermott, M. Steffen, M. Ansmann, K. D. Osborn, K. Cicak, S. Oh, D. P. Pappas, R. W. Simmonds, and C. C. Yu: *Decoherence in Josephson Qubits from Dielectric Loss*. Physical Review Letters **95**.21 (2005), p. 210503. DOI: 10.1103/PhysRevLett.95.210503 (cit. on p. 28).

[MB58]   D. C. Mattis and J. Bardeen: *Theory of the Anomalous Skin Effect in Normal and Superconducting Metals*. Physical Review **111**.2 (1958), pp. 412–417. DOI: 10.1103/PhysRev.111.412 (cit. on p. 19).

[Max50]   E. Maxwell: *Isotope Effect in the Superconductivity of Mercury*. Physical Review **78**.4 (1950), p. 477. DOI: 10.1103/PhysRev.78.477 (cit. on p. 5).

[Maz20]   B. A. Mazin: *Superconducting Materials for Microwave Kinetic Inductance Detectors* (2020), pp. 1–19. URL: http://arxiv.org/abs/2004.14576 (cit. on p. 18).

[McC68]   D. E. McCumber: *Effect of ac Impedance on dc Voltage-Current Characteristics of Superconductor Weak-Link Junctions*. Journal of Applied Physics **39**.7 (1968), pp. 3113–3118. DOI: 10.1063/1.1656743 (cit. on p. 12).

[MN06]   J. E. Mooij and Y. V. Nazarov: *Superconducting nanowires as quantum phase-slip junctions*. Nature Physics **2**.3 (2006), pp. 169–172. DOI: 10.1038/nphys234 (cit. on pp. 3, 14).

[Moo+15]   J. E. Mooij, G. Schön, A. Shnirman, T. Fuse, C. J. P. M. Harmans, H. Rotzinger, and A. H. Verbruggen: *Superconductor–insulator transition in nanowires and nanowire arrays*. New Journal of Physics **17**.3 (2015), p. 033006. DOI: 10.1088/1367-2630/17/3/033006 (cit. on p. 15).

[Mot+09]   F. Motzoi, J. M. Gambetta, P. Rebentrost, and F. K. Wilhelm: *Simple Pulses for Elimination of Leakage in Weakly Nonlinear Qubits*. Physical Review Letters **103**.11 (2009), p. 110501. DOI: 10.1103/PhysRevLett.103.110501 (cit. on p. 77).

[MCL19]   C. Müller, J. H. Cole, and J. Lisenfeld: *Towards understanding two-level-systems in amorphous solids: insights from quantum circuits*. Reports on Progress in Physics **82**.12 (2019), p. 124501. DOI: 10.1088/1361-6633/ab3a7e (cit. on pp. 3, 28, 77).

[NPT99]   Y. Nakamura, Y. A. Pashkin, and J. S. Tsai: *Coherent control of macroscopic quantum states in a single-Cooper-pair box*. Nature **398**.6730 (1999), pp. 786–788. DOI: 10.1038/19718 (cit. on pp. 1, 37).

[Nam+98]   H. Namatsu, Y. Takahashi, K. Yamazaki, T. Yamaguchi, M. Nagase, and K. Kurihara: *Three-dimensional siloxane resist for the formation of nanopatterns with minimum linewidth fluctuations*. Journal of Vacuum Science & Technology B: Microelectronics and Nanometer Structures **16**.1 (1998), p. 69. DOI: 10.1116/1.589837 (cit. on p. 52).

[PA98]   P. J. Petersan and S. M. Anlage: *Measurement of resonant frequency and quality factor of microwave resonators: Comparison of methods*. Journal of Applied Physics **84**.6 (1998), pp. 3392–3402. DOI: 10.1063/1.368498 (cit. on pp. 30, 33).

[Pla+20]   A. P. M. Place, L. V. H. Rodgers, P. Mundada, B. M. Smitham, M. Fitzpatrick, Z. Leng, A. Premkumar, J. Bryon, S. Sussman, G. Cheng, T. Madhavan, H. K. Babla, B. Jaeck, A. Gyenis, N. Yao, R. J. Cava, N. P. de Leon, and A. A. Houck: *New material platform for superconducting*

transmon qubits with coherence times exceeding 0.3 milliseconds (2020). URL: http://arxiv.org/abs/2003.00024 (cit. on p. 29).

[PPT05]   G. E. Ponchak, J. Papapolymerou, and M. M. Tentzeris: *Excitation of coupled slotline mode in finite-ground CPW with unequal ground-plane widths*. IEEE Transactions on Microwave Theory and Techniques **53**.2 (2005), pp. 713–717. DOI: 10.1109/TMTT.2004.840571 (cit. on p. 43).

[Poz12]   D. M. Pozar: *Microwave engineering*. 4. ed. Hoboken, NJ: Wiley, 2012 (cit. on pp. 29–31).

[Pro+15] S. Probst, F. B. Song, P. A. Bushev, A. V. Ustinov, and M. P. Weides: *Efficient and robust analysis of complex scattering data under noise in microwave resonators*. Review of Scientific Instruments **86**.2 (2015), p. 024706. DOI: 10.1063/1.4907935 (cit. on p. 33).

[Pur46]   E. M. Purcell: *Spontaneous Emission Probabilities at Radio Frequencies*. *Proceedings of the American Physical Society*. Vol. 69. 11-12. 1946, p. 681. DOI: 10.1103/PhysRev.69.674.2 (cit. on pp. 29, 75, 89).

[qkit]   *Qkit – a quantum measurement suite in python*. URL: https://github.com/qkitgroup/qkit (visited on 2020-11-26) (cit. on pp. 46, 50).

[Rad03]   R. Radebaugh: "Pulse Tube Cryocoolers". *Low Temperature and Cryogenic Refrigeration*. Dordrecht: Springer Netherlands, 2003, pp. 415–434. DOI: 10.1007/978-94-010-0099-4_24 (cit. on p. 61).

[Ram50]   N. F. Ramsey: *A Molecular Beam Resonance Method with Separated Oscillating Fields*. Physical Review **78**.6 (1950), pp. 695–699. DOI: 10.1103/PhysRev.78.695 (cit. on p. 28).

[RW13]   M. Rommel and J. Weis: *Hydrogen silsesquioxane bilayer resists — Combining high resolution electron beam lithography and gentle resist removal*. Journal of Vacuum Science & Technology B **31**.6 (2013), 06F102. DOI: 10.1116/1.4822136 (cit. on p. 56).

[Rot+16] H. Rotzinger, S. T. Skacel, M. Pfirrmann, J. N. Voss, J. Münzberg, S. Probst, P. A. Bushev, M. P. Weides, A. V. Ustinov, and J. E. Mooij: *Aluminium-oxide wires for superconducting high kinetic inductance circuits*. Superconductor Science and Technology **30**.2 (2016), p. 025002. DOI: 10.1088/0953-2048/30/2/025002 (cit. on pp. 2, 18, 50, 54).

[SFK20]   B. Sacépé, M. Feigel'man, and T. M. Klapwijk: *Quantum breakdown of superconductivity in low-dimensional materials*. Nature Physics **16**.7 (2020), pp. 734–746. DOI: 10.1038/s41567-020-0905-x (cit. on pp. 3, 18, 22).

[San+13]   M. Sandberg, M. R. Vissers, T. A. Ohki, J. Gao, J. Aumentado, M. Weides, and D. P. Pappas: *Radiation-suppressed superconducting quantum bit in a planar geometry*. Applied Physics Letters **102**.7 (2013), p. 072601. DOI: 10.1063/1.4792698 (cit. on p. 43).

[Sch+19]   S. Schlör, J. Lisenfeld, C. Müller, A. Bilmes, A. Schneider, D. P. Pappas, A. V. Ustinov, and M. Weides: *Correlating Decoherence in Transmon Qubits: Low Frequency Noise by Single Fluctuators*. Physical Review Letters **123**.19 (2019), p. 190502. DOI: 10.1103/PhysRevLett.123.190502 (cit. on p. 28).

[Sch97]   V. V. Schmidt: *The Physics of Superconductors*. Ed. by P. Müller and A. V. Ustinov. Berlin, Heidelberg: Springer-Verlag, 1997. DOI: 10.1007/978-3-662-03501-6 (cit. on pp. 5–8).

[Sch+18]   A. Schneider, J. Braumüller, L. Guo, P. Stehle, H. Rotzinger, M. Marthaler, A. V. Ustinov, and M. P. Weides: *Local sensing with the multilevel ac Stark effect*. Physical Review A **97**.6 (2018), p. 062334. DOI: 10.1103/PhysRevA.97.062334 (cit. on pp. 35, 75).

[Sch+20]   Y. Schön, J. N. Voss, M. Wildermuth, A. Schneider, S. T. Skacel, M. P. Weides, J. H. Cole, H. Rotzinger, and A. V. Ustinov: *Rabi oscillations in a superconducting nanowire circuit*. npj Quantum Materials **5**.1 (2020), p. 18. DOI: 10.1038/s41535-020-0220-x (cit. on pp. 2, 18, 35, 70, 72–77, 79).

[Sch07]   D. I. Schuster: *Circuit Quantum Electrodynamics*. PhD thesis. Yale University, 2007 (cit. on p. 25).

[Sha63]   S. Shapiro: *Josephson Currents in Superconducting Tunneling: The Effect of Microwaves and Other Observations*. Physical Review Letters **11**.2 (1963), pp. 80–82. DOI: 10.1103/PhysRevLett.11.80 (cit. on p. 10).

[Shi65]   J. H. Shirley: *Solution of the Schrödinger Equation with a Hamiltonian Periodic in Time*. Physical Review **138**.4B (1965), B979–B987. DOI: 10.1103/PhysRev.138.B979 (cit. on p. 34).

[SSH97]   A. Shnirman, G. Schön, and Z. Hermon: *Quantum Manipulations of Small Josephson Junctions*. Physical Review Letters **79**.12 (1997), pp. 2371–2374. DOI: 10.1103/PhysRevLett.79.2371 (cit. on pp. 1, 10, 38).

[Ste68]   W. C. Stewart: *Current-Voltage Characteristics of Josephson Junctions*. Applied Physics Letters **12**.8 (1968), pp. 277–280. DOI: 10.1063/1.1651991 (cit. on p. 12).

[Tin04]   M. Tinkham: *Introduction to Superconductivity*. 2nd ed. Mineola: Dover, 2004 (cit. on pp. 5–7, 9, 11, 12, 19).

[Vij+09]   R. Vijay, J. D. Sau, M. L. Cohen, and I. Siddiqi: *Optimizing Anharmonicity in Nanoscale Weak Link Josephson Junction Oscillators*. Physical Review Letters **103**.8 (2009), p. 087003. DOI: `10.1103/PhysRevLett.103.087003` (cit. on p. 16).

[Vio+02]   D. Vion, A. Aassime, A. Cottet, P. Joyez, H. Pothier, C. Urbina, D. Esteve, and M. H. Devoret: *Manipulating the quantum state of an electrical circuit*. Science **296**.5569 (2002), pp. 886–889. DOI: `10.1126/science.1069372` (cit. on p. 27).

[Vos+20]   J. N. Voss, Y. Schön, M. Wildermuth, D. Dorer, J. H. Cole, H. Rotzinger, and A. V. Ustinov: *Insulating, metallic and superconducting behavior in a single nanowire*. 2020. arXiv: `2006.06588 [cond-mat.supr-con]` (cit. on pp. 3, 4, 21–23, 79, 82, 85).

[WM08]   D. Walls and G. J. Milburn, eds.: *Quantum Optics*. 2nd ed. Berlin, Heidelberg: Springer-Verlag, 2008. DOI: `10.1007/978-3-540-28574-8` (cit. on p. 24).

[WLA19]   Z. M. Wang, J. S. Lehtinen, and K. Y. Arutyunov: *Towards quantum phase slip based standard of electric current*. Applied Physics Letters **114**.24 (2019), p. 242601. DOI: `10.1063/1.5092271` (cit. on p. 14).

[Wil+20]   M. Wildermuth, L. Powalla, J. N. Voss, Y. Schön, A. Schneider, A. Shnirmann, H. Rotzinger, and A. V. Ustinov: "Ultra-slow fluxoids in impedance-tailored long Josephson junctions". In preparation. 2020 (cit. on p. 51).

[Win13]   D. J. Wineland: *Nobel Lecture: Superposition, entanglement, and raising Schrödinger's cat*. Reviews of Modern Physics **85**.3 (2013), pp. 1103–1114. DOI: `10.1103/RevModPhys.85.1103` (cit. on p. 1).

[Yan+08]   H. Yang, A. Jin, Q. Luo, J. Li, C. Gu, and Z. Cui: *Electron beam lithography of HSQ/PMMA bilayer resists for negative tone lift-off process*. Microelectronic Engineering **85**.5-6 (2008), pp. 814–817. DOI: `10.1016/j.mee.2008.01.006` (cit. on p. 54).

[Zai+97]   A. D. Zaikin, D. S. Golubev, A. van Otterlo, and G. T. Zimányi: *Quantum Phase Slips and Transport in Ultrathin Superconducting Wires*. Physical Review Letters **78**.8 (1997), pp. 1552–1555. DOI: `10.1103/PhysRevLett.78.1552` (cit. on pp. 3, 14).

My publications

[Sch+20]   Y. Schön, J. N. Voss, M. Wildermuth, A. Schneider, S. T. Skacel, M. P. Weides, J. H. Cole, H. Rotzinger, and A. V. Ustinov: *Rabi oscillations in a superconducting nanowire circuit*. npj Quantum Materials **5**.1 (2020), p. 18. DOI: 10.1038/s41535-020-0220-x.

[Vos+20]   J. N. Voss, Y. Schön, M. Wildermuth, D. Dorer, J. H. Cole, H. Rotzinger, and A. V. Ustinov: *Insulating, metallic and superconducting behavior in a single nanowire*. 2020. arXiv: 2006.06588 [cond-mat.supr-con].

[Bar+20]   C. Barone, H. Rotzinger, J. N. Voss, C. Mauro, Y. Schön, A. V. Ustinov, and S. Pagano: *Current-Resistance Effects Inducing Nonlinear Fluctuation Mechanisms in Granular Aluminum Oxide Nanowires*. Nanomaterials **10**.3 (2020), p. 524. DOI: 10.3390/nano10030524.

[Wil+20]   M. Wildermuth, L. Powalla, J. N. Voss, Y. Schön, A. Schneider, A. Shnirmann, H. Rotzinger, and A. V. Ustinov: "Ultra-slow fluxoids in impedance-tailored long Josephson junctions". In preparation. 2020.

[Bov+18]   I. Boventer, M. Pfirrmann, J. Krause, Y. Schön, M. Kläui, and M. Weides: *Complex temperature dependence of coupling and dissipation of cavity magnon polaritons from millikelvin to room temperature*. Physical Review B **97**.18 (2018), p. 184420. DOI: 10.1103/PhysRevB.97.184420.

Appendix

Fabrication parameters

E-Beam lithography

Preparation

- Substrate cleaning in Piranha solution
- Cleaning plasma: 20 W, 20 s, static 6×10^{-1} mbar argon/oxygen (10:1)
- Granular aluminum sputter deposition: 50 to 170 W, varied gas flows
- Cleaning with NEP in ultrasonic bath prior to lithography

Photoresist spin-coating

- PMMA
  - Ramp up: 300 rpm for 10 s
  - Full speed: 7500 rpm for 60 s
  - Acceleration: 7500 rpm/s
  - Reflow time: 30 s
  - Bake-out: 4 min at 160 °C
- HSQ
  - Ramp up: 300 rpm for 4 s
  - Full speed: 2000 rpm for 60 s
  - Acceleration: 7500 rpm/s
  - Reflow time: 30 s

– Bake-out: 2 min at 150 °C

Exposure and developing

- Base dose: 700 to 900 µC/cm^2

- Multiplicator for individual shots defining nanowires: ~ 10

- Beam current: 100 pA (fine structures), 10 nA (large structures)

- Developer: AZ 726 MIF

- Developing time: 65 s

Etching

- Oxygen plasma for PMMA/HSQ double-stack process
    - Gas: 15 sccm argon, 15 sccm oxygen
    - Pressure: 6.67×10^{-3} mbar
    - Plasma power: 50 W
    - Time: $\sim$10 s
- Chlorine plasma for PMMA/HSQ double-stack process
    - Gas: 15 sccm argon, 15 sccm chlorine
    - Pressure: 6.67×10^{-3} mbar
    - Plasma power: 50 W
    - Time: $n \times 7$ s
    - Necessary iterations determined with tests on films with similar parameters
- Chlorine plasma for HSQ etching process
    - Gas: 2 sccm argon, 12 sccm chlorine
    - Pressure: 13.33×10^{-3} mbar
    - Plasma power: 100 W
    - Time: 40 to 70 s

      – Necessary time determined with tests on films with similar parameters

- Fluorine plasma for HSQ etching process

      – Gas: 15 sccm CF_4

      – Pressure: 20×10^{-3} mbar

      – Plasma power: 40 W

      – Time: $\sim$60 s

Optical lithography

Photoresist spin-coating

- S1805

      – Ramp up: 500 rpm for 5 s

      – Full speed: 4500 rpm for 60 s

      – Acceleration: 500 rpm/s

      – Reflow time: 30 s

      – Bake-out: 60 s at 115 °C

- AZ 5214E

      – Ramp up: 500 rpm for 5 s

      – Full speed: 6000 rpm for 60 s

      – Acceleration: 7500 rpm/s

      – Reflow time: 30 s

      – Bake-out: 50 s at 110 °C

Exposure and developing

- S1805
    - Dose: $13\,\text{mW/cm}^2$
    - Exposure time: $4\,\text{s}$
    - Developer: AZ-Developer + H_2O (1:1)
    - Developing time: $35\,\text{s}$
- AZ 5214E
    - Dose: $13\,\text{mW/cm}^2$
    - Time: $5\,\text{s}$
    - Developer: AZ-Developer + H_2O (1:1)
    - Developing time: $33\,\text{s}$

Argon milling

- Substrate cleaning
    - Gas: $4\,\text{sccm}$ argon, $0.5\,\text{sccm}$ oxygen
    - Beam parameters: $10\,\text{mA}$ at $200\,\text{V}$
    - Time: $5\,\text{s}$
- In case of inter-layer contacts
    - Gas: $4\,\text{sccm}$ argon
    - Beam parameters: $15\,\text{mA}$ at $400\,\text{V}$
    - Time: $150\,\text{s}$

Aluminum evaporation

- Circuit structures

    - Thickness: 100 nm

    - Rate: 0.5 nm/s

- Backside metallization

    - Thickness: 150 nm

    - Rate: 1 nm/s

Lift-off

- ~1 h in NEP at 80 °C

- 2 min in ultrasonic bath + 3 min on 80 °C hotplate

- Last step is repeated until satisfying result

Etching of contact lines

- Gas: 15 sccm argon, 3 sccm chlorine, 1 sccm oxygen

- Pressure: 13.33×10^{-3} mbar

- Plasma power: 100 W

- Time: 60 s